ADIABATIC SHEAR LOCALIZATION IN AISI 1340 AND 4340 STEELS: THE INFLUENCE OF MICROSTRUCTURE AND GEOMETRY

A Thesis Submitted to the College of

Graduate Studies and Research

in Partial Fulfillment of the Requirements

for the Degree of Master of Science

in the Department of Mechanical Engineering

University of Saskatchewan

Saskatoon

By

Homa Mostaghimi Ghomi

PERMISSION TO USE

In presenting this thesis in partial fulfillment of the requirements for a Postgraduate degree from the University of Saskatchewan, I agree that the Libraries of this University may make it freely available for inspection. I further agree that permission for copying of this thesis/dissertation in any manner, in whole or in part, for scholarly purposes may be granted by Professor Akindele G. Odeshi who supervised my thesis work. It is understood that any copying or publication or use of this thesis or parts there of for financial gain shall not be allowed without my written permission. It is also understood that due recognition shall be given to me and to the University of Saskatchewan in any scholarly use which may be made of any material in my thesis.

DISCLAIMER

The University of Saskatchewan were exclusively created to meet the thesis and exhibition requirements for the degree of Master of Science at the University of Saskatchewan. Reference in this thesis to any specific commercial products, process, or service by trade name, trademark, manufacturer, or otherwise, does not constitute or imply its endorsement, recommendation, or favouring by the University of Saskatchewan. The views and opinions of the author expressed herein do not state or reflect those of the University of Saskatchewan, and shall not be used for advertising or product endorsement purposes.

Requests for permission to copy or to make other uses of materials in this thesis in whole or part should be addressed to.

Prof. James D. Bugg [Department of Mechanical Engineering]

University of Saskatchewan

Saskatoon, Saskatchewan S7N 5Z9

Canada

OR

Dean

College of Graduate Studies and Research

University of Saskatchewan

107 Administration Place

Saskatoon, Saskatchewan S7N 5A2

Canada

Abstract

The mechanical behaviour of AISI 1340 and 4340 steel under high strain-rate loading in compression and in torsion were investigated using direct impact Hopkinson bar and torsion split Hopkinson bars. Both alloys contained 0.40 wt. % C, but different amounts and types of alloying additions. The materials are commonly used in high performance structural applications, where they could be subjected to dynamic shock loading. The objective of this study was to study the effects of microstructure, strain rates and specimen geometry on the occurrence and failure of adiabatic shear bands in these alloys under dynamic shock loading.

Cylindrical specimens of the AISI 1340 alloys were heat treated to produce martensitic, dual-phase or pearlitic structure and subjected to impact loading at strain rates ranging between 1000 and 8000 /s. The martensitic test specimens were tempered at 205, 315 and 425 ºC to determine the effects of tempered condition on the adiabatic shear failure of the alloy. The effects of geometry on strain localization and adiabatic shear banding in both alloys were investigated by subjecting cylindrical-, cubical-, and truncated conical-shaped specimens to high velocity impact. The dynamic torsion test involved rapidly twisting of heat-treated thin-walled tubular specimens of the alloys and determining the damage evolution during the high strain torsional loading. Both optical and scanning electron microscopes were used to evaluate the damage evolution in the specimens after high strain rate loading.

The types of shear band formed in the alloys depended on the microstructure and strain rate. Deformed bands were formed at low strain rates and there was a minimum strain rate required for formation of transformed band in both alloys. This minimum strain rate was highest in the specimens with pearlitic structure and lowest in the specimen with martensitic structure. The susceptibility of the martensitic specimens to the occurrence of transformed shear band decreased with increasing tempering temperature. Cracks were initiated and propagated along transformed bands leading to fragmentation under the impact loading. The susceptibility of the adiabatic shear bands to cracking was markedly influenced by strain-rates, initial microstructure and the specimens' geometry. The geometry of the impacted specimen determined the shape of the adiabatic shear

band and the topography of the fracture surface of fragmented specimens. Fractographic investigation of fragmented specimens showed ductile shear failure and knobby fracture mode along the transformed band. Investigations of the transformed band using X-ray Photo Emission Electron Microscopy and Near Edge X-ray Absorption Fine structure Spectroscopy showed more nickel and less chromium inside the transformed bands in impacted AISI 4340 steel than in the region outside the shear band.

Acknowledgements

I would like to acknowledge the people who contributed to a successful completion of this work. My appreciations go to my parent for their moral and financial support. I am very grateful to my supervisor, Professor Akindele G. Odeshi, for all his unflinching support, encouragement and guidance. His deep understanding of situation is greatly valued and highly appreciated. The assistance of Professor M. Nabil Bassim in the experimental work of this study in University of Manitoba is also is appreciated. My gratitude also goes to Dr. Richard Evitts, Dr. Ikechukwuka N. Oguocha, and Dr. Qiaoqin Yang for their valuable course of materials. To Prof. Jerzy A. Szpunar, Prof. James Johnston, my committee members, I say big thank you for your time. I also would like to thank Prof. Leon Wegner for his time as the external examiner. I thank Prof. James D. Bugg, the Head of Department of Mechanical Engineering for his understanding, support and help. The financial support the Natural Sciences and Engineering Research Council of Canada (NSERC) for this research project in form of Discovery Grant to my supervisor is highly appreciated. I also wish to acknowledge Robert Peace for his assistance and support in my experimental work. I also would like to thank Dr. Uday Lanke of the Canadian Light Source (CLS) for his help in my experimental work. Lastly, lots of thanks to all the department technicians, office support staff, other graduate students and especially my very supportive friends for their support.

Table of Contents

List of Figures

List of Tables

CHAPER ONE

INTRODUCTION

1.1. Overview

Dynamic shock loading at high strain-rates (10^3 s^{-1}) leads to local plastic deformation along narrow bands. This deformation differs from low strain-rate or quasi-static loading conditions where plastic deformation is relatively homogeneous. An example of dynamic shock loading is deformation of materials under high impact velocity, and the narrow bands of extreme shear strain localization are called adiabatic shear bands (ASBs). Heat generated during impact loading as a result of conversion of kinetic energy of the impacting object to heat energy during deformation, leads to thermal softening which occurs simultaneously with the strain hardening effect of plastic deformation. A near adiabatic condition usually arises in which heat generated along some narrow paths are not conducted away. This causes local thermal softening and thermo-viscous instabilities that lead to strain localization and occurrence of adiabatic shear bands. Adiabatic shear bands are of two types: Deformed and Transformed bands. Deformed bands appear as greatly distorted regions demonstrating extensive shear deformation of the grains. Transformed bands appear as white narrow bands in the impacted materials. Transformed bands are also called white etching adiabatic shear bands because of their characteristic white colour when observed under an optical microscope. The microstructure inside the transformed bands cannot be resolved under optical or Scanning Electron Microscope (SEM). However, observations of transformed adiabatic shear bands using Transmission Electron Microscope (TEM) in many materials indicated that they consist of very fine grains of sub-micron size.

The excessive thermal softening and highly localized strain inside adiabatic shear band can cause fragmentation of even ductile metals under dynamic mechanical loading. During high strain-rate deformation, tensile stresses are generated inside shear bands as

a result of the lower flow stress inside the adiabatic shear bands compared to the outside. The tensile stresses generated inside the shear band eventually become sufficiently high enough to open up micro-pores inside these bands. By coalescence of the micro-pores, voids are formed which elongate and rotate to elliptical shapes. These are finally connected, initiating microcracks which propagate along the shear band leading ultimately to fracture. Adiabatic shear bands' hardness values are usually higher than that of the bulk material due to the high density of dislocations and very fine nature of the grains inside the bands. Consequently, they are also very brittle and materials containing adiabatic shear bands are more susceptible to fracture along shear bands during subsequent loading. Therefore, fundamental understanding of the mechanism of formation and failure of adiabatic shear bands, as influenced by materials or process variables such as composition, strain-rate, microstructure, geometry, etc., is very important for controlling adiabatic shear failure of engineering components under dynamic shock loading.

1.2. Motivation

The materials investigated as part of this study were AISI 1340 and AISI 4340 alloy steels, with both containing 0.40 % C and varying degrees of alloying additions. AISI 4340 steel is one of the most popular High-Strength Low Alloy (HSLA) steels which are commonly used in high strength applications such as in the automotive industry, pressure vessels, and gas pipelines. It has considerable amounts of alloying additions, such as manganese (Mn), chromium (Cr), nickel (Ni), and molybdenum (Mo). Mn, Cr, Ni and Mo in steels increase the steel hardenability. Moreover, Cr and Mo form carbides which consequently increase matrix strength. Meanwhile, Mn helps in refining the grain size. AISI 1340 steel is a low carbon manganese steel that is mostly used in the automotive body construction. The low amount of carbon and high amount of manganese make AISI 1340 steel appropriate for formation of steel with a dual-phase structure, which consist of hard martensite in a soft ferrite matrix. The manganese addition expand the ferrite + austenite phase region in the iron-iron carbide equilibrium phase diagram, while the low carbon content, enhances the ability to intercritically anneal the steel in the ferrite+austenite phase region of the iron-iron carbide equilibrium phase diagram (shown in Fig. 3.3 on page 37). Moreover, the high amount of manganese

and carbon content of the austenite at the intercritical annealing temperature provides enough hardenability for the austenite within the AISI 1340 steel to form martensite during quenching. As a result of the unique properties of dual-phase steels, which include high strength and remarkable ductility, they are widely used in automotive body construction to save weight and consequently improve fuel consumption efficiency.

Knowledge of the formation and failure of adiabatic shear bands inside AISI 1340 and 4340 steels under dynamic shock loading as influenced by such factors such as heat-treated condition is a leading point for a fundamental understanding of high strain rate behaviour of these alloys. The fragmentation of pressure vessel or steel pipe due to excessive pressure or failure of automobile parts from a car crash can be traced to high strain-rate loading and adiabatic shear failure of the AISI 4340 and 1340 steels used in these applications, respectively.

1.3. Research objectives

The research objectives of this study were to:

1. Investigate the effects of microstructure and strain rates on plastic deformation and failure of AISI 1340 and AISI 4340 steels under dynamic shock loading,

2. Investigate the effect of specimen geometry on the formation of adiabatic shear band in AISI 1340 and AISI 4340 steels under dynamic impact loading, and

3. Investigate the chemical and bonding changes associated with the occurrence of transformed bands in alloy steel.

1.4. Methodology

In order to achieve the research objectives, cylindrical, cubical, conical (truncated) and thin-walled tubular specimens were machined from AISI 1340 and AISI 4340 steels. These thin-walled tubular and cylindrical specimens were heat-treated to obtain pearlitic, martensitic or dual phase structures in order to investigate the effects of microstructure on formation and failure of adiabatic shear band in the alloys under dynamic shock loading. Another set of cylindrical, cubical and conical specimens of the alloys were heat treated to obtain martensitic microstructure and used to investigate the

effects of specimen geometry on the characteristic of adiabatic shear bands. All the specimens were subjected to dynamic shock loadings using instrumented direct impact Hopkinson bar or Torsional Kolsky Bar. The stress-strain curves obtained were discussed in relation to the sequence of plastic deformation leading to adiabatic shear failure of the specimens. The effects of strain-rates on deformation behaviour and microstructural evolution inside the materials were investigated. The characteristics of adiabatic shear bands observed in the impacted alloys were investigated in relation to the pre-impact microstructure of the steel specimens. Fractographic studies of the fractured specimen were undertaken to understand the failure mechanisms in the alloy under the impact loading and high strain-rate loading in torsion. Synchrotron light radiation at the Canadian Light Source (CLS) was used to investigate the compositional changes associated with the occurrence of transformed bands in the AISI 4340 alloy. This provided further insight into microstructural evolution associated with the occurrence of transformed bands in this high strength steel and support the design effort of tailoring materials microstructure in order to make them more resistant to adiabatic shear failure during dynamic shock loading.

1.5. Thesis arrangement

The current chapter of the thesis introduces the focus, motivation and objective of this M.Sc. research project. Chapter two consists of a literature review of previous research investigations on the behaviour of materials under dynamic shock loadings. Relevant information on materials investigated and experimental techniques are outlined in chapter three, while chapter four contains results, their analyses and discussion. A summary of this study and the conclusions drawn from the research investigations are presented in chapter five.

CHAPTER TWO

LITERATURE REVIEW

The behaviour of materials under dynamic shock loading as reported in previous studies is reviewed in this chapter. The concept of shear strain localization along adiabatic shear bands at high strain rates is discussed. The general definition of adiabatic shear band, types of adiabatic shear bands, mechanisms of formation and failure of adiabatic shear bands, as well as properties and microstructure of adiabatic shear bands in a variety of materials are summarized in this chapter.

2.1. Adiabatic shear bands

Plastic deformation at low strain-rates or under quasi-static loadings is relatively homogeneous. Therefore, the heat generated inside the material dissipates and the material strain hardens as the shear strain increases. It is governed by slip and twinning mechanisms [1]. However, at strain rate greater than $10^3 s^{-1}$, such as impact loading, deformation becomes localized along narrow bands which are called adiabatic shear bands (ASBs) [2,3] . Heat generated during impact loading leads to thermal softening which occurs simultaneously with the strain hardening effect associated with plastic deformation. A near adiabatic condition usually arises in which heat generated along narrow paths are not conducted away, leading to excessive thermal softening and thermo-viscous instability that leads to the strain localization along the adiabatic shear bands [2,3]. Adiabatic shear band concepts have been studied experimentally [2-4] and analytically [5-9]. The concept of an adiabatic shear band was first proposed by Zener and Holloman [3]. They suggested that extensive shear strain inside the shear band causes temperature rise within shear band. Staker [10] suggested that a true shear strain at which onset of adiabatic shear band instability begins is measured experimentally by:

$$\gamma_c = \frac{-Cn}{\left(\delta\tau/_{\delta T}\right)} \tag{2.1}$$

where C is volume specific heat, n is strain hardening exponent, and $\delta\tau/\delta T$ is the slope of temperature dependence of flow stress. This relationship is applicable for any material whose stress-strain curve's first part is parabolic.

Temperature rise within adiabatic shear band depend on the material, composition, and strain rate. Odeshi and Bassim [11] suggested the heat generated inside the adiabatic shear band of AISI 4340 steel specimens during high velocity impact caused the temperature rise within adiabatic shear band close to melting point of the alloy in some regions. Duffy and Chi [12] measured the local temperature within adiabatic shear band by small high speed infrared detectors as a function of time and position for a low carbon cold-rolled steel and three quench-hardened steels (HY-100 and two tempers of AISI 4340 VAR steel of varying hardness) which were subjected to high strain-rate deformation using torsional Kolsky bars. The temperature was estimated to reach about 600˚C along the adiabatic shear band propagation path [13]. Local temperature within adiabatic shear band of SS400 steel deformed by a fine blanking process was calculated to be in the neighbourhood of 600˚C [14]. The calculated temperature inside the shear band of tantalum specimens subjected to high strain rate deformation was determined to be about 800˚C, and onset of recrystallization was observed at high microscopic strains in isolated areas [15]. Hartley *et al.* [16] determined the temperature rise within the adiabatic shear bands of cold rolled AISI 1018 steel and hot rolled AISI 1020 steel to be 450˚C based on calculations from the emitted infrared radiation from the surface of the metals.

The temperature rise within AISI 4340 VAR steel, with the hardness value 44 on the Rockwell C scale, subjected to dynamic shock loading by Torsional Kolsky Bar testing was calculated to be 460˚C using infra-red detectors [17].The highest temperature rise inside the adiabatic shear band of C-300 steel (maraging steel) was calculated to be 1400 ˚C (90% of melting point), while that for Ti-6Al-4V was about 450 ˚C [18]. For polycrystalline zirconium alloy (Zircadine 702, containing 0.7% Hf) which was subjected to impact loading using a Split Hopkinson Pressure Bar for hat-shaped specimens, temperature rise within shear band was calculated to be 930K for 100 shear strain using the Zerilli-Armstrong equation [19]. For low-carbon steel plates with

chemical composition of 0.15%C–0.25%Si–1.1%Mn– Fe (wt.%) which were subjected to high strain-rate torsional loading, the temperature rise within adiabatic shear band was found to be 540˚C with the high temperature reported to promote spheroidization of cementite inside the shear band. The temperature rise within adiabatic shear band was calculated by:

$$dT = \frac{C_p}{\beta\rho}\int \sigma \, d\varepsilon \tag{2.2}$$

where, ρ is density, C_p is heat capacity, and β is a work to heat conversion factor which is taken as 0.9. Modeling of temperature history inside the shear bands shows that heat generation inside the shear band occurs at less that 200μs, while the shear band is at maximum temperature for 19μs [20].

The higher amount of plastic deformation and strain hardening make the shear band material harder than the bulk material. As a result of high temperature and excessive thermal softening inside the shear band, the materials inside the shear band are subjected to more extensive shear strain than those outside shear band region. Therefore, adiabatic shear bands are usually brittle and their presence in a material makes it more susceptible to fracture than the material without ASBs. Fragmentation of materials which was deformed under high velocity impact were observed to be preceded by the formation of adiabatic shear bands [21, 22]. Adiabatic shear bands have been observed in practical applications such as high speed machining, explosive fragmentation [2, 13, 23], machine chips [24, 25], metal forging, and ballistic impact [26].

2.1.1. Types of adiabatic shear bands

There are two types of Adiabatic Shear Bands: deformed and transformed bands [27]. Deformed bands appear as greatly distorted areas demonstrating extensive shear deformation of the grains. They are commonly observed in non-ferrous materials such as aluminum and copper alloys. They have also been observed in commercially pure niobium subjected to dynamic impact loading at low temperature [28]. Transformed bands appear as white narrow bands in the impacted materials. They are also called white etching bands, because of the white color within ASBs after etching with nital. White etching bands are commonly observed in hardened steels [1, 13, 21, 26, 29- 32].

Timothy *et al.* [27] proposed that transformed bands are generally observed in metals with low thermal diffusivity and low resistance to adiabatic shear localization. These metals can transform to other phases at high temperatures and then generate a metastable phase by rapid cooling to room temperature, the quenching medium being the materials surrounding the shear band. White shear bands have also been reported in some aluminum alloys [33], tantalum [34], copper [35, 36], and zirconium alloys [37]. Adiabatic shear bands generally have been reported in varieties of engineering materials including rolled homogenous armour (RHA) [9], RDX/DOS composition (cyclotrimethylene trinitramine (RDX) to which was added various percentages of the binder dioctyl sebacate (DOS)) [28], titanium [38], commercially pure niobium [39], commercially pure vanadium [40], and densified silicon carbide powders [41].

There are different explanations for the white colour of the transformed adiabatic shear bands. It has been suggested that it is due to the phase transformation occurring during dynamic shock loading. Zener and Holloman [3], Cho *et al.* [13], Glenn and Leslie [29], and Rogers [42] suggested that during adiabatic heating the temperature rise inside the adiabatic shear band is high enough to cause transformation to austenite in steel along adiabatic heated path. The austenite region is quenched by the surrounding matrix to form untempered martensite. Moreover, the hardness of transformed bands in steel has been found to be close to that of untempered martensite [20].

The theory that phase transformation, leading to the formation of untempered martensite, occur inside adiabatic shear band during high strain-rate loading, has not been adequately substantiated in the literature. Meanwhile, high strain-rate deformation happens in less than 100μs. Therefore, the formation of untempered martensite as a result of quenching of the austenite inside the white etching band is doubtful in this short space of time. Cho *et al*. [13] calculated the temperature reached inside the transformed shear band of HY-100 steel specimens during a high strain-rate deformation to be 600˚C. This is below the temperature at which austenitization will occur, thereby ruling out the possibility of martensitic transformation.

White etching bands are difficult to resolve under optical and scanning electron microscopes. Transmission electron microscopic observation indicates that they consist

of very fine grains of sub-micron size. It has been suggested that during massive and swift deformation, the martensite, and carbides laths break apart into sub-grains with a few hundreds of nanometer size [1, 13]. Li *et al.* [44] observed equi-axed nano-sized grains in adiabatic shear bands which are proposed to form as a result of dynamic recrystalization. Equi-axed nano-sized structure inside the shear band has been observed by Meyers *et al.* [15] for tantalum, Xue *et al.* [33] for aluminum alloy, Hines and Vecchio [35] , and Andradea *et al.*[36] for copper, Li et al.[43] for Monel alloy, Rittel *et al.* [45], and Me-Bar and Shechtman[46] for titanium.

The nanosized grains of transformed shear bands offer another explanation for the white colour and featureless nature of these bands under an optical microscope. Wittman et al. [20] suggested that the white colour of the adiabatic shear bands is due to the limit of optical microscopes in resolving the extremely tiny particles making up the shear band. The white colour of the white etching band after etching with nital on the polished surface was also attributed to carbide dissolution, which changed the microstructure and consequently the etching properties of the shear band [20].

Although, white etching bands are commonly observed in hardened steel, depending on the heat treatment procedure, microstructure and deformation conditions, both types of shear bands can form in steels [11].

2.1.2. Multiple adiabatic shear bands

A single adiabatic shear band may be formed inside a material under dynamic shock loading causing fracture of the specimen into two pieces. Multiple adiabatic shear bands can also form leading to fragmentation into several pieces. The study of multiple adiabatic shear bands by Xue *et al.* [40] for thick-walled cylinder (TWC) of AISI 304 stainless steel subjected to explosive loading showed that initiation and propagation of multiple adiabatic shear bands changed with changes in initial loading condition. However, these effects did not change the spacing of the shear bands. Average length of shear bands, as well as the spacing between them was the same in different sections, while highest shear band length varied in different sections. The middle section with highest propagating shear band speed had the maximum length. The phenomenon of multiple adiabatic shear bands formation has been investigated by Xue *et al.* [47] for

pure titanium and Ti-6Al-4V alloy which were deformed under explosive loading of thick-walled cylinders at a strain-rate of $10^4 s^{-1}$. Multiple adiabatic shear bands initiated at the internal boundary of the tested thick wall cylindrical specimens and exhibited periodic distribution from early stages of formation. The adiabatic shear band pattern showed a self-organization property [47, 48]. The propagation velocity of shear band was higher for Ti-6Al-4V alloy than pure Ti alloy. However, the numbers of adiabatic shear bands were higher for pure Ti alloy than Ti-6Al-4V. Adiabatic shear bands showed bifurcation (splitting into two or more bands) when they formed in a spiral pattern or when the distance between them increased [47]. Loading factors and the type of material have a significant effect on adiabatic shear band spacing [47]. Spacing of the multiple adiabatic shear bands also depends on microstructural inhomogeneities which offer the adiabatic shear band initiation sites [48].

2.3. Adiabatic shear band initiation

The susceptibility to the occurrence of adiabatic shear bands depends on material properties. Materials with high strain rate sensitivity and low temperature sensitivity of flow stress are less likely to form adiabatic shear bands [42]. The tendency of a material to form adiabatic shear bands depends on its original microstructure and its thermodynamic stability [13]. Materials with high strength and low strain hardening are more susceptible to adiabatic shear localization [49]. Lee *et al*. [50] suggested that metals with higher strength (yield strength and fracture toughness) are more inclined to form adiabatic shear bands under dynamic mechanical loadings than those with lower yield strength.

Feng and Bassim [24] suggested that local material defects or any inhomogeneities inside the material cause adiabatic shear band initiations. These materials defects are called the initial perturbations. Wright [51] suggested that parametric solutions for the formation of adiabatic shear bands show that total effective perturbation of the tested samples can be calculated by simply adding the initial perturbation in strength, temperature, and wall thickness. Molinari and Clifton [52] suggested that the critical strain at which the stress collapse happens depends logarithmically on the size of the initial perturbation. As the size of initial perturbation increases, the collapse strain

decreases logarithmically. Investigation by Duffy and Chi [12] on the torsional Kolsky Bar testing of low carbon cold-rolled steel and three quench-hardened steels (HY-100 and two tempers of AISI 4340 VAR steel of varying hardness) also showed that the critical strain at which adiabatic shear bands are formed depends on the initial defects. Mataya *et al.* [53] suggested that γ' precipitates in the size of 10 nm increases the susceptibility of γ' strengthened austenitic stainless steel JBK-75 to form shear localization. It has been suggested that at high strain-rate, localized flow occurs along high angle grain boundaries in precipitates free zone in the form of recrystallized grains [53].

Bassim [34] suggested that differences in properties and microstructure cause the material to form adiabatic shear bands. Local defects and inhomogeneities inside the material act as preferential sites for shear band initiation. It has been also suggested that specimen geometry and dimensions affected the formation of adiabatic shear band. Nesterenko *et al*. [6] suggested that shear localization initiates along the grains which are favourably orientated. They also suggested that uneven distribution of grain size can act as perturbations. Larger grains show lower yield strength, while smaller grains shows higher yield strength. Therefore, larger grains deform initially and can act as preferential sites for shear localization. They also proposed that crystallographic peculiarities have a very important role in shear band initiation in the way that decreasing the grain size under 100μm increases the number of shear bands [6]. Meyers *et al*. [54] investigated the effect of grain size on the high strain rate behaviour of copper and suggested that localization of plastic deformation is observed for the coarse-grain sample while the copper sample with smaller grain size exhibited homogenous plastic deformation.

Figure 2.1 shows the possible mechanisms for shear band initiation suggested as by Nesterenko *et al*. [6] which includes: 1) Grain size inhomogeneity, 2) Geometrical softening, 3) Peirce-Asaro-Neddleman textural localization and 4) Dislocation pile-up release.

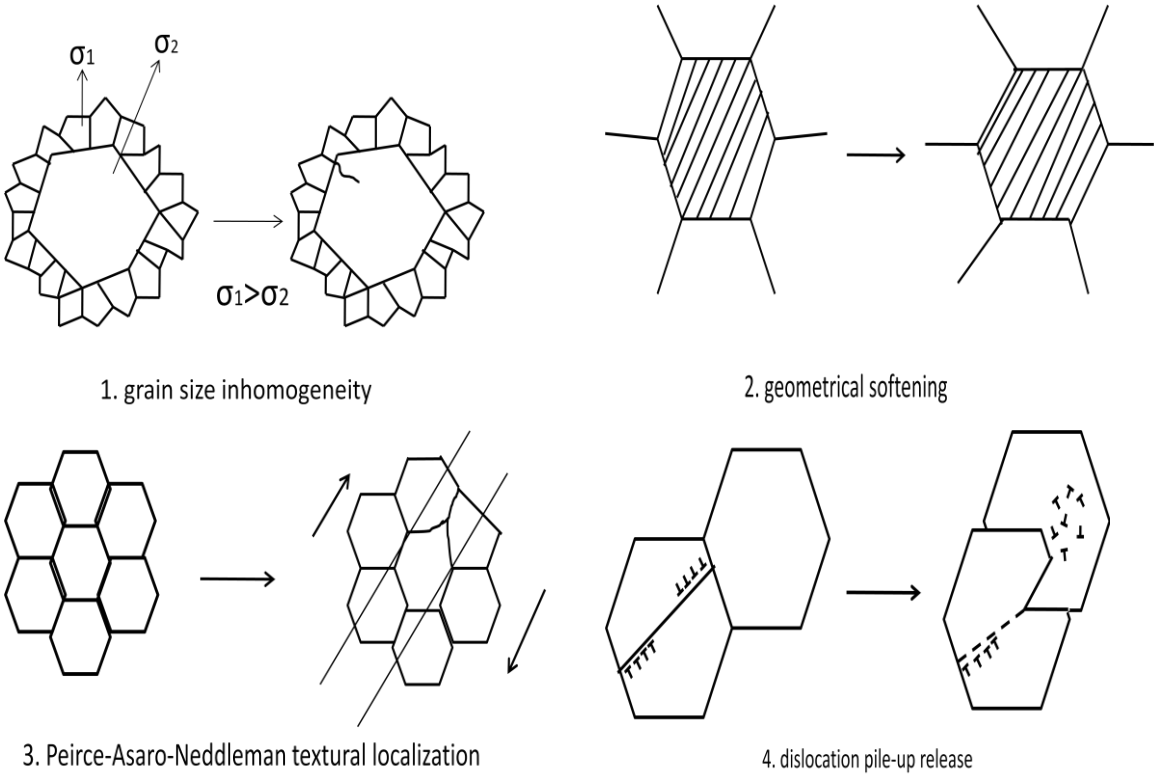

Figure 2.1. Schematic views of possible mechanisms of adiabatic shear band initiation, adapted from [6].

The experimental and numerical study of the effects of notch length and notch root radius on AM50 and Ti6Al4V alloys showed that adiabatic shear band failure is more sensitive to the sharpness of the imperfections than the size of them. Numerical simulation of energy distribution showed a high energy concentration near the notch. The high amount of energy near the notch motivates nucleation of localized ASBs [45].

Specimen's geometry can also influence the occurrence of ASBs in an alloy. For example, a previous study by Li *et al*. [55] showed that shear strain localization did not happen for cylindrical tungsten heavy alloy (WHA), while truncated-conic specimens showed adiabatic shear band formation, which initiated from the upper-right corner to the centre of the opposite surface with the angle of 45˚ to the upper surface of the specimen. It was suggested that adiabatic shearing in the truncated-conic specimens formed as a result of an uneven stress condition along the specimen as well as shear

instability at the critical maximum shear stress. Surface friction was reported to introduce a higher shear stress in the upper-right corner, which suggests that initiation of adiabatic shear bands can be influenced by surface friction.

Several mathematical models including Graddy-Kipp (GP) [56] and Wright Ockendon (OW) models [57] have been proposed for initiation and propagation of adiabatic shear bands. Nesterenko *et al*. [6], in comparing these two models, observed that the experimental results were in a good agreement with theoretical results. They also suggested that initiation of shear band is mostly better represented by the Wright-Ockendon model which is based on the perturbation analysis, while propagation of the shear band is better represented by the Graddy-Kipp model theory which is based on momentum diffusion. They suggested that there is no evidence of diffusion of momentum before shear localization initiation. Diffusion momentum only plays a role during shear localization propagation.

Deformation under dynamic shock loading occurs in stages. Marchand and Duffy [37] suggested that plastic deformation at high strain-rates consists of three stages: homogenous strain hardening, inhomogeneous strain hardening, and deformation localization along narrow adiabatic shear bands. Feng and Bassim [24] and Bassim [34] also suggested the adiabatic shear band formation in AISI 4340 steel occurs in three stages: (1) homogenous elastic deformation, (2) simultaneous occurrence of strain hardening and thermal softening, in which strain hardening is dominant, and (3) thermal softening dominated deformation. Nesterenko *et al*. [38] suggested that localization of deformation occurs once the critical strain for stress collapse is exceeded, which is accompanied by heterogeneous plastic deformation inside the shear band.

2.4. Mechanisms of formation of adiabatic shear bands

There are numerous uncertainties with regards to the mechanism of formation and development of microstructure within adiabatic shear bands. However, several theories have been suggested to explain the mechanism of formation of adiabatic shear bands. These include phase transformation [3, 13, 12, 29, 42], dynamic recovery [32, 38, 58],

dynamic recrystallization [15, 32, 35, 38, 53, 58], and progressive subgrain misorientation [12, 47, 53, 60].

2.4.1. Phase transformation

Phase transformation is one of the earliest theories proposed to explain the occurrence of transformed bands in steels. Zener and Holloman [3] believed that formation of white etching adiabatic shear bands occurs by phase transformation of the room temperature structure to austenite and its subsequent transformation to untempered martensite as a result of quenching by the surrounding materials. Cho *et al*. [61] also considered the white etching bands that form in AISI 4340 steels to be a product of phase transformations leading to the formation of untempered martensite. Chen *et al.* [62] suggested that, for steels which are deformed under dynamic shock loadings, the temperature within adiabatic shear bands can reach up to 1500˚C. At this temperature, phase transformation of ferrite to austenite will occur. Therefore, white etching bands in high strength steels can form as a result of phase transformation from austenite to un-tempered martensite. The measured hardness values of the transformed bands have been observed to be within the range of that for un-tempered martensite [3]. This gives credence to the theory that the constituent of transformed bands is untempered martensite.

The theory of phase transformation accompanying formation of transformed bands is in dispute. Cho *et al*. [13] observed that, at a strain rate around 10^3 s^{-1}, the temperature reaches 600˚C inside the transformed band, formed in HY-100 steel during a high strain-rate deformation. They concluded that, since the temperature inside the shear band did not reach the austenite phase region, the formation of untempered martensite as a result of quenching the austenite inside the white etching band is therefore very unlikely. Zurek [1] observed ultra-fine equi-axed grains inside transformed bands in high strength low alloy steel and suggested that the higher hardness inside the shear band is due to the fine grain size of the transformed band rather than phase transformation. TEM investigation of adiabatic shear bands that form in a Monel alloy under dynamic shock loading by Li *et al*. [43] showed that the shear band has the same structure as the matrix

(FCC), indicating no phase transformation occurred inside the shear band under dynamic shock loading.

2.4.2. Dynamic recovery

Dynamic recovery is one of the suggested mechanisms for the formation of transformed adiabatic shear bands in steels. Chen *et al*. [14] proposed this mechanism for the formation of transformed bands in steel during the fine blanking process, as shown in Fig. 2.2. The mechanism involves elongation and reorientation of grains (ferrite and pearlite) along the applied shear stress flow direction. A dislocation interaction in the elongated grains leads to partitioning into very fine grains through formation of cell walls. The final stage of the dynamic recovery process involves spheroidization resulting in densely packed very fine subgrains inside shear band [14]. Kad *et al*. [19] explained dynamic recovery leading to formation of transformed bands in a zirconium alloy (Zircadine 702) somewhat differently and proposed it to occur in three stages: 1) elongation of cells and subgrains, 2) development of misorientation between neighbouring grains and fragmentation of subgrains to smaller parts, and finally 3) grain rotation due to rotation of grain boundaries resulting in evolution of a fine equi-axed grain microstructure.

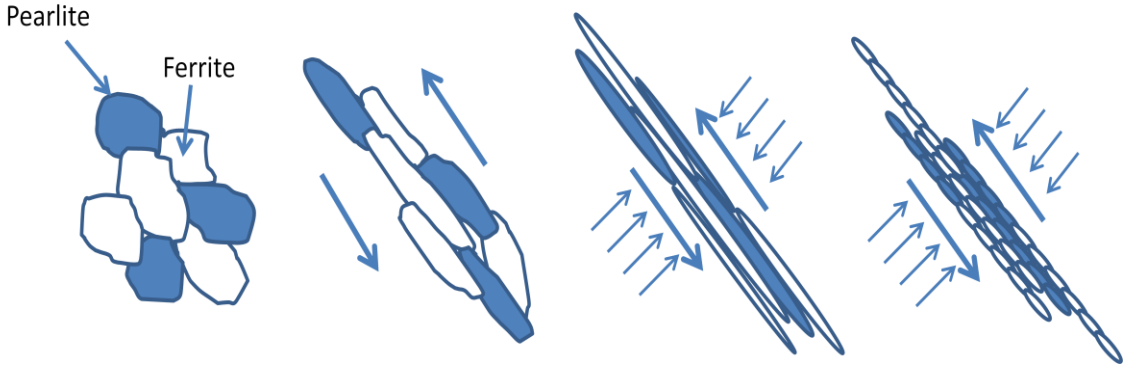

Figure 2.2. Schematic view of dynamic recovery mechanism, adapted from [14].

2.4.3. Dynamic recrystallization

Another mechanism used to explain the grain refinement inside transformed bands is dynamic recrystallization. As a result of the transient nature of the adiabatic shear

banding process, static recrystallization can not justifiably explain the formation of the fine equi-axed grains found in transformed bands. Static recrystallization is diffusion controlled and needs more time to occur than the period of formation of ASB which is of the order of a few hundred microseconds. Meyers *et al.* [15], Barry and Byrne [32], Hines and Vecchio [35], Nesterenko and Meyers [38], Mataya *et al.* [53], and Hwang *et al.* [58] have suggested dynamic recrystallization as the mechanism of formation of transformed bands in metallic alloys. A dynamic recrystallization model, which involves grain boundary diffusion has been suggested by Meyers *et al*. [63]. This model was called Rotational Dynamic Recrystallization and suggested to be much faster than bulk diffusion.

The rotational recrystallization mechanism proposed by Lins *et al*. [60] consists of dislocation multiplication and patterning to form an elongated cell structure, transformation of these cells into elongated subgrains surrounded by lamellar boundaries with high angles (misorientation), and, finally, division of elongated subgrains by formation of boundaries accompanied by local crystal rotation. This sequence of events in dynamic recrystallization was also reported by Li *et al*. [43] and Nesterenko *et al.* [38]. Formation and growth of recrystallized grains under dynamic shock loading inside the shear band depends on the strain-rate and density of dislocations. Atomic thermal migration also controls recrystallized grain growth if the temperature rise within the adiabatic shear band is high enough to allow this [43]. Nesterenko *et al*. [38] summarised the mechanism for dynamic recrystallization, as shown in Fig. 2.3, to occur in 4 stages as follows:

1. Multiplication of dislocations, which are dispersed randomly,
2. Arrangement of dislocations in the form of elongated dislocation cells,
3. Generation of subgrains by dislocation pattering as the deformation progresses, and
4. Break-down of subgrains into equi-axed submicron size grains. As the deformation increases, grain rotation occurs.

Xu *et al*. [33] suggested that the temperature at which recrystallization occurs in metals is about 0.4-0.5 T_m. Andradea *et al*. [36] also observed that temperature rises inside the shear band of the copper specimens were in the range of 500-800K, which is the

temperature range at which recrystallization can occur [36]. However, the calculated temperature inside the shear bands of tantalum subjected to the high strain-rate deformation was about 800˚C, which is lower than the recrystallization temperature. Nevertheless, at high microscopic strains in isolated areas, the onset of recrystallization was observed [15].

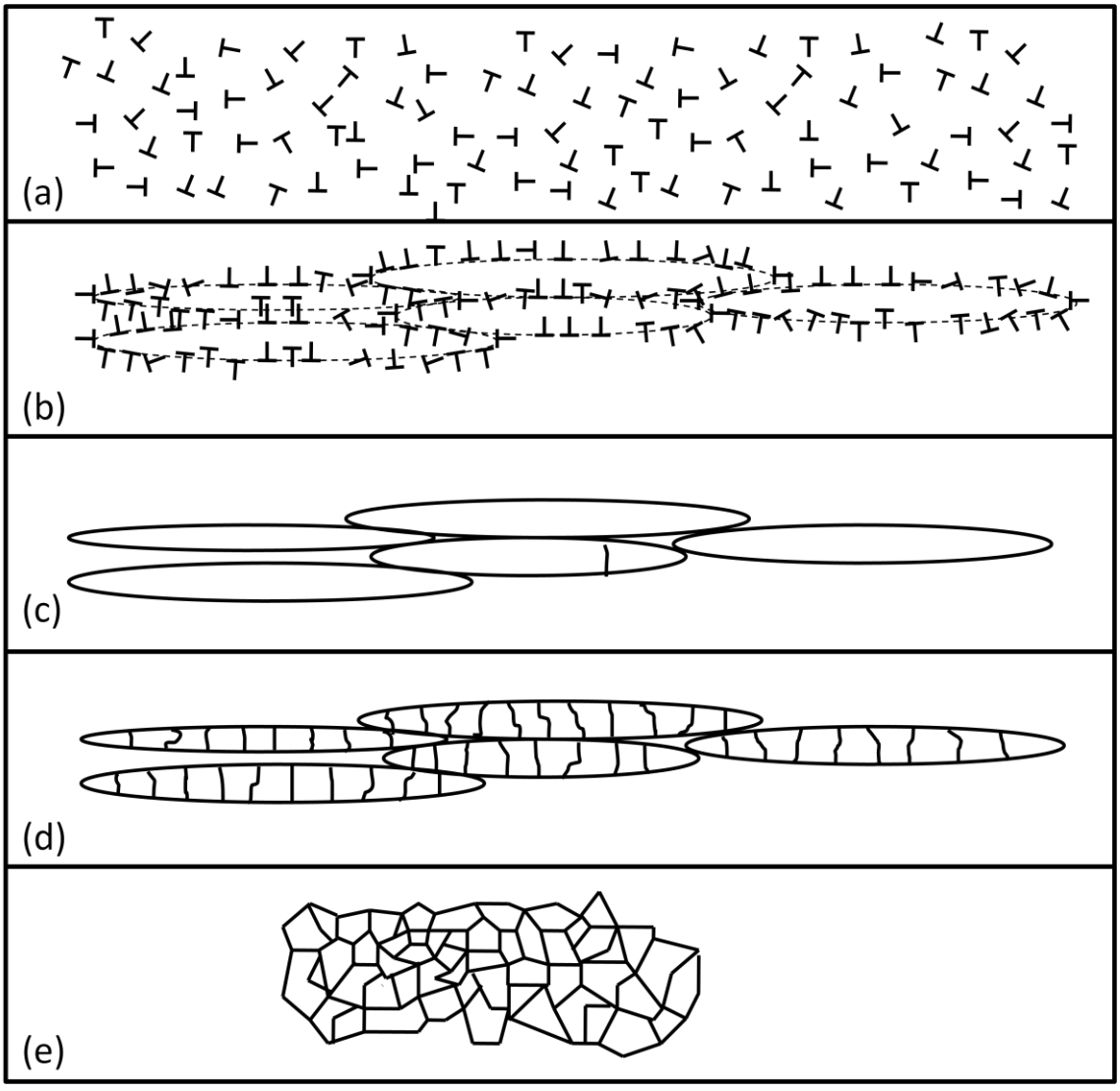

Figure 2.3. Schematic view of dynamic recrystallization mechanism, (a) dislocation multiplication, (b) dislocation patterning forming elongated cells. (c) & (d) formation of subgrains, and (e) breakdown of elongated cells into very fine subgrains. Adapted from [38].

2.4.4. Progressive subgrain misorientation (PriSM)

Progressive Subgrain missorientation (PriSM) has also been suggested for the formation of transformed bands. This involves dynamic recrystallization of grains, which occur by the formation and mechanical rotation of subgrains, followed by boundary refinement during shear band cooling after deformation. Boundary refinement occurs by decreasing the surplus dislocation poles developed mainly by dislocation climb during shear band cooling. During the short period time of deformation, there is not enough time for dislocation annihilation and boundary refinement for the material inside the adiabatic shear band. However, the cooling period, during which the temperature within the adiabatic shear band is still perfectly high, is longer than the deformation period. Therefore, dislocation annihilation and boundary refinement is kinetically possible during the cooling of the transformed band after dynamic shock loading [60]. Hines *et al*. [64] also proposed that the progressive subgrain misorientation recrystallization model accounts for evolution of subgrain misorientation inside the adiabatic shear band. This model is based on a bicrystal approach. Evolution of microstructure inside the shear band is proposed to proceed in two stages: firstly, recrystallization as a result of formation and mechanical rotation of subgrains during the deformation, and secondly, boundary refinement due to the diffusion after deformation and during shear band cooling.

Perezprado *et al*. [65] observed no evidence of dynamic recrystallization within the shear band in hat shaped specimens of Ta and Ta-W alloys that were subjected to dynamic impact loading. They suggested that the temperature rise inside the shear band was not high enough to cause dynamic recrystallization. The Progressive subgrain misorientation (PriSM) mechanism, which is based on the mechanical subgrain rotation, is considered to be a more suitable mechanism to explain the microstructure evolution inside the shear band. Under tested conditions of time and temperature, dynamic recrystallization occurrence is doubtful for this material.

2.5. Microstructure and properties of adiabatic shear bands

Transformed adiabatic shear bands contain very fine, sub-micron size grains with an average size of tenths of micrometers [42]. It is suggested that carbide lamellae inside

the shear bands formed in pearlitic SS400 steel, which was deformed by a fine blanking process, became elongated as a result of intense shear strain inside the shear bands. The elongated carbide lath eventually fragmented into smaller grains which underwent spheroidization forming equi-axed grains. The formation of very fine ferrite subgrains inside the adiabatic shear band was due to the fragmentation of carbide particles as well as compression of carbon and iron diffusion paths under hydrostatic pressure and at high temperatures within the shear band. The hydrostatic pressure inside the adiabatic shear band of the pearlitic SS400 was suggested to hinder the formation of microcracks inside the shear band, although the material inside the shear band is subjected to large shear stresses [14].

TEM investigations of adiabatic shear bands in AISI 4340 steel by Wittman *et al*. [20] showed highly deformed carbide particles with the same structure as the surrounding matrix. They also suggested that partial spheroidization occurs inside the shear band due to the fragmentation of carbide laths, as well as carbon and iron diffusion, which is associated with the nucleation of fine ferrite subgrains. High temperature, as well as shear strain inside the band, cause the fragmentation of carbide particles and accelerate the shear band formation [1]. The adiabatic shear band investigation in tempered martensitic structure of HY-100 steel by Cho *et al*. [13] showed that ASB consisted of two distinctive regions: the highly elongated grains along adiabatic shear bands, and fine equi-axed cells. Derep [67] observed that the microstructure inside the adiabatic shear band in an armour steel after deformation under dynamic shock loading contained a fine grain equi-axed structure of delta ferrite, mixed with narrow laths of martensite. Lesuer *et al*. [68] studied the occurrence of adiabatic shear bands in an ultra-high carbon steel (UHCS) containing 1.3% C, 3.0% Si, 0.5% Mn, 0.99% Cr and observed a mixture of nano-sized carbides and ultra-fine grains of ferrite (70μm size) inside the adiabatic shear band. They suggested that temperature rise inside the shear band caused transformation to austenite followed by rapid cooling, which resulted in divorced eutectoid transformation (DET) after severe plastic deformation (SPD) occurrence inside the shear band. The microstructure inside adiabatic shear bands consisted of nano-sized carbides in super fine grain ferrites (70 μm). They also observed higher hardness in the shear band, compared with other parts of the specimen [68].

Li *et al*. [43] observed fine equi-axed subgrains with the average diameter of 150 nm, as well as low density of dislocations at the center of adiabatic shear bands of a Monel alloy which was subjected to dynamic shock loading using a Split Hopkinson Pressure Bar. TEM observation of 8090 Al–Li alloy subjected to dynamic impact loading showed that the material inside the adiabatic shear band consisted of deformed cells with a high dislocation density, while the deformed region between the matrix and shear band consisted of highly elongated cells with well defined boundaries. On the other hand, the structure at the center of the shear band consisted of very fine equi-axed subgrains with low density of dislocations with the size of about 0.2μm. It is suggested that these equi-axed subgrains were formed as a result of dynamic recrystallization [33].

TEM investigation inside the shear band of 304L stainless steels, which were subjected to dynamic impact loading, indicated the nucleation of ά martensite (ά martensite forms in metastable austenitic stainless-steel by plastic deformation [69]) and the existence of a high density of dislocations inside the shear band. As the strain-rate and stress rate increased, the density of dislocations as well as the fraction of ά martensite inside the shear band increased. Therefore, the density of dislocations and ά martensite formation inside the shear band are sensitive to strain-intensity and strain-rate [70, 71]. Meyers *et al*. [63] also observed the microstructure of adiabatic shear bands in AISI 304L stainless steel (Fe–18%Cr–8%Ni) specimens using Electron Backscatter Diffraction (EBSD) and Transmission Electron Microscopy (TEM). The Electron Backscatter Diffraction (EBSD) results indicated that regions close to the adiabatic shear band experience grain subdivision (size 30μm) with angular rotation up to 20˚. The microstructure inside the shear band could not be detected by EBSD. TEM observation of the microstructure inside the shear band by Meyers *et al*. [63] revealed two regions: 1) a region with grains having an average size of 0.1-0.2 μm, which have low dislocation density and well defined grain boundaries, and 2) a glassy structure region that is formed by a solid-state amorphization process. This was the first time that an amorphous structure has been observed inside a shear band. Stacking faults, twinning, martensitic transformation at twin band intersection and highly plastic deformation were observed outside the shear band. Therefore, it was suggested that plastic deformation and high temperature inside the shear band changes the microstructure from a dislocated and twinned structure to a

submicron size equi-axed structure with well-defined grain boundaries. For the fine grains of an average size of 0.2 μm, grain boundary rotation with the rotation angle of about 30˚ with respect to the estimated deformation time of approximately 10-50 μs has been reported [66].

TEM observations of AISI 316L stainless steel specimens by Xue and Gray[23] showed well-defined adiabatic shear bands with a mixture of equi-axed, rectangular or elliptical, and elongated subgrains. They observed elongated subgrain laths and a high density of dislocation at the peripheral region of the transformed band, while fine equi-axed subgrains with the average size of 100 nm were observed inside the core of the shear band. The fine equi-axed grains were proposed to form as a result of fragmentation of elongated laths or subcells reconstruction by patterning of the high density of dislocations generated inside the shear bands. As the deformation increased, the adiabatic shear band core width increased and consequently the width of region with elongated subgrains decreased [23].

TEM observations by Hwang *et al*. [58] on low-carbon steel plates that were subjected to dynamic shock loadings using torsional Kolsky bar, showed elongated ferrite and very fine equi-axed ferrite inside the shear band. Realignment of dislocations inside the elongated ferrites by dynamic recovery generated cell structures with very fine equi-axed grains with the average size of 0.05-0.2 μm. The dynamic recrystallization mechanism was suggested as a possible mechanism which developed these high- angle sub-grains with relatively low density of dislocations. It was suggested that cementite particles inside the shear band were fragmented into smaller particles and spheroidized. Spheroidized cementite particles pinned down ferrite grain boundaries and hindered ferrite grain growth. Therefore, ferrite particles inside pearlite inside the adiabatic shear band were finer than those outside the pearlite [58]. The investigation of the effects of deformation temperature, strain rate, and preshocking condition on the formation of adiabatic shear bands by Chen *et al.* [66] in tantalum specimens that were subjected to dynamic shock loadings showed that as the deformation temperature decreased, shear localization increased due to the lower heat capacity . It also has been observed that as the strain rate increased, shear localization increased due to the higher heat generation

inside the material. As the temperature decreased and strain rate increased, the width of the shear band decreased. They also observed that specimens in preshock conditionings were more incline to form shear localization [66].

TEM investigation of the white etching bands in a Ti–6Al–4V alloy also showed the existence of equi-axed grains with the diameter of 50 nm inside the shear band [44]. Optical and transmission electron microscopy of adiabatic shear band in Ti-6Al-4V by Me-Bar and Shechtman [46] showed that the temperature rise inside the adiabatic shear band as a result of plastic deformation caused melting of the alloy in some regions besides the transformation from α phase to β phase that is followed by swift cooling at a rate of $170^{\circ}Cs^{-1}$. The regions, where melting of the alloys occurred, were totally distorted, while the regions with β phase were elongated along the shear flow direction [46]. As a result of temperature rise inside adiabatic shear band of Ti-6Al-4V, and intense localized plastic deformation, completely distorted regions were observed inside the shear bands which had an entirely different microstructure from the parent alloy. This microstructure was suggested to be a tempered form of ά parental microstructure [72]. Small grains with an average size of 0.3-0.5 μm were observed inside the shear band of titanium, while the regions close to the shear band showed a high density of dislocations and deformation twinning. The boundary region between matrix and shear band of commercially pure titanium subjected to dynamic shock loadings consisted of slip bands and their intersections. Fine equi-axed submicron size grains were observed inside the shear band [30].

Submicron size grains with the average size of 0.1 μm were observed inside adiabatic shear bands formed in copper that was rapidly deformed; the fine grain structure of the shear bands were proposed to form as a result of dynamic recrystallization [36]. Hines and Vecchio [35] investigated the adiabatic shear bands in copper and observed small grains with the average size of 0.1-0.2μm inside the adiabatic shear band. Copper samples that were deformed in liquid nitrogen at sub zero degree temperature exhibited no temperature-dependence of recrystallization [35].

Lee *et al*. [70] observed dislocation and twinning deformation inside the adiabatic shear band of inconel 690 superalloy specimens subjected to dynamic impact loading. They

observed that dislocations were arranged in a form of dislocation tangle and caused the formation of dislocation cell walls. It was observed that, as the test temperature increased, dislocation annihilation occurred, and the density of dislocation decreased. On the other hand, increasing strain-rate led to an increase in dislocation and twinning densities. Therefore, under high strain-rate loading and at low temperature, smaller dislocation cell size with thicker walls were formed which hindered the dislocation motion. Lee and his colleagues observed that, as the temperature increased at a constant strain rate, the flow stress, strain-rate sensitivity, and work hardening coefficient decreased, while activation volume and temperature sensitivity increased. However, as the strain-rate increased at a constant temperature, the flow stress and strain-rate sensitivity increased, while the activation volume and work hardening coefficient decreased [70].

Nesterenko *et al*. [38] observed four kinds of microstructure in a deformed specimen of tantalum: (1) at effective strain values of less than 1 and a calculated temperature less than 600K, dislocations and elongated dislocation cells were observed, (2) at effective strain values of between 1 and 2 and a calculated temperature of 600-800 K, subgrain formation occurred by dynamic recovery, (3) dynamically recrystallized micrograins were observed for the effective strain between 2 and 2.5 and a calculated temperature of between 800 and 900K, and they were proposed to form by dynamic recrystallization, and (4) at effective strains higher than 2.5 and a temperature higher than 1000K post-deformation recrystallized grains were observed which were suggested to form by static recrystallization. It has also been suggested that static recrystallization involves an atomic migrational mechanism, while dynamic recrystallization involves subgrain rotation and dislocation annihilation. Microscopic analysis of tantalum samples that were deformed at high strain-rates by Meyers *et al*. [15] showed subgrains at the centre of adiabatic shear bands where the shear strain was 5.5. Elongated cells were observed in the boundary region between the shear band and the bulk material. Under transmission electron microscope, twinning deformation has been observed inside the adiabatic shear band of a low carbon steel with pearlite particles of 18 μm. However, there was no twinning deformation inside the adiabatic shear band of medium and high

carbon steel with the pearlite particle size of 25 and 35 μm, respectively. It has been suggested that grain boundaries restrict twinning deformation [71].

TEM observation of adiabatic shear bands in AISI 4340 VAR steel with hardness of 44 HRC showed highly elongated subgrains with well defined boundaries and varied dislocation densities, as well as dislocation cells. There was no evidence of phase transformation inside the adiabatic shear band. The preferred orientation of these subgrains was calculated at 110 planes which were parallel to the shear direction [17]. Meyers and Wittman [26] reported that hardness of transformed bands observed in quench-hardened and tempered low-carbon steels (AISI 1018 and 8620) were significantly higher than that of untransformed matrix. It has been suggested that this higher hardness of ASB is due to the fine microstructure with supersaturated carbon. It has been suggested that hardness inside the transformed band of steels depends on the carbon concentration [61].

Lee *et al*. [50] studied microstructural evolution inside adiabatic shear bands for three aluminum alloys: AA 2090 Al-Li alloy, a weldalite 049TM alloy and AA 7039 Al. They observed that the microstructure of the adiabatic shear band was totally different in the 2090 Al-Li alloy. It contained highly elongated grains and coarse grain boundary particles. The cracks propagated along the grain boundaries with coarse particles (intergranular cracking). These intergranular cracks may prevent adiabatic shear band formation.

Hat shape specimens of a polycrystalline zirconium alloy (Zircadine 702, containing 0.7% Hf), which were impacted under dynamic shock loadings by Split Hopkinson Bar, exhibited well-defined adiabatic shear bands with the average width of 9-24μm in all tested specimens. The equi-axed grains with the average size of 200 nm were observed inside the shear band. Grains near the adiabatic shear band were subjected to moderate deformation and aligned themselves along the shear direction [19].

Shear localization occurred for granular materials such as silicon carbide powders under high strain rate deformation. Comminution and rearrangement of particles were the suggested deformation mechanism of adiabatic shear bands in granular ceramic

materials. Plastic deformation of SiC particles caused the temperature to rise inside the shear band which melted SiC particles inside the shear band and fused them together [41]. Nesterenko *et al*. [73] investigated the effect of particle size of densified granular alumina specimens which were subjected to dynamic shock loadings by thick-walled cylinders on the adiabatic shear band characteristics. They observed that adiabatic shear band width was independent of initial particle size and was approximately 10-20μm. However, the microstructure of adiabatic shear bands significantly depended on the initial particle size. Specimens with the initial particle size of 4μm, experienced comminution (break-up) and particle softening, while observations of those with particle size of 0.4 μm showed a network of cracks parallel and perpendicular to the shear band. Initial particle size significantly affected displacement, magnitudes and distribution of adiabatic shear bands due to the different softening mechanism. Hardness of adiabatic shear bands increased in both specimens with small and big granular particle sizes. They suggested that specimens with large grain size had higher hardness due to an occurrence of microfracture, followed by repacking of particles with different sizes. Meanwhile, small size initial particles just underwent classic repacking and not particle fracturing.

Meyers *et al*. [63] observed the adiabatic shear bands in metals (Ti, Ta, Ti-6Al-4V, and stainless steel), granular and pre-fractured ceramics ($Al_2O_3$and SiC), a polymer (teflon), and a metallic glass ($Co_{58}Ni_{10}Fe_5Si_{11}B_{16}$). They suggested that the microstructure evolution mechanisms for each group were as follows:

1. Metals: The first stage of deformation is associated with thermal softening following by dynamic recovery and dynamic recrystallization. It was proposed that, during the high strain-rate deformation, subgrain fragmentation and grain boundary rotation can occur.

2. Ceramics: Shear localization depends on the particle size. If the particle size is greater than a critical value a_C, comminution and particle break-up will occur. However, if the particle size is smaller than critical value, a significant amount of heat that is generated by plastic deformation and particle repacking will cause the fusion of the particles and bonding.

3. Non-crystalline metals and polymers: Local inelastic transformations initiated the highly localized regions which organized themselves into shear band zones.

The width of the region in which the grain distortions are clear, in comparison with other parts of the specimen, is called the width of the shear band. The width of the shear band depends on the materials, chemical compositions and strain rate [71]. Xue-bin [74] suggested that wide transformed adiabatic shear bands, as well as high local plastic deformation between deformed and transformed ASB, are formed as a result of a high heat conversion factor, low density, low heat capacity and high melting temperature. High local plastic deformation in deformed adiabatic shear band forms when there is a high work to heat conversion factor, low density, low heat capacity and low melting point. They also suggested that difference in materials investigated, loading methods, conditions, and different definitions of the ASB width are three reasons responsible for the scatter in experimental results on the width of the shear bands [74]. It has been observed that the width of the shear band in steels decreased as the carbon content and strain rate increased [71].

The local shear strain within an adiabatic shear band is defined as $\gamma = \tan\theta$ where θ is the distortion angle [33]. As the distance from the centre of the shear band increases, the distortion angle decreases. Therefore, the maximum local shear strain occurs at the centre of the adiabatic shear band. The angle of distortion and local shear strains depend on the material, chemical composition and strain rate. It has been observed that for steels, as the amount of carbon and strain rate increased, the local shear strain increased [71]. Engineering strain can be calculated from the true strain using Equation 2.7 [33]:

$$\varepsilon = \sqrt{1 + \gamma + \gamma^2} \tag{2.7}$$

2.6. Adiabatic shear band failure

Materials fail along the adiabatic shear bands under dynamic impact loadings. Adiabatic shear bands are preferential sites for crack initiation and propagation [47, 75]. As the loading rate increased, the temperature inside of the shear band increased, which has significant effects on material yielding and plasticity. The optical and scanning electron microscopic observations of roll homogeneous armour (RHA) plate by Raftenberg and

Krause [31], perforated by a pointed projectile, showed the existence of some cracks along the transformed shear bands blended with deformed adiabatic shear bands along the indentation cavity of the plates. Zurek [1] also observed a ductile fracture mode inside the white etching adiabatic shear band of pearlitic AISI 4340 steel. Mataya *et al*. [53] observed macroscopic, transgranular cracks inside the shear band of γ' strengthened austenitic stainless steel, JBK-75. Cho *et al*. [61] suggested that crack formation along the adiabatic shear band of AISI 1018 cold-rolled steel occurred in three stages: (1) formation and coalescence of micro-voids and separation along ferrite boundaries, (2) separation between pearlite and ferrite particles, and (3) breaking apart of pearlite lamellae. They also observed that, for HY-100 steel, voids initiated at MnS inclusions inside the adiabatic shear band.

The schematic view of the crack formation and propagation mechanism inside adiabatic shear band, as proposed by Bassim and Odeshi [76] for quench-hardened and tempered AISI 4340 steel is shown in Fig. 2.4. It was suggested that the formation of cracks along adiabatic shear bands starts with the formation of micro-pores inside the adiabatic shear bands (Fig. 2.4a). These micro-pores cluster together, forming voids, which act as crack nuclei. The micro-cracks, nucleated at adjacent voids interconnect leading to formation of crack, as shown in Fig. 2.4(d) [76]. Rittel *et al*. [45] suggested that voids' nucleation occurs because of 1) vacancy coalescence at high strain-rate regions, 2) formation of micro-voids because of grain boundary sliding, and 3) void nucleation at secondary-phase particles and ahead of dislocation pile-ups. It has been reported that the existence of precipitates are not a necessary factor for void nucleation [45].

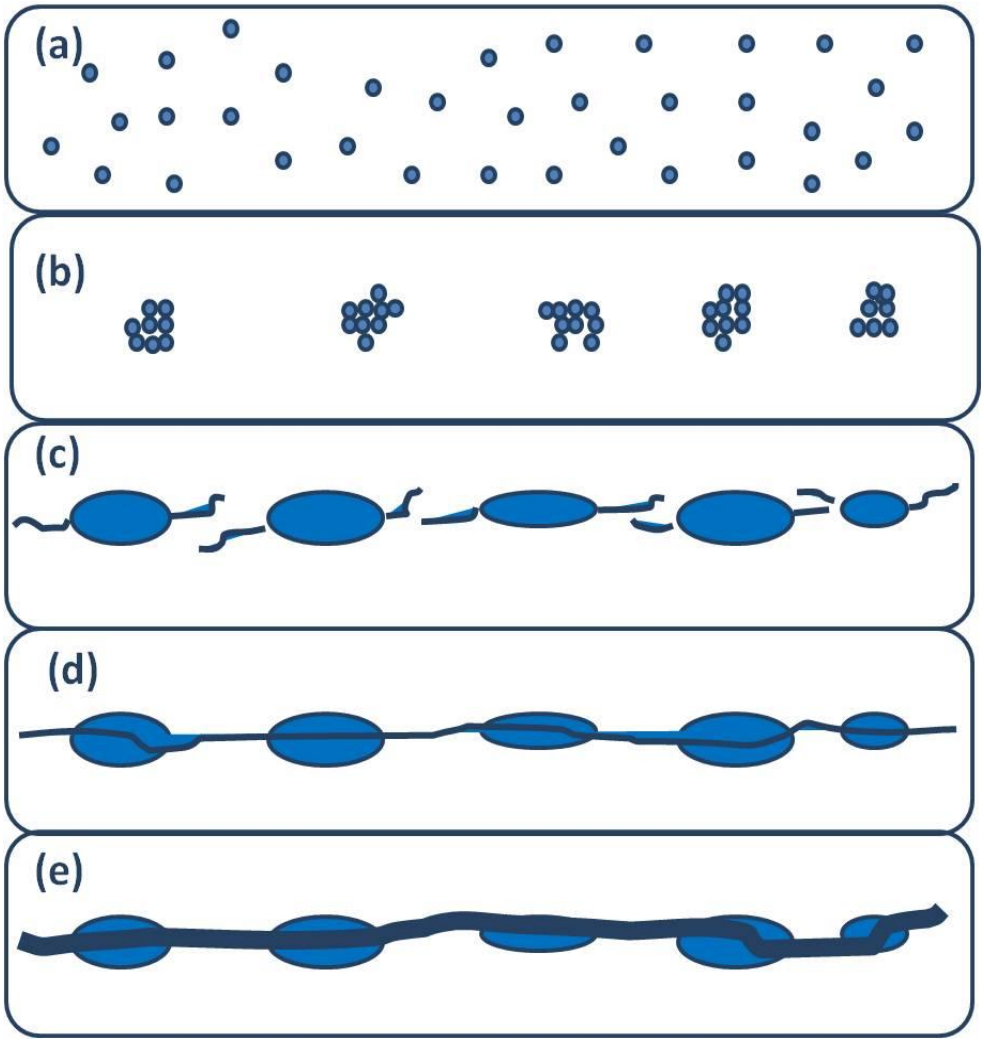

Fig. 2.4. Schematic view of crack formation inside adiabatic shear band, adapted from [76].

Xue *et al*. [77] studied the failure of adiabatic shear bands in Ti–6Al–4V alloys. They proposed a model for the evolution of a crack inside shear bands as shown schematically in Fig. 2.5. They suggested that voids nucleate inside the shear band. Odeshi *et al*. [78] suggested that micro-voids nucleate inside adiabatic shear bands as result of tensile stress generation due to the difference between the flow stress inside and outside the shear bands. These voids grow until they reach the shear band boundary where the material is harder due to the lower temperature. Xue et al. [77] proposed that these voids grow along the shear bands, and finally coalesce, causing fragmentation. The schematic views of the mechanisms proposed by Xue and his colleagues [77] in the absence and

presence of shear stress are presented in Fig. 2.5. In the presence of shear stress, the voids are elongated and rotated as shown in Fig 2.5(b) [77].

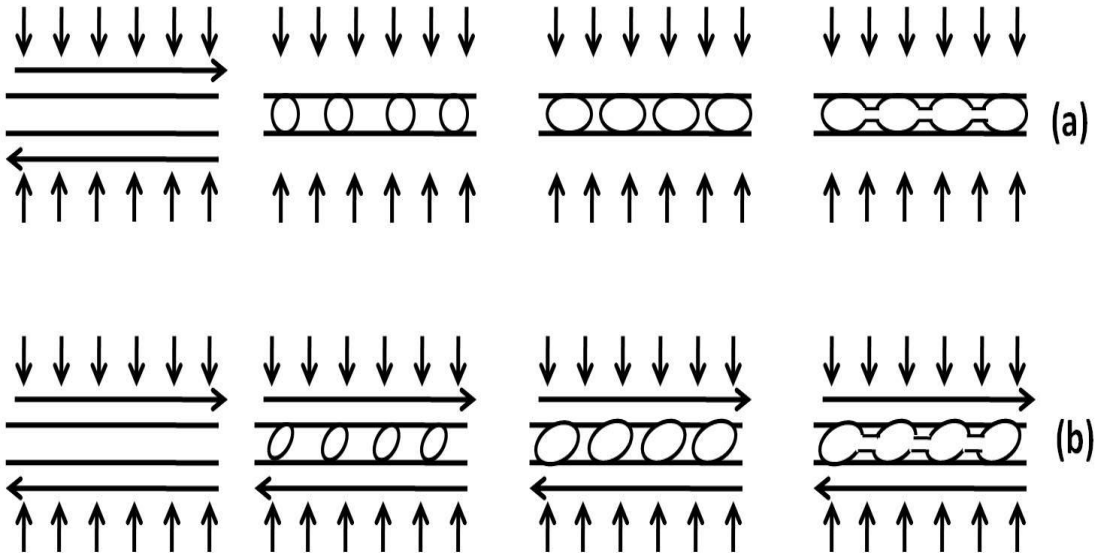

Figure 2.5. Schematic view of voids nucleation inside the shear band, (a) in the absence of shear stress, (b) in the presence of shear stress, adapted from [77].

A ductile fracture mode has been observed inside and outside the shear band. Ductile fracture inside the shear band occurred as a result of thermal softening which created tensile stress and opened up micro-voids inside the adiabatic shear band. On the other hand, ductile fracture outside the shear band occurred as a result of precipitates, which act as crack nuclei [45]. Nesterenko *et al*. [38] suggested that ductile fracture along the adiabatic shear band of deformed tantalum was due to the residual tensile tangential stresses upon loading. Cho *et al*. [61] observed elongated dimples and knobby features on the fracture surface of an AISI 1018 cold-rolled steel (CRS), a structural steel (HY-100), and an AISI 4340 vacuum arc remelted (VAR) steel tempered to either of two hardnesses RHC 44 or 55. They observed elongated dimples, indicating ductile shear fracture mode. They also observed knobby features on the fracture surface, suggesting melting of alloy in these regions. The fracture surface of the specimen could melt as a result of heat generation inside the adiabatic shear band as the two fracture surfaces are rubbed against one another [42, 61].

Odeshi and Bassim [11] observed ductile fracture with the evidence of precipitates at voids' origin in bulk material of AISI 4340 steel, which was deformed under dynamic shock loadings. However, both ductile and cleavage fracture were reported to occur outside the shear band of AISI 4340 steel. Elongated dimples as a result of ductile fracture mode were observed in the deformed zone between the bulk material and transformed band. Fracture along transformed bands showed highly elongated dimples indicating shear ductile fracture and knobby fracture mode. The dimples were deeper and narrower inside the transformed shear band than dimples formed in deformed bands in the region adjacent to the transformed band [11]. Lee *et al*. [70] also observed dimples on the fracture path through adiabatic shear band in inconel 690 superalloy subjected to dynamic impact loading.

Lee and Lin [71] also observed both elongated dimples and knobby features on the fracture surface of adiabatic shear band in low, medium, and high carbon steels. It has been observed that as the strain-rate increased, the depth of the dimples increased and the shear band exhibited more ductile fracture. This indicated that as the strain-rate increased, the temperature within adiabatic shear band increased. Moreover, the proportion of knobby features increased as strain rate and carbon content increased, and the size of dimples decreased with increasing strain rate and carbon content [71].

Ryttberg *et al*. [79] proposed three damage subzones to form below the fracture surface of 100Cr6 steel that fractured under impact shock loadings: 1) white etching band, 2) equiaxed grains, and 3) elongated subgrains (The preferred orientation of subgrains was 110 planes parallel to the shear direction). It was also observed that the region below the fracture surface of tool steel 100CrMn6 was divided into three zone: 1) right under the fracture surface, white etching adiabatic shear band containing equi-axed ferrite particles (size. 50-150 nm); 2) within a distance less than 50 μm under the fracture surface, lamellae cementite and carbide particles within ferrite matrix, and 3) within the range of 50-100 μm distance under the fracture surface, elongated grains, distorted carbide lamellae with small lamellar spacing which align themselves parallel to the shearing direction. Evidence of deformation twinning of each region was reported [79].

2.7. Adiabatic shear band recovery

The susceptibility of the material to fracture under subsequent loading can be reduced by the annealing shear band that developed in the previous dynamic shock loading. Odeshi *et al*. [21] investigated the effects of post-impact heat treatment on the adiabatic shear band in AISI 4340, which were formed under dynamic impact loading. It was observed that annealing the white etching band at 315˚C for 2h did not affect the microstructure inside the shear band. However, hardness value of the shear band decreased by soaking the specimen band at 650˚C for 20 minutes. By soaking the specimen at 650˚C for 20 minutes the hardness value of the shear band decreased to the same value as that of the material outside the shear band. By extending the soaking time at 650 °C to 2h, the white ASB changed to a gray colour of the ductile deformed band. Coarsening of nano-sized particles inside the adiabatic shear band was observed to occur, which accounted for the reduced hardness of the shear band when soaked at 650 °C for 20 minutes.

2.8. Summary

At strain rate greater than $10^3 s^{-1}$, deformation become localized along narrow bands in materials. The narrow paths of intense strain localizations are called Adiabatic Shear Bands (ASBs). Materials fragmentation under high strain-rate is usually preceded with the occurrence of adiabatic shear bands, especially transformed bands which contained nano-sized subgrains and offer preferential sites for crack initiation and propagation. Therefore, fundamental understanding of the mechanisms of formation these bands and their failure is very important to prevent adiabatic shear failure of engineering components under dynamic shock loadings. It is very important to investigate and document the dynamic impact response of various engineering materials in relation to adiabatic shear banding as influenced by microstructure, strain rates and geometry. Although mechanical properties of most engineering alloys under static loading are readily available in the literature, the same cannot be said for the case of dynamic shock loading. The need to generate property data sheets for all materials and make them readily available for the use of design engineers in materials selection for high strain-rate applications cannot be overemphasized.

The current study was conducted to document the dynamic mechanical response and adiabatic shear banding in AISI 1340 steel as influenced by strain rates, microstructure and specimen's geometry. The dynamic mechanical behaviour of the alloy specimens heat-treated to have martensitic, pearlitic and dual-phase structure will be investigated. Such a detailed investigation of AISI 1340 steel under dynamic impact loading has not been previously conducted. The results to be obtained from this investigation will contribute to knowledge on dynamic impact behaviour of this alloy and to generation of materials database for dynamic mechanical behaviour of the material. Although AISI 4340, the second alloy intended for investigation in this research study, have been investigated by a number of researchers [1, 11,12, 20,21], the effects of geometry of the on the occurrence and trajectory of adiabatic shear bands in the steel has not been investigated as planned in this research study.

In order to provide further insight to the microstructural evolution that culminates in the occurrence of transformed bands in steel, chemical analyses of the regions inside and outside these bands are planned for investigation using the synchrotron light radiations at the Canadian Light Source (CLS) in Saskatoon. The investigation will be carried out at the soft x-ray spectromicroscopic (SM) beamline of the CLS using X-ray Photoemission electron microscopy (XPEEM) and Near edge X-ray absorption Fine Structure (NEXAFS). Such an in-depth chemical analysis of the nano-grains inside transformed bands in metallic materials has not been previously undertaken as planned. Data to be generated from synchrotron study of transformed band will likely open a new line of discourse on the microstructural evolution associated with the occurrence of transformed bands in steel in particular and metallic alloys in general.

CHAPTER THREE
MATERIALS AND EXPERIMENTAL PROCEDURE

The materials used in this investigation, the geometry of the specimens, heat treatment procedure, high strain-rate deformation tests (Direct impact Hopkinson Bar test, Torsional Kolsky Bar test) are explained in this chapter. Metallographic preparation and procedures for microstructure analysis using Optical Microscopy (OM), Scanning Electron Microscopy (SEM), X-ray Photoemission electron Microscopy (XPEEM), and microhardness testing are also provided in this chapter.

3.1. Materials

The chemical compositions of AISI 1340 and 4340 steel used in this investigation are shown in Table 3.1. The AISI 1340 steel was supplied by Stelco Inc. in Hamilton Ontario (now called US steel Canada), which also provided the chemical composition of the steel. AISI 4340 steel was purchased from steel vendor by mechanical engineering workshop in college of engineering at University of Saskatchewan. The chemical composition range of AISI 4340 was looked up in ASM handbook volume 1 [82]. They both contain 0.40 wt. % C. whereas AISI 1340 steel is manganese steel containing 1.54 wt. % Mn and 0.14 wt. % V, the AISI 4340 steel is a low alloy steel containing substantial amounts of Mn, Cr and Mo. AISI 4340 steel is one of the most popular High-Strength Low Alloy (HSLA) steels, and is commonly used in high strength applications in automobiles and trucks, gas pipelines, pressure vessels, etc. The low carbon content and high manganese content of AISI 1340 steel makes it suitable for processing into dual-phase structure. The manganese expands the ferrite + austenite phase region in the iron-iron carbide equilibrium phase diagram and the low carbon content enhances the ability to partially austenitize the steel in the ferrite + austenite phase region. On quenching the steel after intercritical annealing in the ferrite + austenite phase region, the austenite will transform, leaving a microstructure that consists of hard martensite embedded in a continuous soft ferrite matrix. The high manganese content and high carbon content of the austenite in the intercritical temperature range provides enough

hardenability for the transforming austenite [82]. As a result of the unique combination of good strength and ductility in dual-phase steel, it can be rolled into high strength thin plates suitable for automobile bodywork. Thus, AISI 1340 steel is widely used in automotive body construction to enable cars to save weight and consume less fuel [82].

Table 3.1. Chemical compositions of AISI 1340 and 4340 carbon steels

Elements	AISI 1340 steel (wt%)	AISI 4340 steel (wt%)
C	.40	.40
Mn	1.54	0.60-0.80
P	.022	0.035
S	.015	0.04
Si	.27	0.15-0.30
Cu	.009	-
Ni	.012	1.65−2.00
Cr	.050	0.70-0.90
Mo	.002	0.20-0.30
V	.14	-
Cb	.068	-
Ti	.002	-
Ni	.012	1.65-2.00

3.1.1. Specimens

The geometry of the test samples are shown in Figs. 3.1 and 3.2. Samples for torsional tests were machined from hot-rolled AISI 1340 and 4340 steel rods into thin-walled tubular specimens with a gage length of 3.8 mm and wall thickness of 0.4 mm (Fig. 3.1). The compression specimens investigated with direct impact Hopkinson, which were machined from the hot-rolled rods of AISI 1340 and 4340 steels, were in three shapes: cylinder, cube, and truncated cone as shown in Fig. 3.2. The cylindrical specimens had a diameter and length of 9.5 mm and 10.5mm, respectively. The cubical-shape specimens had dimensions 9.00 mm × 9.00 mm × 10.00 mm. The specimens machined

into the shape of a truncated cone had radii of 9.5 mm and 8.5 mm, and a height of 10.5 mm.

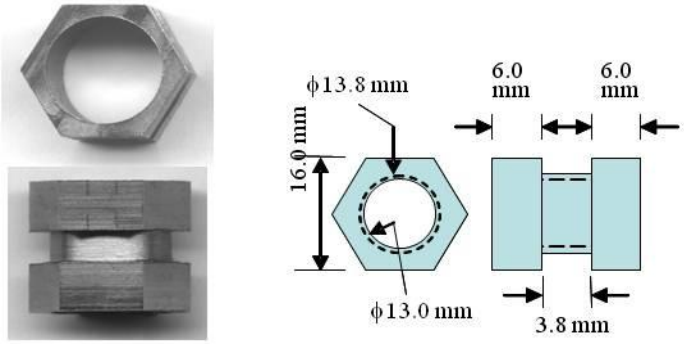

Figure 3.1. Thin-walled tubular specimens for torsion test.

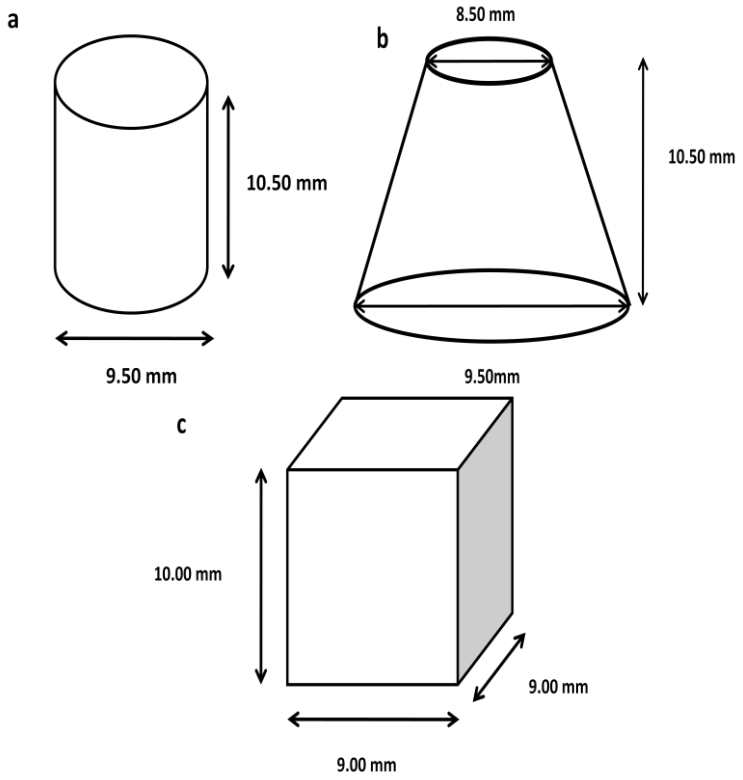

Figure 3.2. Specimens′ shape (a) cylinder, (b) cone, (c) cube.

3.2. Experimental Procedure

3.2.1. Heat treatment Procedure

In order to determine the effects of microstructure on the dynamic impact response of the alloys, machined specimens were heat-treated to obtain pearlitic, martensitic or dual phase structures. The heat treatment procedures with respect to temperature, time and quench medium is summarized in Table 3.2. The heat treatment temperature was designed using the iron-iron carbide equilibrium phase diagram shown in Fig. 3.3. To obtain martensitic structure, steel specimens having 0.4 wt. % C were austenitized at 850˚C for 30 minutes using Linderg blue Furnace located in College of Engineering (Room 2C24), University of Saskatchewan and then quenched in water, in the case of AISI 1340 steel or oil in the case of AISI 4340 steel to obtain martensitic structure. The cylindrical martensitic AISI 1340 steel specimens were divided into three groups, tempered at 205˚C, 315˚C or 425˚C, respectively, for one hour. AISI 4340 steel specimens were tempered at only 315˚C for one hour. The effect of tempering temperature on the AISI 4340 has been investigated in a previous study [11, 21, 83]. To obtain pearlitic structure, specimens were austenitized at 850˚C for 30 minutes and then cooled down to the room temperature in air. The microstructure at room temperature consisted of ferrite and pearlite. Dual-phase structure was obtained by austenitizing the specimens at 740˚C in the ferrite + austenite phase region (Fig. 3.3) for 20 minutes and then quenching in water in the case of AISI 1340 steel or oil in the case of AISI 4340 steel. These specimens were then tempered at 315˚C for one hour.

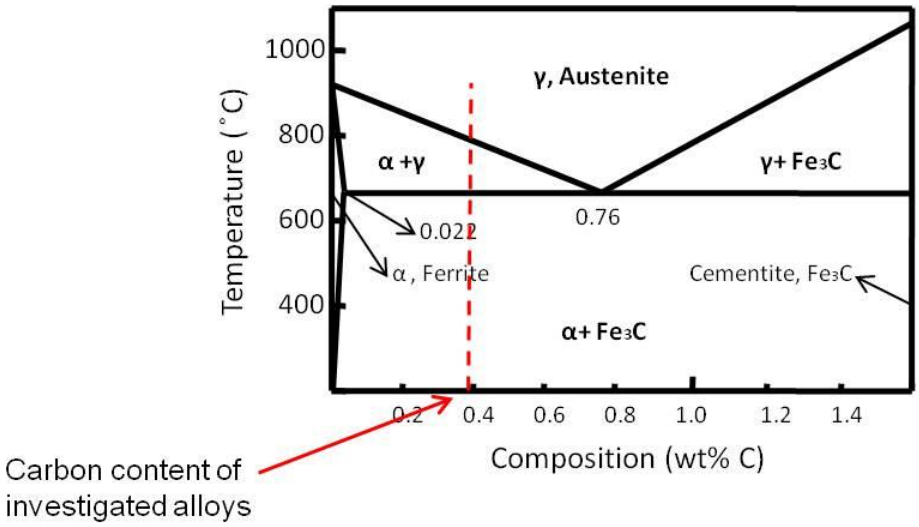

Figure 3.3. Iron-iron carbide phase diagram.

Table. 3.2. Summary of heat treatment procedure

AISI 1340 Steel

Microstructure	**Austenitizing Temperature (˚C)**	**Time (min)**	**Quench**	**Tempering Temperature (˚C)**	**Number of Specimens**	
					Impact Test	Torsion Test
Martensitic	850	30	In Water	205 (1 hr)	Cylinder 10	-
	850	30	In Water	315(1 hr)	Cylinder 10 Cube 6 Cone 6	3
	850	30	In Water	425(1 hr)	Cylinder 10	-
DP Structure	740	20	In Water	315(1 hr)	Cylinder 10	3
Pearlitic	850	30	In air	-	Cylinder 10	3

AISI 4340 Steel

Microstructure	**Austenitizing Temperature (˚C)**	**Time (min)**	**Quench**	**Tempering Temperature (˚C)**	**Number of Specimens**	
					Impact Test	Impact Test
Martensitic	850	30	In oil	315(1 hr)	Cylinder 4 Cube 6 Cone 6	3
DP Structure	740	20	In oil	315(1 hr)	Cylinder 4	3
Pearlitic	850	30	In air	-	Cylinder 4	3

3.2.2. High strain-rate tests

3.2.2.1. Compression test

The dynamic mechanical behaviour of the materials under compressive loading at high strain rate was investigated using an instrumented Direct Impact Hopkinson Bar. Figure 3.4 shows a schematic view of the direct impact Hopkinson Bar and a photograph of the direct impact Hopkinson Bar used in this investigation, which is located in Department of Manufacturing and Mechanical Engineering at University of Manitoba, is shown in Fig. 3.5. The projectile, which is fired by the light gun, travels through the gun barrel and strikes the sample at high impact velocity. The projectile was fired at varying firing pressure to produce projectile velocities that ranged between 20 and 32 m/s at the time it struck the specimen. The projectile was made of quench-hardened AISI 4340 steel and weighed 1.905 kg. As the specimen was impacted by the projectile, elastic waves were produced, which transmitted through the specimen to the output bar. The transmitted elastic wave signals were captured by a strain gage attached to the output bar. The captured strain waves were conditioned and amplified by the attached strain pulse amplifier. The amplified strain pulse data were recorded using a mixed signal digital oscilloscope.

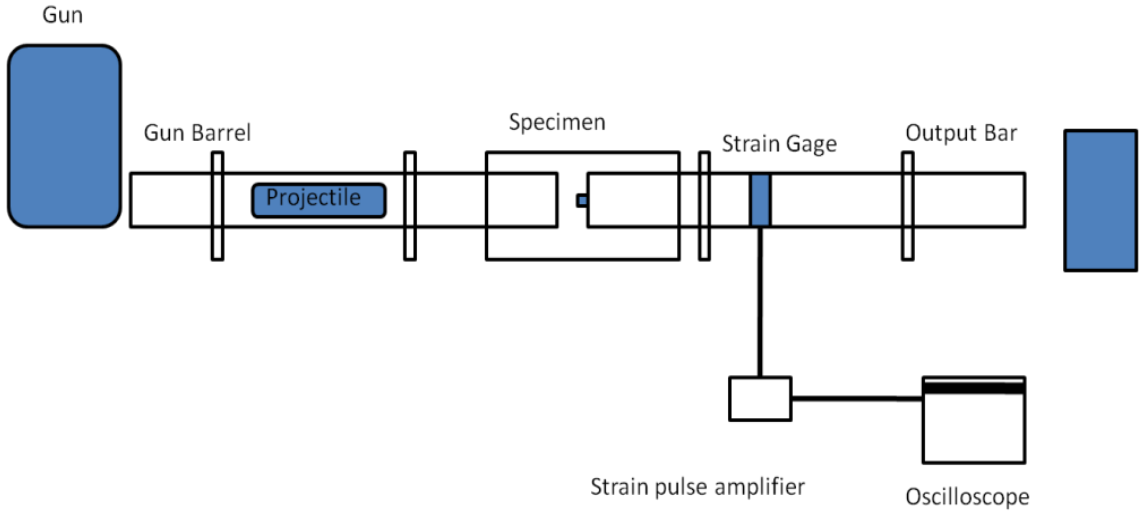

Figure 3.4. Schematic view of the direct impact Hopkinson bar.

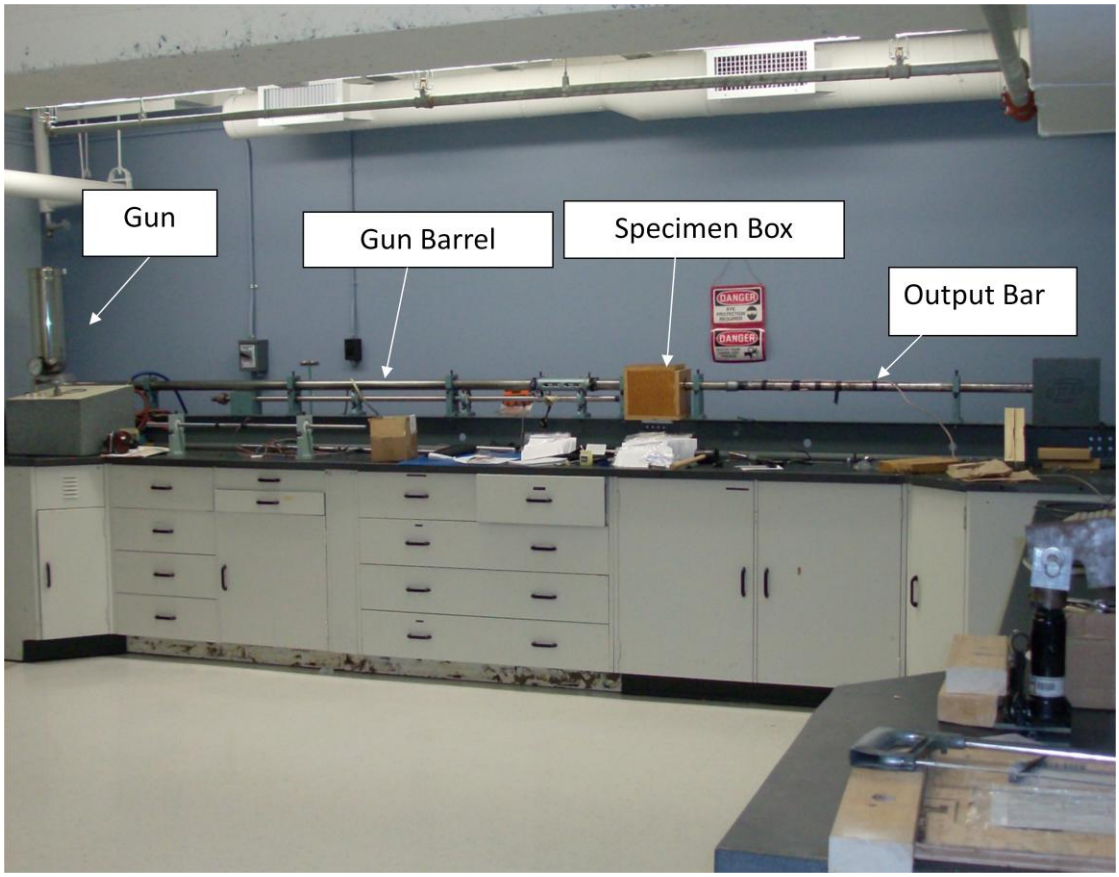

Figure 3.5. Photograph of direct impact Hopkinson bar used in this study.

The elastic waves are captured by the oscilloscope as time (s) vs. voltage (V) data. The voltage can be converted to the impacted load (N) by calibrating the strain gage on the out-put bar. In order to calibrate the gage, the output bar was subjected to quasi-static compressive loads of 1 kN to 7 kN in increments of 1 kN. The voltage corresponding to each applied load (N) was measured and a plot of load (N) vs. voltage (V) was made, as shown in Fig. 3.6. The slope of load (N) vs. voltage (V) relationship was found to be 21798 N/V, which gave the conversion factor for voltage measured by the oscilloscope into the corresponding force in N.

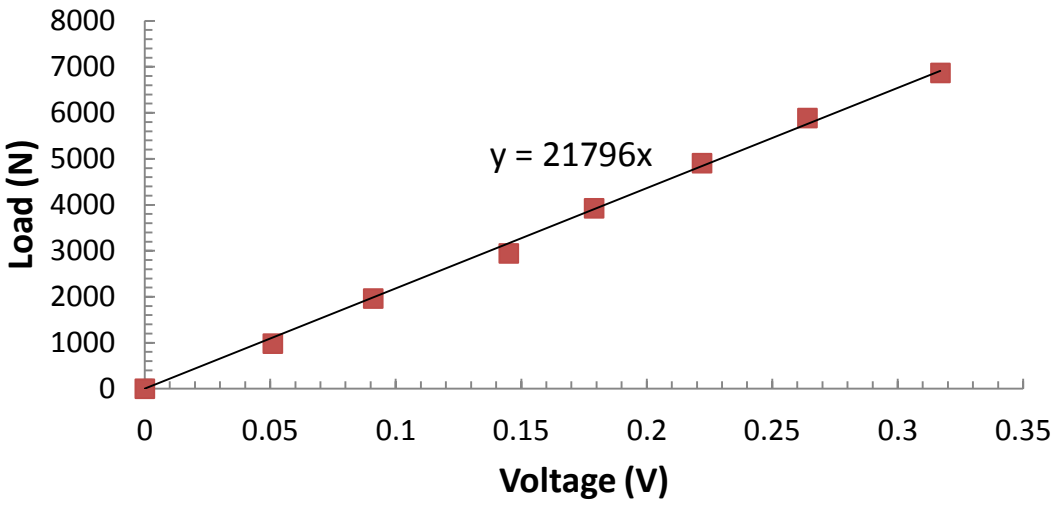

Figure 3.6. Direct impact test calibration result.

If it is assumed that specimens have constant volume and a linear variation of displacement with time, as well as constant strain rate, the true stress and true strain values can be calculated from the following equations:

$$\sigma(t) = \frac{P(t)}{A_i} \frac{L_i - (L_i - L_f)(t/t_f)}{L_i} \tag{3.1}$$

$$\varepsilon(t) = \ln \frac{L_i}{L_i - (L_i - L_f)(t/t_f)} \tag{3.2}$$

where, L_i and L_f are initial and final length, respectively. The data for the dynamic stress-strain curves for the materials under impact loading were computed using Equations 3.1 and 3.2. The strain rate corresponding to each impact velocity is directly proportional to the maximum strain and inversely proportional to the length of the striker bar (l), which was 0.223 m in this case, as shown in Equation 3.3. The strain-rate was calculated using this equation:

$$\dot{\varepsilon} = \frac{C_0}{2l} \varepsilon \tag{3.3}$$

where, C_0 is the longitudinal wave propagation velocity in the transmitter bar.

3.2.2.2. Torsion test

A torsional Kolsky Bar was used in conducting the high strain rate test in torsion on the test specimens. A schematic view of the Torsional Kolsky Bar is shown in Fig. 3.7, while a photograph of the bar used in this study which is located in Department of Mechanical and Manufacturing Engineering at University of Manitoba, is shown in Fig. 3.8. The system consists of two collinear bars. The incident one can rotate easily within the support of bearings. The short, thin-walled specimen is loaded between the two bars. The torsional wave, which is produced by a sudden release of a stored torque in the loading end of the incident bar, travels through the incident bar and is captured by the strain gage attached to the incident bar. On reaching the specimen, it loads and deforms the specimen rapidly. The incident wave is partially transmitted to the transmitter bar and partially reflected back to the incident bar. The transmitted wave is captured by the strain gage attached to the transmitter bar while the reflected wave is captured by the strain gage attached to the incident bar. The amplifier amplifies the detected strain data and sends them to an oscilloscope, which collects and stores the data. The stress, strain, and strain-rate can be calculated from the incident, transmitted and reflected wave data.

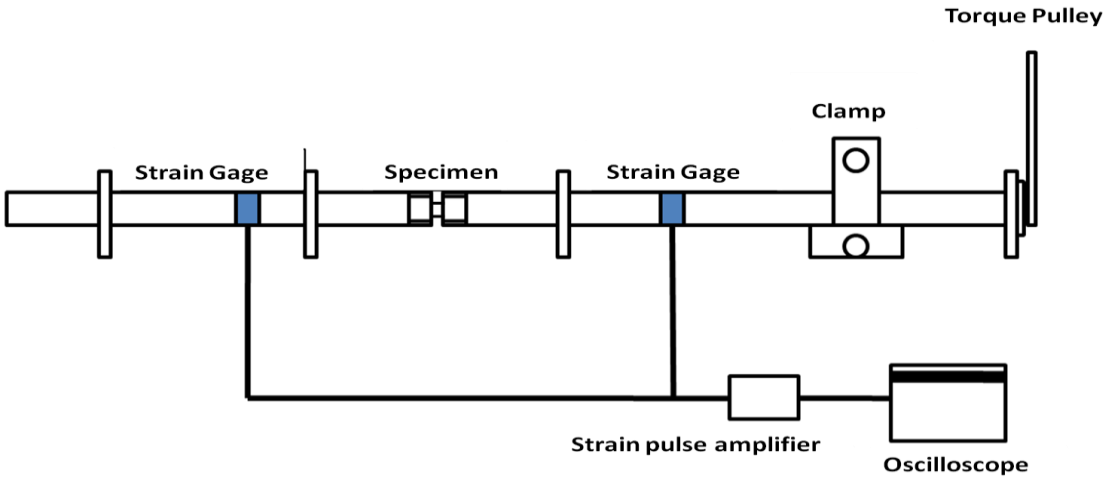

Figure 3.7. Schematic view of torsional Kolsky bar testing.

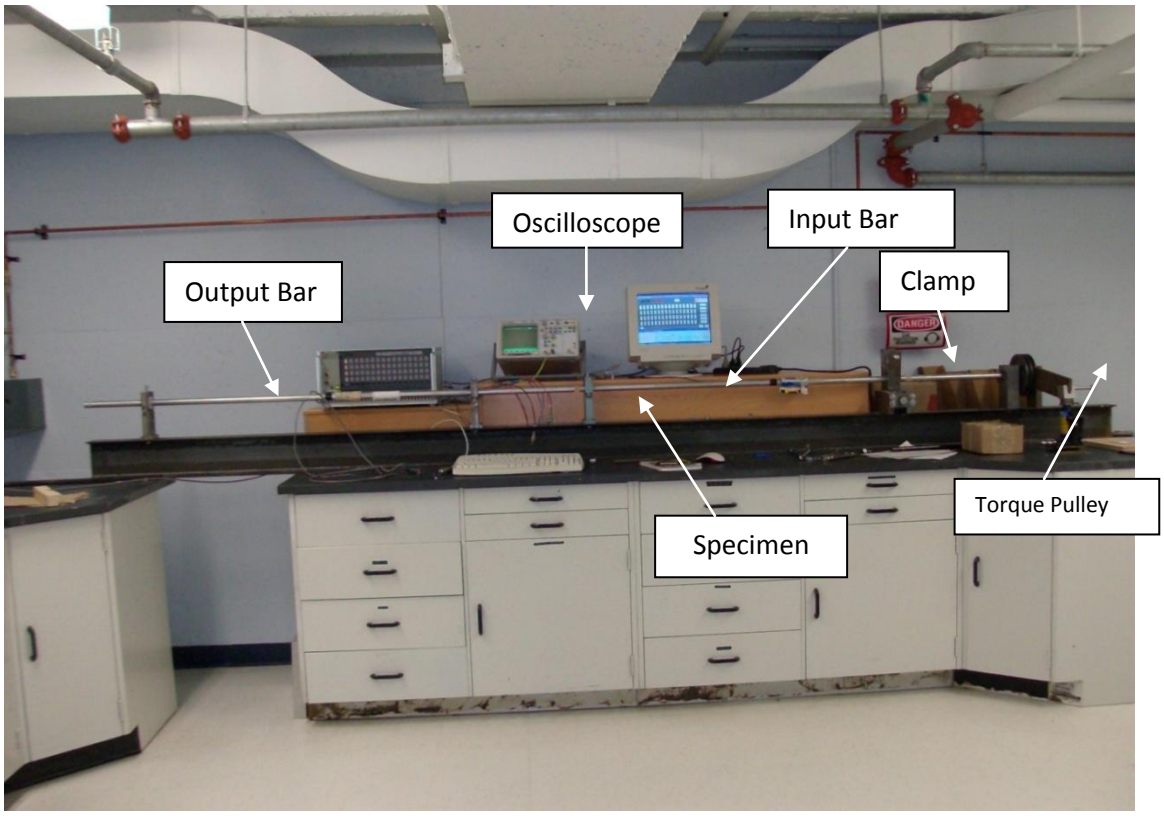

Figure 3.8. Photograph of torsional Kolsky bar used in this study.

The corresponding shear strain for the elastic wave data in the form of voltage recorded by the oscilloscope was determined by loading a connected incident and transmitter bar in torsion at incremental angles of twist while reading the voltage generated by the strain gages on the bars. A plot of shear strain against voltage is shown in Figs. 3.9 and 3.10, which gives the conversion factor for obtaining the shear strain that corresponds to voltage output from the strain gages on the incident and transmitter bars. By using the slopes of the lines in Figs. 3.9 and 3.10, the incident strain (γ_I), transmitted strains (γ_T) and reflected strains (γ_R) were computed from the voltage data from the strain gages. The shear strain vs. voltage relationships were calculated as follows:

Incident bar. $$\gamma_I = 1.323 \times 10^{-4} \frac{Strain}{Voltage\ (V)} \times \text{Voltage (V)} \quad (3.4)$$

$$\gamma_R = 1.323 \times 10^{-4} \frac{Strain}{Voltage\ (V)} \times \text{Voltage (V)} \quad (3.5)$$

Transmitted bar. $\gamma_T=1.314x10^{-4}\frac{Strain}{Voltage\ (V)}$x Voltage (V) (3.6)

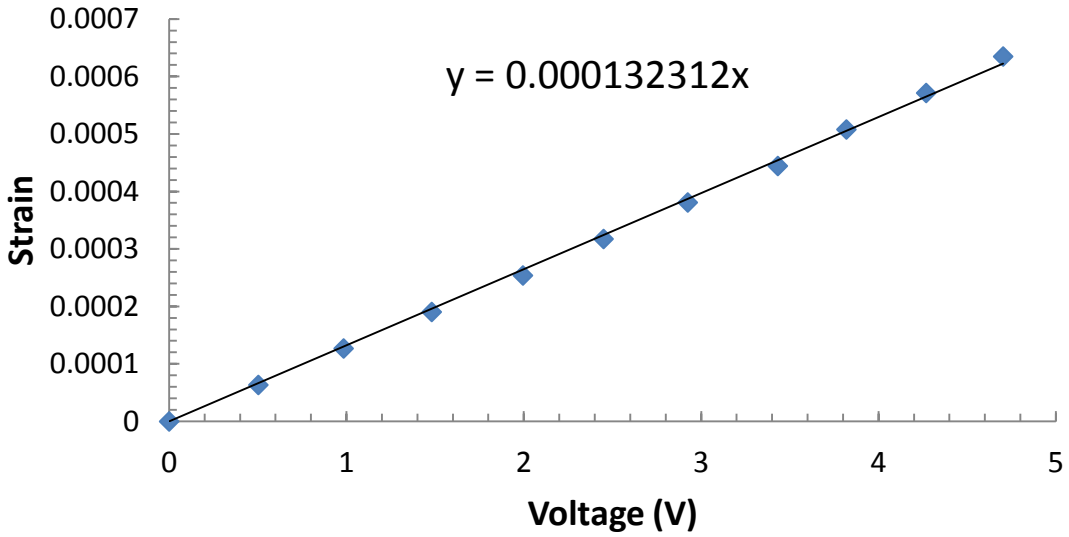

Figure 3.9. Torsional Kolsky bar calibration result for incident and reflected waves.

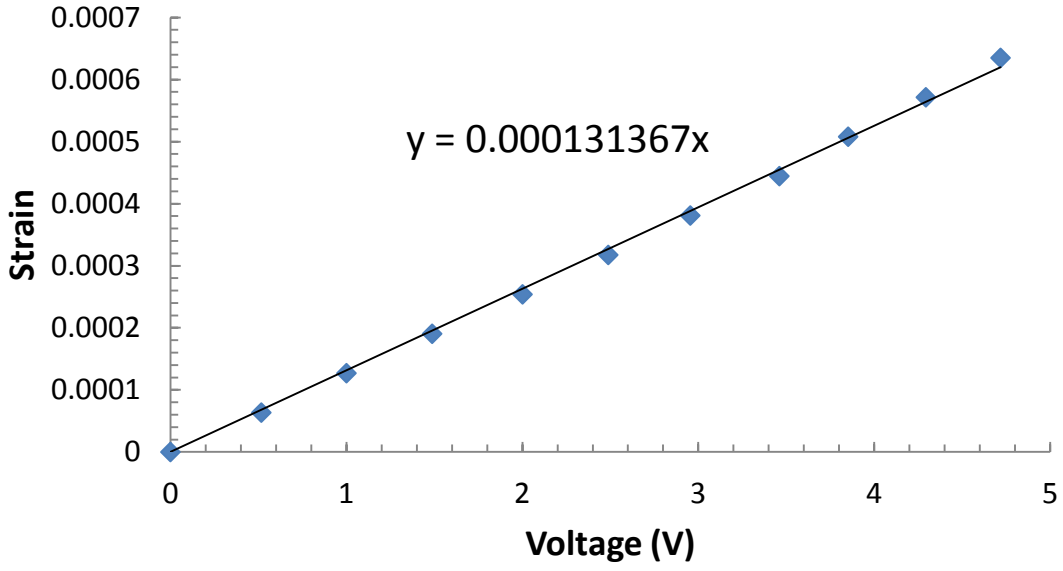

Figure 3.10. Torsional Kolsky bar calibration result for transmitted waves.

The strain-rates were calculated as follows [84]:

$$\dot{\gamma}_s(t) = \frac{r_s}{L_s}\frac{2c}{r_b}\left[-\gamma_R(t)\right] \tag{3.7}$$

where r_s is the mean radius of the thin-wall specimen, L_s is the length of the specimen, c is the wave speed propagation velocity in bar, and r_b is the radius of the bar. The shear strain in the specimen was calculated by integrating the strain rate, as shown in Equation 3.5 [84]:

$$\gamma_s(t) = \int_0^t \dot{\gamma}_s\,(t)dt \tag{3.8}$$

The shear stress was determined using Equation 3.6 as follows [84]:

$$\tau_s(t) = \frac{G{r_b}^3}{4{r_s}^2 t_s}\,\gamma_T(t + t_T) \tag{3.9}$$

where G is the shear modulus [84].

3.2.4. Microstructural Investigations

Deformed specimens that had been subjected to dynamic shock loadings were mounted in phenolic resin using the pneumatic mounting press shown in Fig. 3.11. The mounted specimens were pre-grinded with water on SiC-220 grit paper mounted on a rotating polishing wheel for 1 minute. Then, they were grinded on the MD-largo disc on a low speed polishing wheel with MD-Largo polishing liquid for 5 minutes. The grinded specimens were then polished in two polishing stages. In stage one, specimens were polished on a MD-Dac polishing cloth with MD-Dac liquid on a low speed polishing wheel for 4 minutes. In the final stage, they were polished on MD-Nap polishing cloth with MD-Nap liquid on low speed polishing wheel for 1 minute. The polished samples were then etched with 2% nital for about 16 seconds.

Figure 3.11. Photograph of pneumatic mounting press used for specimen mounting.

Prepared specimens were observed under optical microscope (Nikon ECLIPSE MA100) using four different magnifications: 50X, 100X, 500X, and 1000X located in Room ENG 2C25 in the Department of Mechanical Engineering at University of Saskatchewan. Specimens with well formed white shear bands were then cut along the longitudinal cross-section, polished and etched in 2% nital for 16 seconds. The specimens were then observed under the optical microscope to give the geometry of the shear bands along longitudinal cross-section of the impacted specimen. Figure 3.12 shows the Nikon Eclipse MA 100. Fractographic investigation of fragmented specimens was done using a Scanning Electron Microscope (SEM). Figure 3.13 shows the Joel JSM 6010L V Scanning Electron Microscope used in this research study which is located in Department of Mechanical Engineering at University of Saskatchewan. The SEM was operated using accelerated voltage of 15KV and a secondary electron imaging technique. X-ray photoemission electron microscope (XPEEM) with Near Edge X-Ray Absorption Fine Structure (NEXAFS) spectroscopy was used to investigate the chemical and electronics structure of material inside and outside of the adiabatic shear band for

AISI 4340 alloy steel using synchrotron light radiations at the Canadian Light Source (CLS) in Saskatoon.

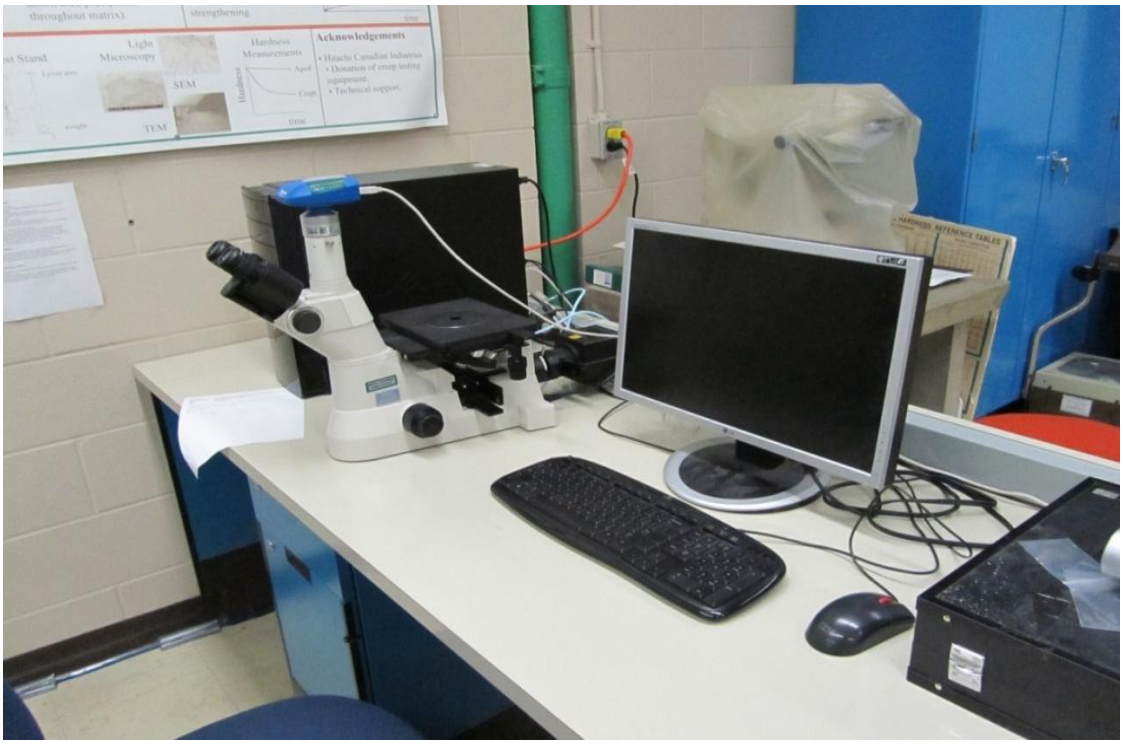

Figure 3.12. Photograph of the Nikon Eclipse MA 100 optical microscope used in this study.

Figure 3.13. Joel Scanning Electron Microscope (SEM).

3.2.5. Microhardness Measurements

Vickers microhardness tests were conducted on the material, inside and outside of the shear bands for specimens with well-formed adiabatic shear bands. Figure 3.14 shows the Vickers microhardness tester used in this research which is located in Mechanical Engineering Department at University of Saskatchewan (Room ENG 2C25).

Figure 3.14. Vickers microhardness tester.

Polished specimens were mounted on the Microhardness tester and indented using a diamond indenter. The Vickers hardness number is obtained by the ratio of *F/A*, where *F* is the force applied to the square-based pyramid diamond indenter, which was 500gf for this work. *A* is the surface area of the resulting indentation in square micrometers, which can be calculated by the following equation:

$$A = \frac{d^2}{2\sin(136°/2)} \approx \frac{d^2}{1.8554} \tag{3.10}$$

where, *d* is the average length of the indentation diagonal D_1 and D_2. The Vickers hardness number was calculated using the following equation [59]:

$$VHN = \frac{F}{A} \approx \frac{1.8554\,F}{d^2} \tag{3.11}$$

Figure 3.15 shows optical micrographs of Vickers microhardness test indentations located inside and outside of the shear band of a quench-hardened AISI 1340 steel specimen tempered at 425˚C, and impacted at 39.1 kg.m/s.

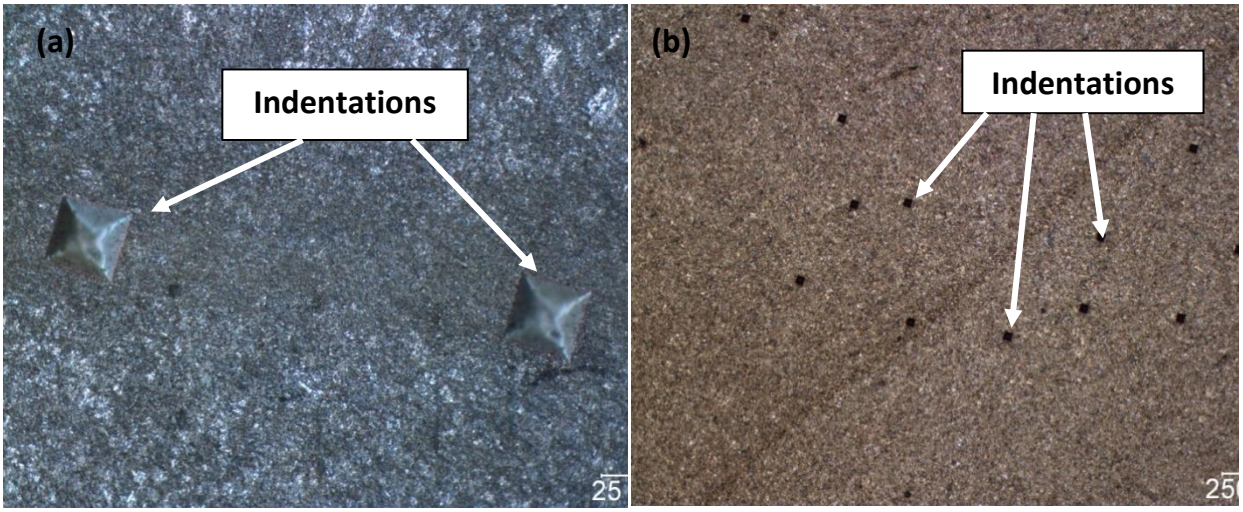

Figure 3.15. Optical micrographs showing Vickers hardness indentations on quench-hardened AISI 1340, tempered at 425˚C, impacted at 39.1 kg.m/s, (a) inside the shear band, (b) outside the shear band.

CHAPTER FOUR

RESULTS AND DISSCUSSION

Stress-strain curve results from the dynamic impact and torsional tests are outlined in this chapter. The effects of strain rate and microstructure on the dynamic stress-strain curves are discussed. Results of metallographic and microhardness tests of heat-treated specimens before and after impact are presented in this chapter. The effects of strain rate, microstructure, alloying elements, and geometry of the specimen on adiabatic shear band behaviour of AISI 1340 and 4340 steel are discussed.

4.1. Stress-strain curve

4.1.1. Overview

Figure 4.1 shows a typical stress-strain curve obtained from high strain-rate loading of a cylindrical steel specimen. After a clear yield point, which shows the onset of plastic deformation, strain hardening as a result of plastic deformation and thermal softening due to the heat generated inside the material, occur simultaneously [3]. At the beginning, strain hardening dominates the plastic deformation until a maximum flow stress is reached. After the maximum flow stress, thermal softening dominates the deformation process. Hence, as the strain increases, the flow stress decreases. The sharp stress collapse due to mechanical instability is a consequence of intense adiabatic heating along a narrow path leading to strain localization. This point is the critical strain for the occurrence of an adiabatic shear band (ε_{crit}) [3]. It should be noted that assumptions which has been made to produce dynamic stress-strain curves may not be valid after the onset of strain localization.

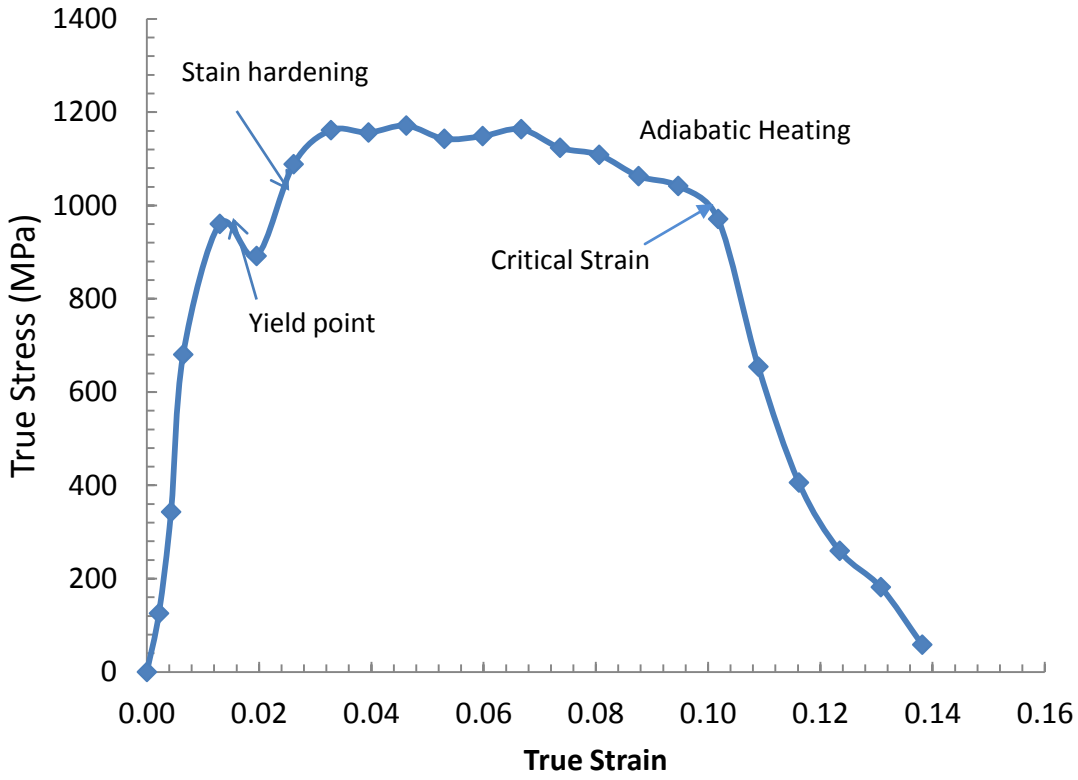

Figure 4.1. Typical stress-strain curve for specimen subjected to dynamic shock loading [martensitic AISI 1340 steel, tempered at 425˚C, cylindrical specimen and subjected to impact loading at 33.2 kg.m/s ($\dot{\varepsilon}$=1146 s^{-1})].

4.1.2. The effect of impact momentum

The effects of impact momentum on the dynamic impact response of the martensitic AISI 1340 steel specimens that were tempered at 315˚C are shown in Figs. 4.2 and 4.3. The strain-rate generated in each specimen is directly correlated to the applied impact momentum. As the impact momentum increases, the critical strain and time at which thermo-mechanical instability occur increases. The increase in critical strain for instability is due to increasing thermal softening and plastic strain in the specimens as impact momentum increases. Also, as the impact momentum increases, the specimens become more work-hardened before thermal softening begins to dominate the deformation process. The increased plasticity with increase in strain-rates is due to an increased thermal softening effect during the deformation process. This result agrees with the submission of Kalthoff and Burgel [75] that the temperature inside shear bands

increased as the loading rate increased, leading to significant effects of material yielding and plasticity. The same behaviour has been observed for the other microstructures which were impacted at different impact momentums (Figs. 4.2 - 4.6). Lee and Lin [71] suggested that as the strain-rate increases, the stress increases at any specific strain. Also, as the strain rate increases, the rate of work hardening decreases due to increased heat generation during plastic deformation. Increasing the strain rate has dual effects on plastic deformation. On one hand it increases strain hardening because of the dislocation multiplication. On the other hand, it increases thermal softening due to the heat generation during plastic deformation.

It has also been observed that as the impact momentum or strain-rate increases, maximum flow stress increases. However, for AISI 1340 steels specimens with martensitic structure, as the impact momentum increases, the maximum flow stress initially increases, but begins to decrease with increasing impact momentum at high values of impact momentum. From Table 4.1, this impact momentum beyond which maximum flow stress begins to decrease with increasing impact momentum is that momentum above which transformed bands are formed, as shown in the experimental data presented in Table 4.1. The temperature inside the shear band increases as the strain rate increases. The impact momentums at which maximum flow stresses begin to decrease increases with increasing tempering temperature. This indicates that martensitic specimens that were tempered at a lower tempering temperature are more inclined to form transformed bands at lower strain-rates. On the other hand, for steel specimens with pearlitic structure, as the strain-rate increases, the maximum flow stress increases and there is no evidence of decrease in maximum flow stress, within the range of applied impact momentum (strain-rate). It can also been seen from Table 4.1 that no transformed adiabatic shear band was observed in the specimen at highest applied impact momentum.

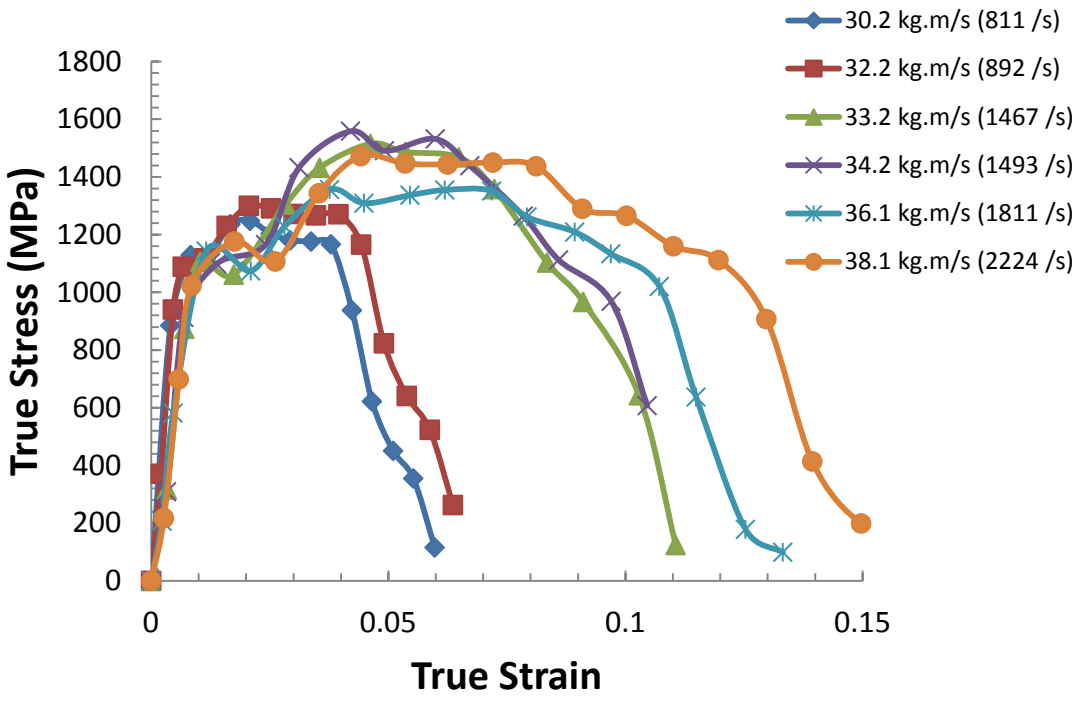

Figure 4.2. Dynamic impact stress-strain curves for martensitic AISI 1340 steel specimens (tempered at 315˚C) as a function of the impact momentum and strain rates.

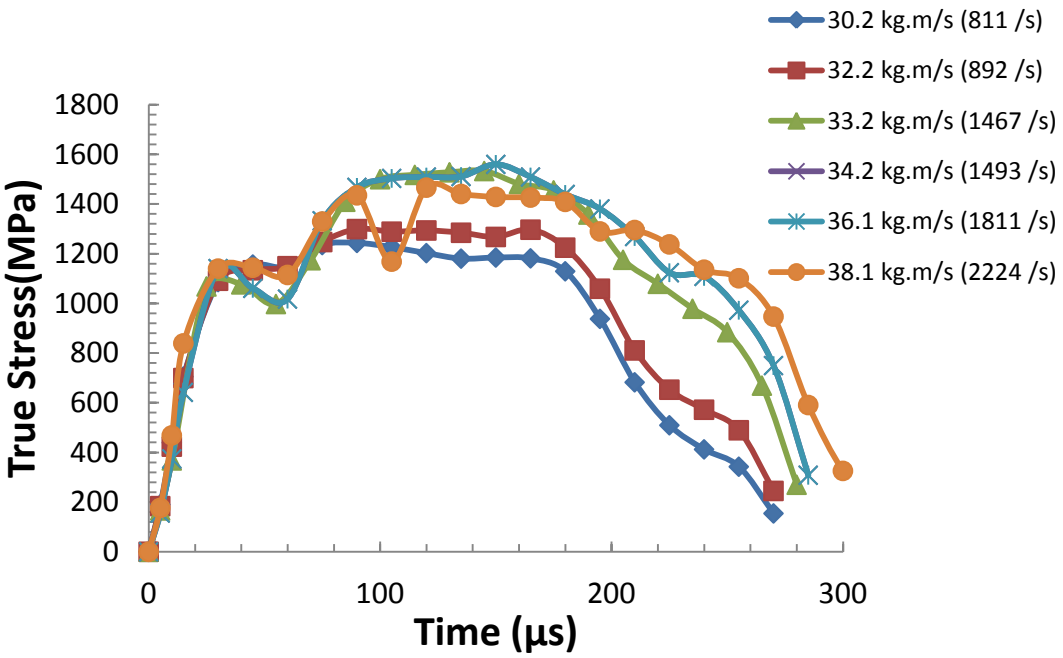

Figure 4.3. Stress vs. deformation time curves for martensitic AISI 1340 steel specimens (tempered at 315˚C) as a function of the impact momentum and strain rates.

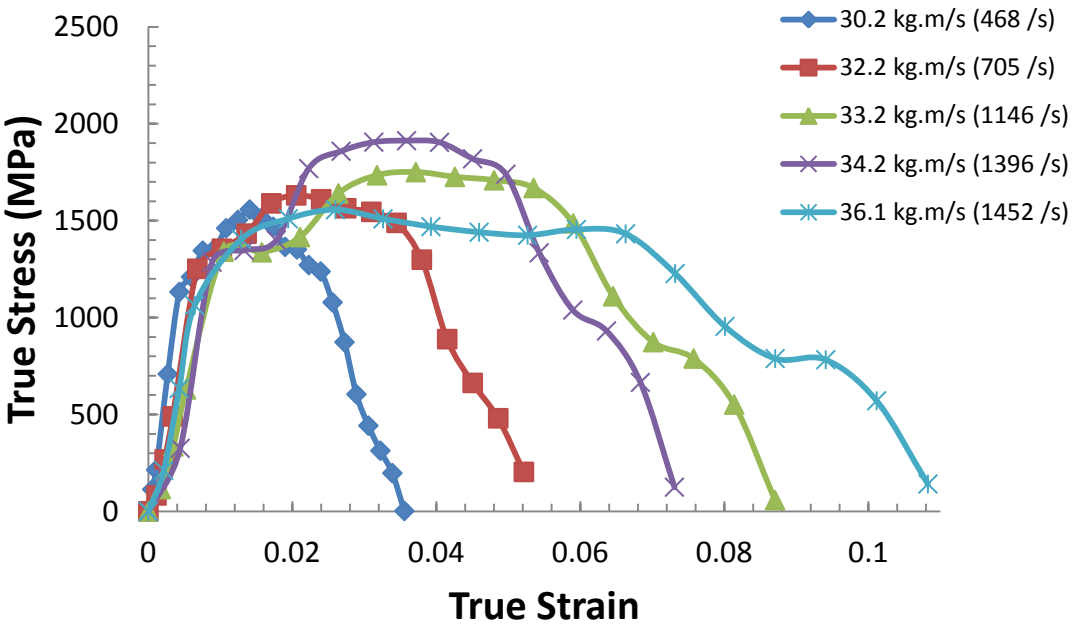

Figure 4.4. Dynamic impact stress-strain curves for martensitic AISI 1340 steel specimens (tempered at 205˚C) as a function of the impact momentum and strain rates.

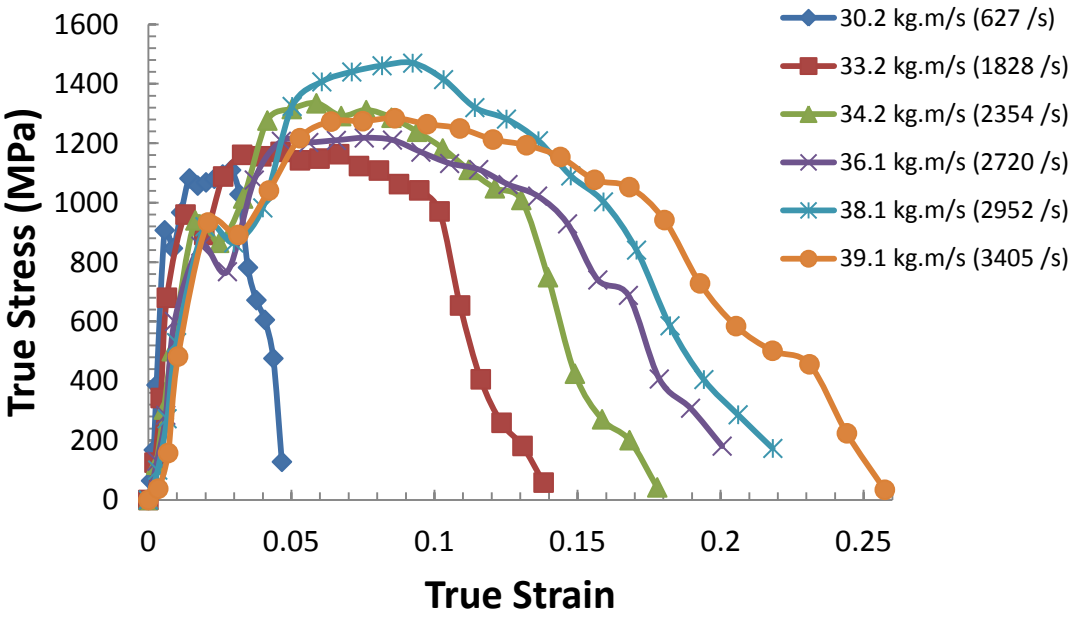

Figure 4.5. Dynamic impact stress-strain curves for martensitic AISI 1340 steel specimens (tempered at 425˚C) as a function of the impact momentum and strain rates.

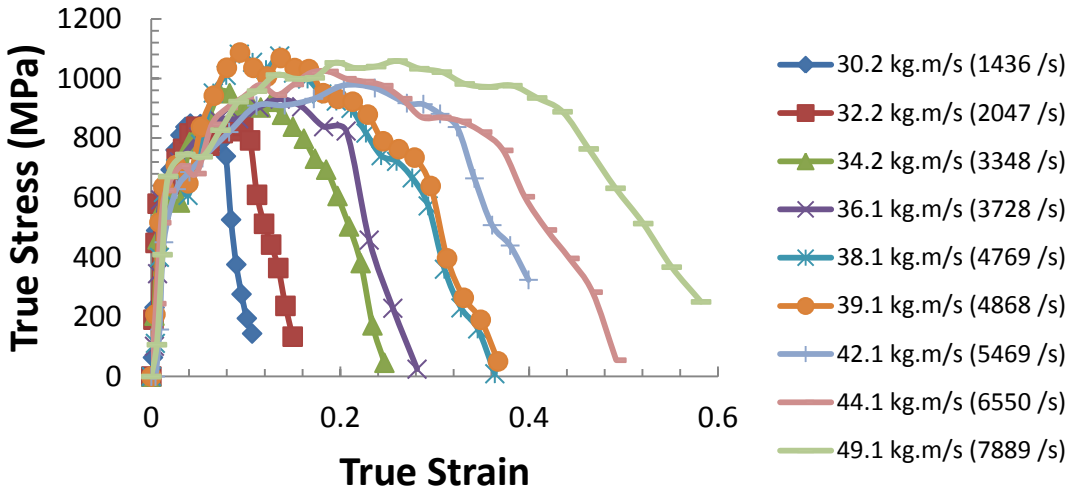

Figure 4.6. Dynamic impact stress-strain curves for pearlitic AISI 1340 steel specimens as a function of the impact momentum and strain rates.

Table 4.1. Experimental data sheet for the impact test

a. AISI 1340 steel

Impact pressure (kPa)	Impact Momentum (kg.m/s)	Total Strain	Strain rate (s^{-1})	ASB
Martensitic Structure (Temper at 205˚C)				
60	30.2	0.035	468	Slightly Deformed
80	32.2	0.052	705	Deformed
100	34.2	0.071	965	Slightly Transformed
100	34.2	0.102	1396	Slightly Transformed
120	36.1	0.105	1452	Transformed
140	38.1	Fractured	Fractured	Transformed
150	39.1	Fractured	Fractured	Transformed
Martensitic Structure (Temper at 315˚C)				
60	30.2	0.060	811	Deformed
80	32.2	0.066	892	Deformed
90	33.2	0.106	1467	Deformed
100	34.2	0.108	1493	Intense Deformed
120	36.1	0.129	1811	Deformed and Transformed
140	38.1	0.156	2224	Transformed
150	39.1	0.176	2534	Transformed
180	42.1	Fractured	Fractured	Transformed
Martensitic Structure (Temper at 425˚C)				
60	30.2	0.047	627	None
80	32.2	0.146	2064	None
100	34.2	0.193	2354	Deformed
120	36.1	0.188	2720	Deformed
140	38.1	0.202	2952	Deformed
150	39.1	0.229	3405	Deformed and Transformed
180	42.1	Fractured	Fractured	Transformed
Pearlitic Microstructure				
60	30.2	0.010	1376	None
60	30.2	0.104	1436	None
80	32.2	0.145	2047	None
100	34.2	0.225	3348	Slightly Deformed
120	36.1	0.247	3728	Deformed
140	38.1	0.305	4769	Deformed
150	39.1	0.310	4868	Deformed
180	42.1	0.341	5469	Deformed
200	44.1	0.393	6550	Deformed
250	49.1	0.452	7889	Deformed

Impact pressure (kPa)	Impact Momentum (kg.m/s)	Total Strain	Strain rate (s^{-1})	ASB
Dual-Phase Microstructure				
60	30.2	0.057	776	None
80	32.2	0.099	1371	Deformed
100	34.2	0.116	1622	Intense Deformed
120	36.1	0.136	1910	Deformed
140	38.1	0.168	2409	Deformed
160	40.1	0.187	2722	Deformed and Transformed
180	42.1	Fractured	Fractured	Transformed
200	44.1	Fractured	Fractured	Transformed

b. AISI 4340 steel

Martensitic Structure (Temper at 315˚C)				
100	34.2	0.120	1677	Intense Deformed
120	36.1	0.138	1943	Intense Deformed
140	38.1	Fractured	Fractured	Transformed
Pearlitic Microstructure				
120	36.1	0.110	1528	None
140	38.1	0.144	1999	None
150	39.1	0.140	1872	Slightly Transformed
180	42.1	Fractured	Fractured	Transformed
Dual-Phase Microstructure				
80	32.2	0.089	1228	Slightly Deformed
80	32.2	0.091	1819	Slightly Deformed
100	34.2	0.095	1310	Deformed
100	34.2	0.094	1293	Deformed
120	36.1	0.118	1646	Intense Deformed
120	36.1	0.136	1916	Intense Deformed
140	38.1	Fractured	Fractured	Transformed
160	40.1	Fractured	Fractured	Transformed

4.1.3. The effect of microstructure

Figure 4.7 shows the effect of microstructure on stress-strain curves for AISI 1340 steel specimens that were impacted at the same impact momentum of 36.1 kg.m/s. The corresponding strain-rates generated in each specimen are also indicated in this figure. The total strains as well as critical strains for the onset of thermo-mechanical instability are higher for the martensitic AISI 1340 steel specimens that were tempered at 425˚C compared to those that were tempered at 315˚C and 205˚C. Meanwhile, the AISI 1340 steel specimens with pearlitic structure have the highest total strain and critical strain for thermo-mechanical instability. The steel with dual-phase structure has intermediate properties between those with martensitic and pearlitic microstructures. As the tempering temperature increases for martensitic steel specimens, the initial resistance to plastic deformation under the impact loading decreases. The strain and the time at, which thermal softening begins to dominate the deformation process increases, as shown in Figs. 4.7 and 4.8. The critical strain and time for the onset of adiabatic heating and the associated thermo-mechanical instability, which triggers shear strain localization, also increases with increasing tempering temperature. This suggests that the susceptibility of the martensitic specimens to the adiabatic shear banding will decrease with increasing tempering temperature.

The amount of strain the specimens can withstand after yielding and before thermal softening dominate the strain hardening tends to increase with increasing tempering temperature. This suggests that increasing tempering temperature will result in lower tendency for the occurrence of adiabatic shear band in quenched and tempered AISI 1340 steel specimens. Hwang *et al*. [58] investigated the effect of tempering on stress-strain curves for low-carbon steel plate that was subjected to torsional loading at high strain rate using Torsional Kolsky Bar. They also observed that as the annealing time increased, fracture shear strain increased, while the maximum shear stress beyond which thermal softening plays a major role decreased. As the annealing time increased the width of the shear band increased.

Tempering temperature and time both have the same effect on the steel microstructure. By increasing either time or temperature, the internal stresses inside the material are

relieved and the material become relaxed. Zhang *et al.* [8] suggested that tempering temperature of impacted low alloy steel (40Cr and 40CrNiMo) specimens had a great effect on the formation of adiabatic shear bands. They observed that at low to medium tempering temperatures, transformed adiabatic shear bands were formed, while at higher tempering temperatures, deformed adiabatic shear band were formed.

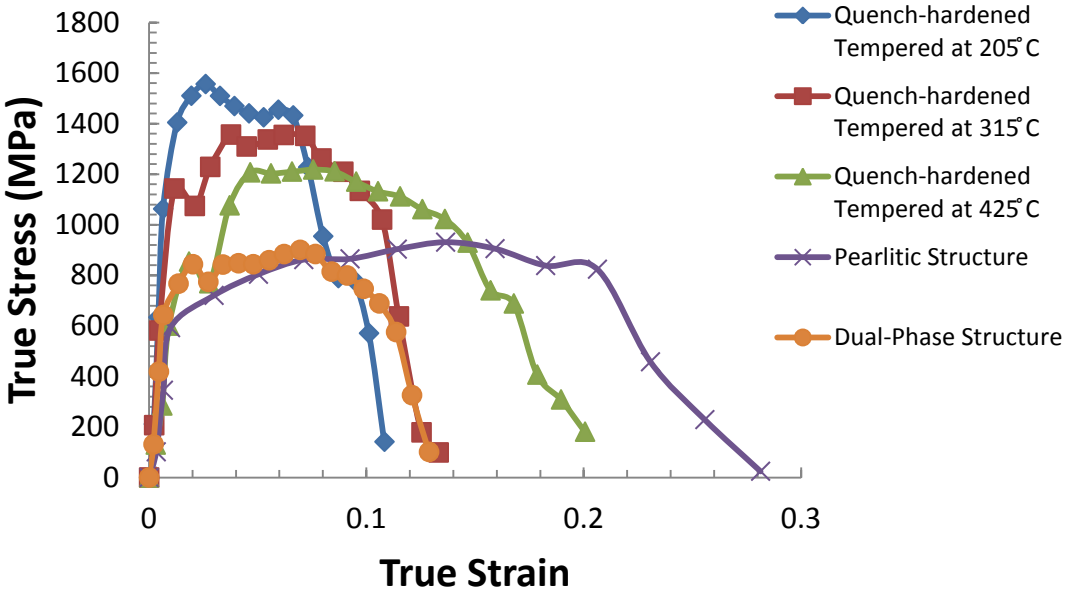

Figure 4.7. Dynamic impact stress-strain curves for AISI 1340 steel as a function of the heat-treatment condition (impacted at 36.1 kg.m/s).

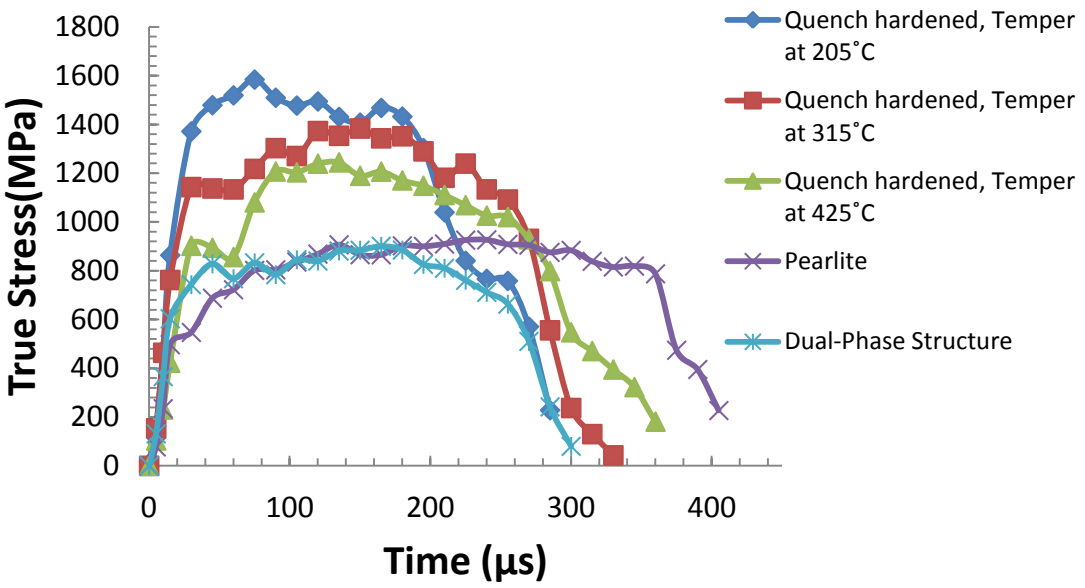

Figure 4.8. Stress vs. deformation time curves for martensitic AISI 1340 steel specimens (tempered at 315˚C), as a function of heat-treatment condition.

Since the AISI 1340 steel specimen with pearlitic structure has the highest ductility, it experiences the greatest work hardening before thermal softening and has the highest critical and total strain. The AISI 1340 steel specimens with dual-phase structure have intermediate properties between the specimens with martensitic and pearlitic structure. The dual-phase structure contains a soft ductile ferrite matrix that is reinforced with hard and strong martensite. Therefore, it demonstrates a good mixture of ductility and strength. Hence, the amount of strain hardening of specimens with dual-phase structure before thermal softening and critical strain at which they show thermo-mechanical instability and strain localization are significantly lower than for the steel specimens with pearlitic structure. On the other hand, it reaches the point at which thermal softening is the dominant deformation mechanism at a much lower stress level than that for the martensitic structure. The same behaviour has been observed for the other martensitic, pearlitic and dual-phase structure specimens impacted at different momentums [Figs. 4.9- 4.13] or subjected to dynamic torsional loading [Fig. 4.14]. Figure 4.14 shows the effect of microstructure on stress-strain curves for AISI 1340 steel torsional specimens that were subjected to dynamic torsional loadings using an

applied torque of 1619 N.m. The maximum flow stress above which thermal softening becomes dominant is highest in specimens with martensitic structure and lowest in that with pearlitic structure. The results are in line with those obtained from the impact test.

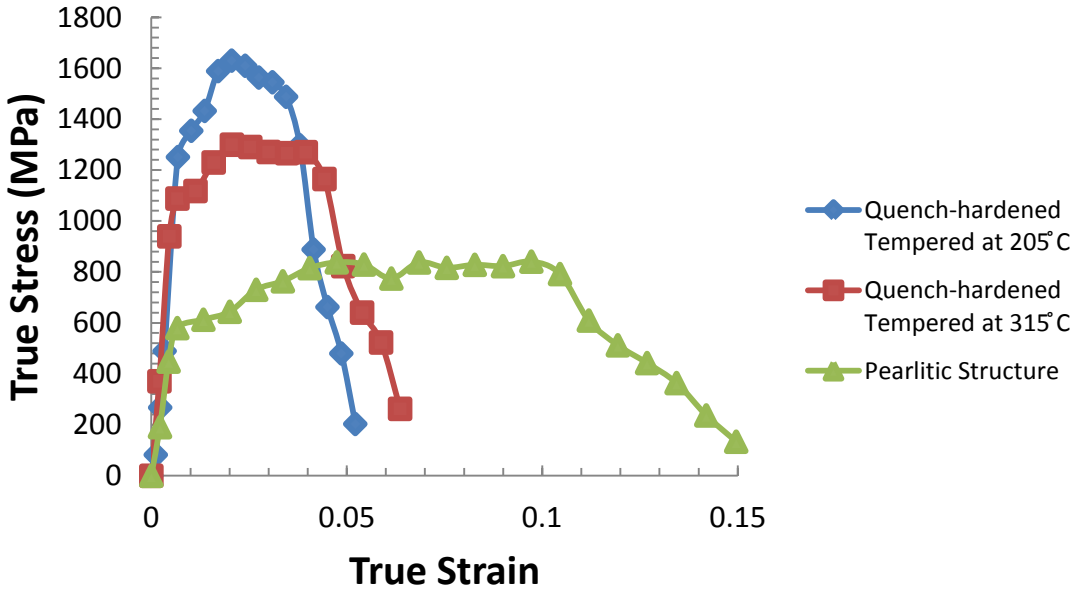

Figure 4.9. Dynamic impact stress-strain curves for AISI 1340 steel as a function of the heat-treatment condition (impacted at 32.2 kg.m/s).

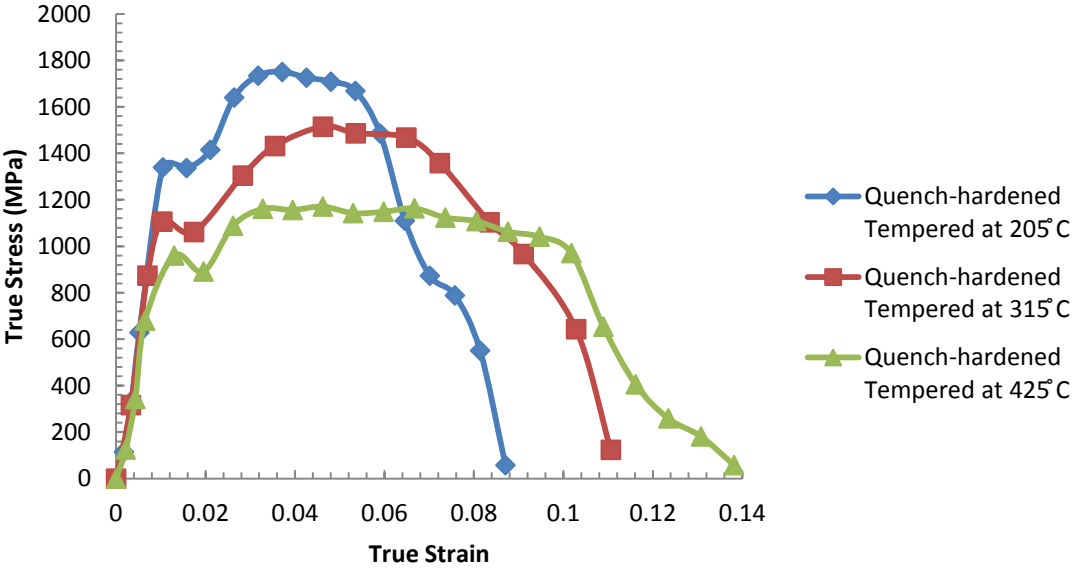

Figure 4.10. Dynamic impact stress-strain curves for AISI 1340 steel as a function of the heat-treatment condition (impacted at 33.2 kg.m/s).

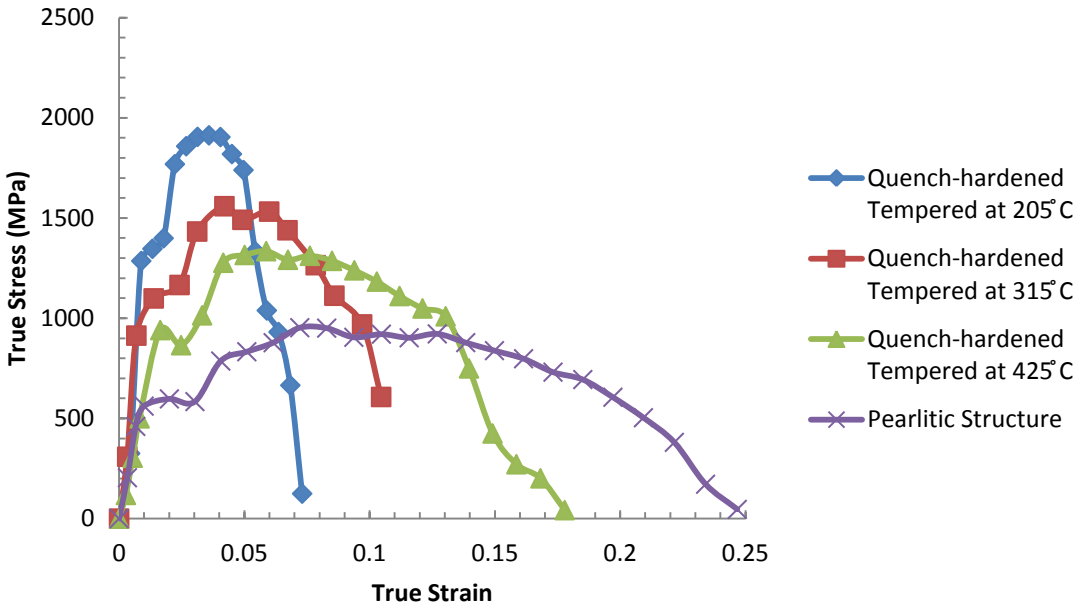

Figure 4.11. Dynamic impact stress-strain curves for AISI 1340 steel as a function of the heat-treatment condition (impacted at 34.2 kg.m/s).

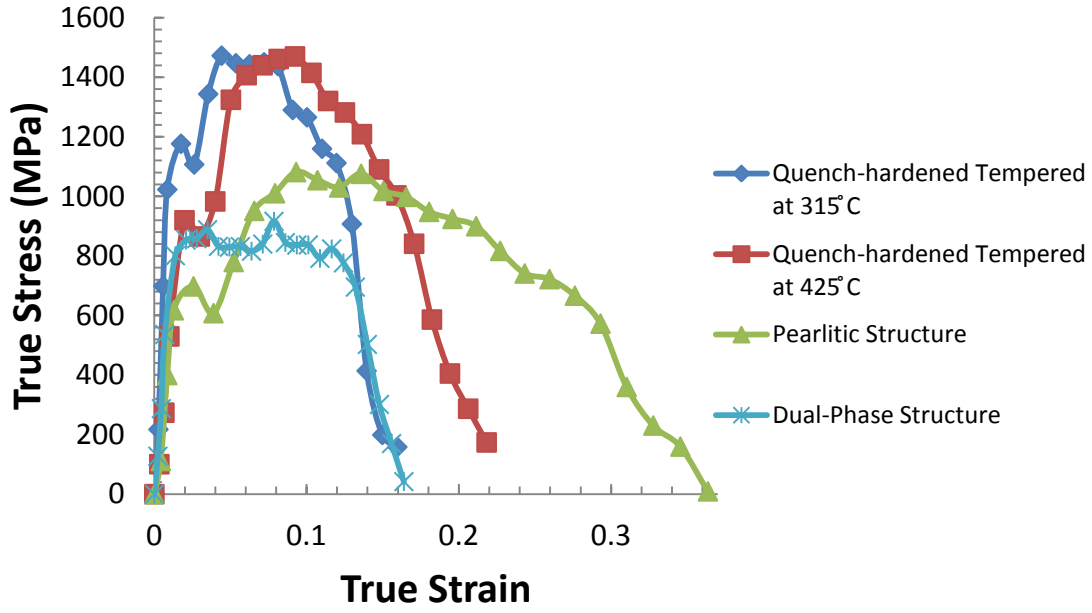

Figure 4.12. Dynamic impact stress-strain curves for AISI 1340 steel as a function of the heat-treatment condition (impacted at 38.1 kg.m/s).

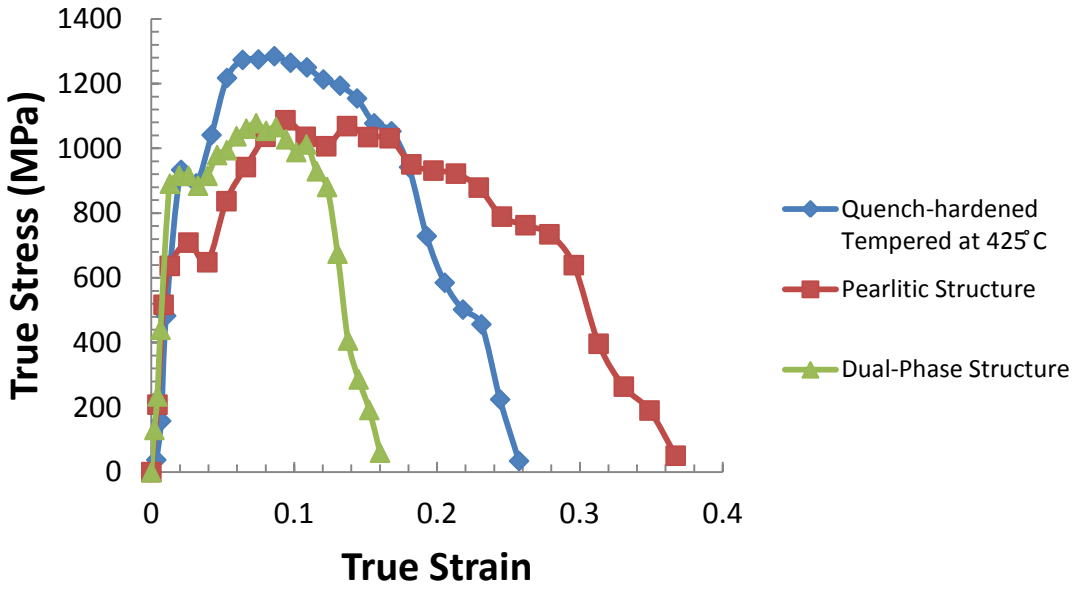

Figure 4.13. Dynamic impact stress-strain curves for AISI 1340 steel as a function of the heat-treatment condition (impacted at 39.1 kg.m/s).

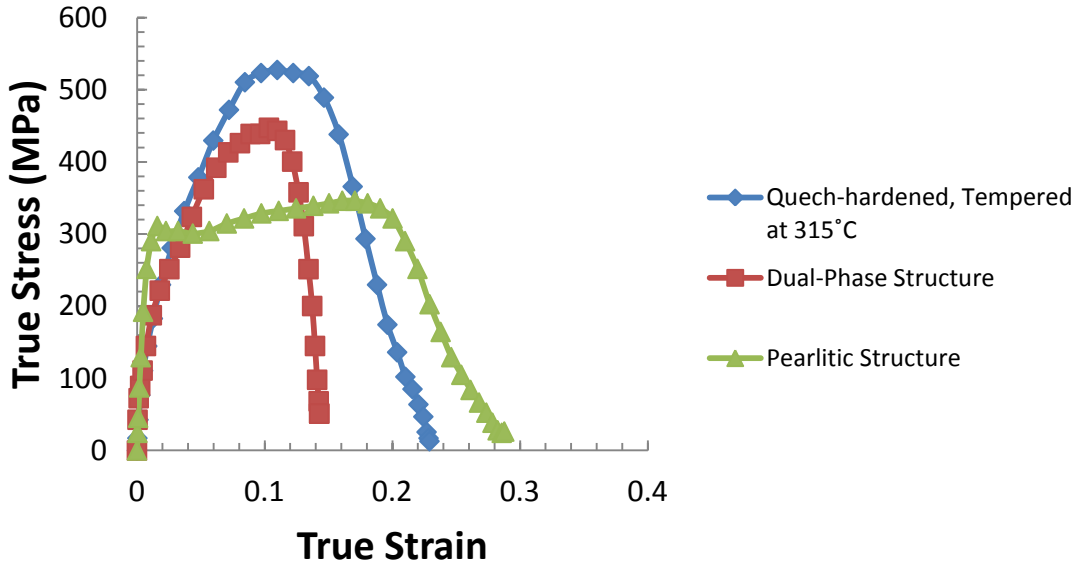

Figure 4.14. Torsional stress-strain curves for AISI 1340 steel as a function of the heat-treatment condition (1619 N.m torque).

4.1.4. The effect of alloying elements

Figures 4.15 and 4.16 show the effects of alloying elements on the stress-strain curves for quench-hardened AISI 1340 and AISI 4340 steel specimens subjected to impact momentums of 34.2 and 36.1 kg.m/s, respectively. At the higher impact momentum, both martensitic AISI 1340 and AISI 4340 alloy steel specimens show the same general behaviour (Fig. 4.16) although AISI 4340 steel had a higher strength under quasi-static loading. For the lower impact momentum of 34.2 kg.m/s, it is observed that martensitic AISI 1340 steel specimens undergo more strain hardening, before thermal softening dominates, than martensitic AISI 4340 steel specimens. Thus, AISI 1340 steel specimens have higher flow stress than AISI 4340 steel at this impact momentum (Fig. 4.15). This suggests that thermal softening has a more significant role in the impact response of martensitic AISI 4340 steel than martensitic AISI 1340 steel. Therefore, martensitic AISI 4340 steel specimens will be more inclined to form adiabatic shear bands than martensitic AISI 1340 steel specimens.

Figs. 4.17 and 4.18 show the effects of alloying elements on stress-strain curves for pearlitic AISI 1340 and AISI 4340 steel specimens. The AISI 4340 steel specimen has significantly higher yield strength than the AISI 1340 steel specimen impacted at the same momentum. This shows that pearlitic AISI 4340 steel specimens are more resistant to plastic deformation at high strain-rate deformation than AISI 1340 steel specimens. Moreover, pearlitic AISI 1340 steel specimens are significantly more hardened before thermal softening than AISI 4340 alloy steel. In addition, the maximum stress above which thermal softening is dominant is much higher for the AISI 4340 alloy steel than for the AISI 1340 alloy steel. These observations shows that, although the stress-strain curves of both alloys in the martensitic heat treatment condition are very close, a significant difference is noticed in their high strain-rate response when heat treated to form pearlitic structure.

Both AISI 1340 and AISI 4340 steel contain 0.4% C. However, AISI 4340 has considerable amounts of alloying addition such as Mn, Cr, Ni and Mo, while AISI 1340 is manganese steel containing 0.14 wt% V. Mn, Cr, Ni and Mo in steels increase the steel hardenability. Moreover, addition of vanadium, in the case of austenitizing at high

temperatures for a long time, provides secondary hardening during tempering [82]. Menzemera *et al*. [85] suggested that chromium, molybdenum, and manganese assist the formation of carbides which consequently increase matrix strength. Meanwhile Molybdenum helps refining the grain size. Moreover, Feng and Bassim [24] suggested that local materials defects cause adiabatic shear band initiations which are called initial perturbations. Bassim [34] suggested that any inhomogeneities inside the material increases the materials' susceptibility to form adiabatic shear bands. Consequently, AISI 4340 alloy steel with higher amount of overall Cr, Mo, Ni and Mn is more likely to form carbides which can act as initial perturbations and promote adiabatic shear band formation. These carbides also increase the internal stresses inside the material which causes higher temperature rise within adiabatic shear bands during high strain-rate deformation. Therefore, AISI 4340 steel specimens are more inclined to experience more intensive adiabatic heating and form adiabatic shear bands than AISI 1340 steel specimens.

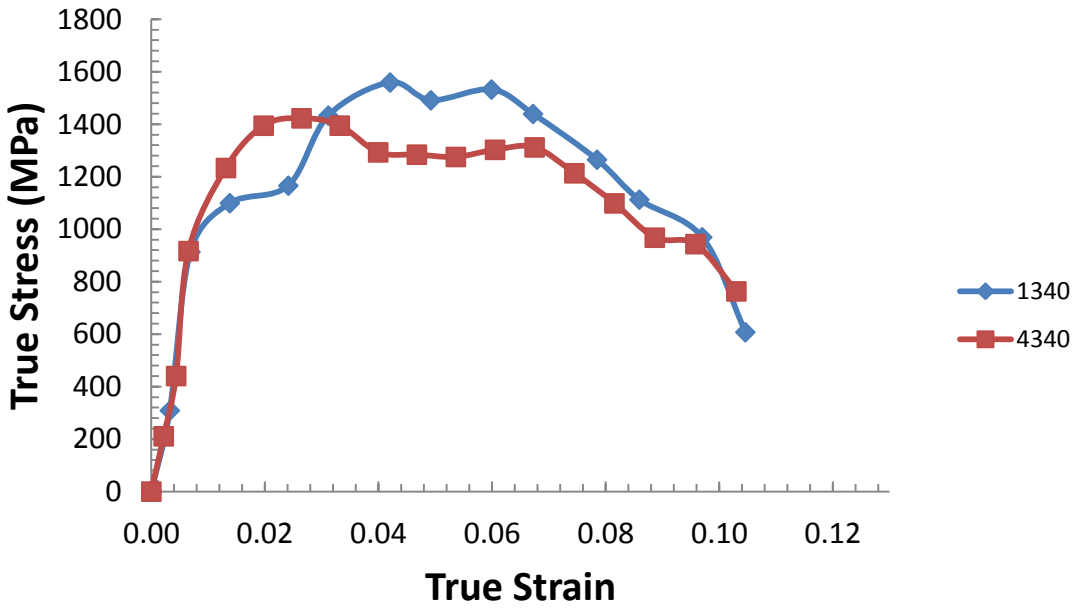

Figure 4.15. Stress-strain curves for martensitic steels, tempered at 315˚C, cylindrical specimens, impacted at 34.2 kg.m/s.

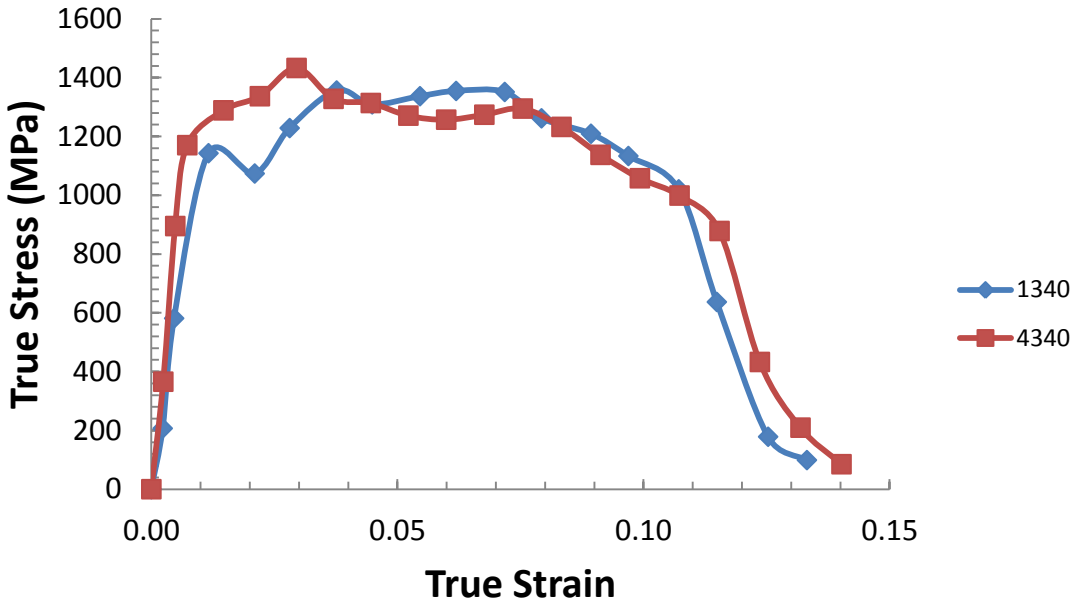

Figure 4.16. Stress-strain curves for martensitic steels, tempered at 315˚C, cylindrical specimens, impacted at 36.1 kg.m/s.

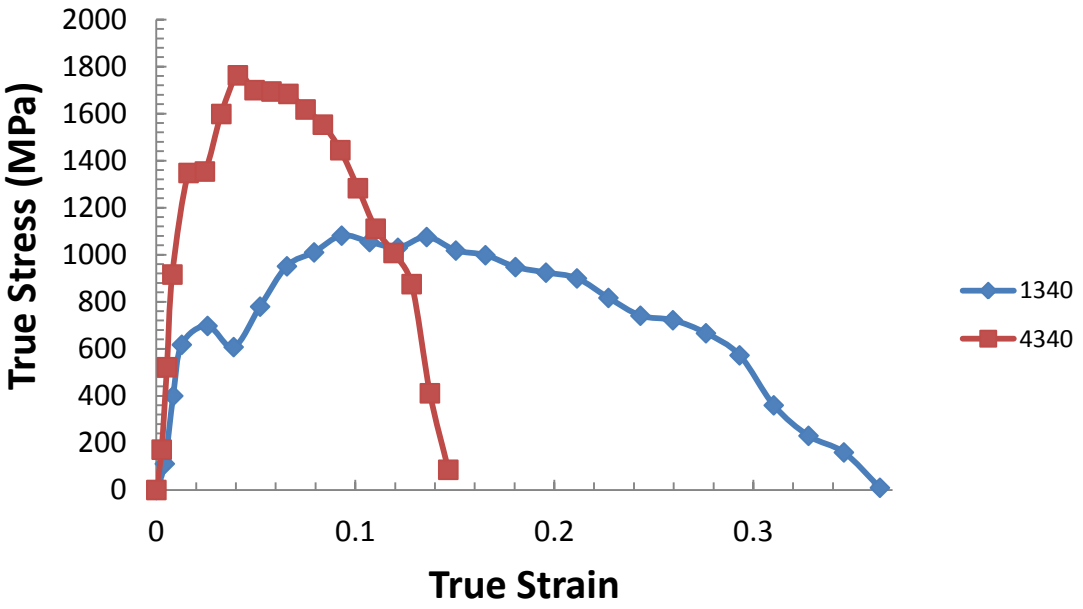

Figure 4.17. Stress-strain curves for steel pearlitic structure steels, cylindrical specimen, impacted at 38.1 kg.m/s.

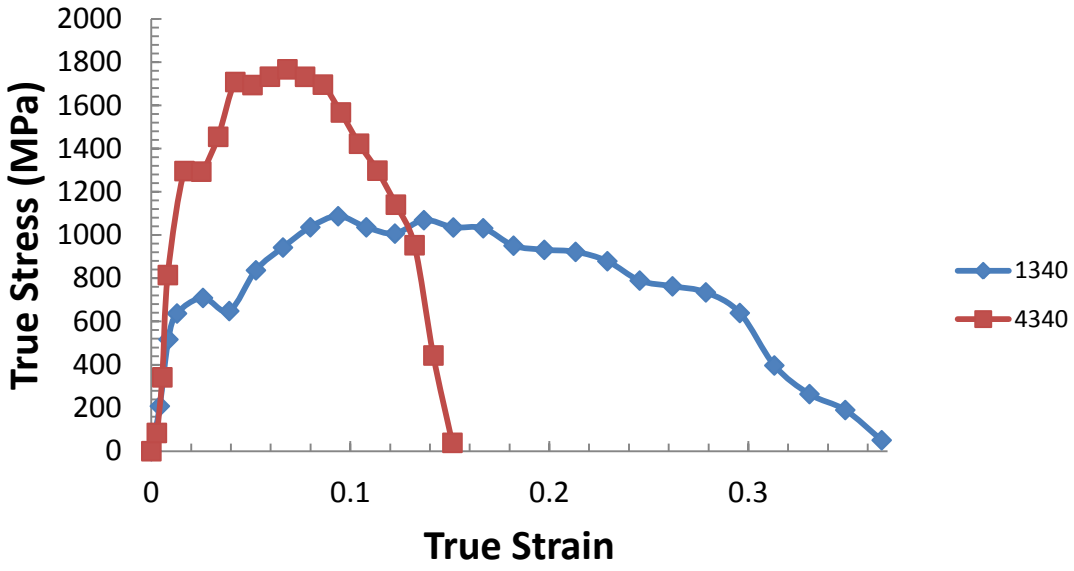

Figure 4.18. Stress-strain curves for pearlitic structure steels, cylindrical specimen, impacted at 39.1 kg.m/s.

4.2.2. Metallographic analysis

4.2.2.1. Overview

Figure 4.19 shows the optical micrographs of the original AISI 1340 steel after the various heat treatment conditions before the dynamic impact test. The quenched and tempered steel specimens consist of martensitic plates and retained austenite (Fig. 4.19a). The white phase in the microstructure of the quenched and tempered steel is untransformed austenite. The normalised steel specimen consists of pearlite and ferrite (Fig. 4.19b). Phase analysis of the microstructure using Pax-it software shows that the pearlitic specimen contains 11 vol. % pearlite and 89 vol. % ferrite. The steel subjected to inter-critical annealing at 740 ˚C before quenching shows the dual-phase microstructure consisting of 20 vol. % ferrite (bright) and 80 vol. % martensite (dark phase) as shown in Fig. 4.19c.

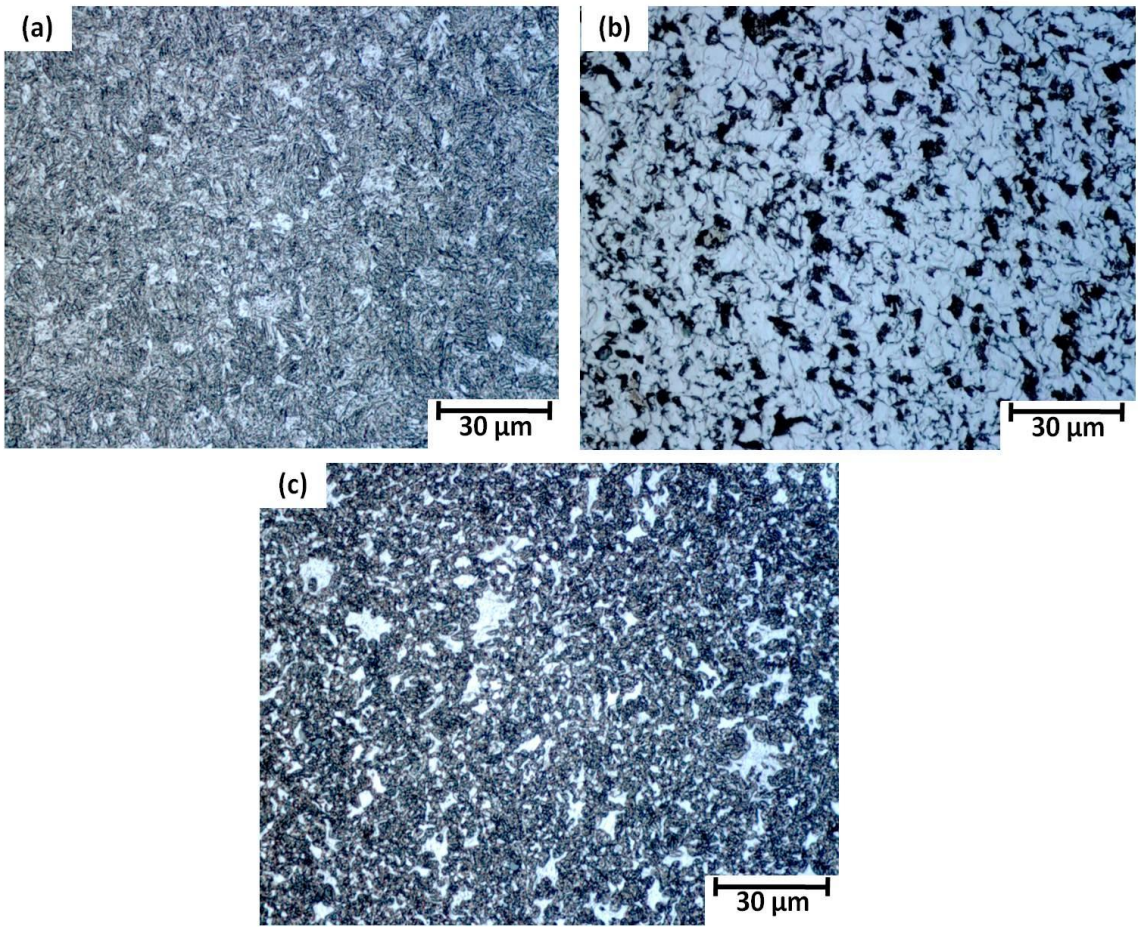

Figure 4.19. Optical micrographs of AISI 1340 steel specimens before impact test: (a) austenitized at 850 °C, water- quenched and tempered at 315 °C – martensitic structure, (b) austenitized at 850 °C and air-cooled – pearlitic structure, (c) austenitized at 740 °C, water-quenched and tempered at 315 °C - dual-phase structure.

Figure 4.20 shows the optical micrographs of the original AISI 4340 steel after the various heat treatment procedures before impact test. The quenched and tempered steel consists of martensitic plates and retained austenite (Fig. 4.20a). The normalised steel specimen consists of pearlite and ferrite (Fig. 4.20b). Phase analysis of the microstructure using Pax-it software shows that the pearlitic specimen contains 35 vol. % pearlite and 65 vol. % ferrite. The steel subjected to inter-critical annealing at 740˚C before quenching also shows martensitic structure (Fig. 4.20c). Unlike AISI 1340 manganese steel, a dual-phase microstructure could not be formed in AISI 4340 steel at 740˚C. The significant amount of manganese in AISI 1340 steel widens the ferrite + austenite region in the iron-iron carbide equilibrium phase diagram. Therefore, by austenitizing AISI 1340 specimens inside this region at 740˚C mixture of austenite and ferrite are formed which are then converted to martensite + ferrite on quenching in water. However, AISI 4340 steel does not have a sufficient amount of manganese, which can expand ferrite-austenite region in the iron-iron carbide phase diagram. Moreover, the presence of nickel could expand the austenite phase region [82] to 740˚C. Thereby, complete austenitization can occur at 740˚C. This explains why quenching the AISI 4340 steels from 740˚C produced an entirely martensitic microstructure.

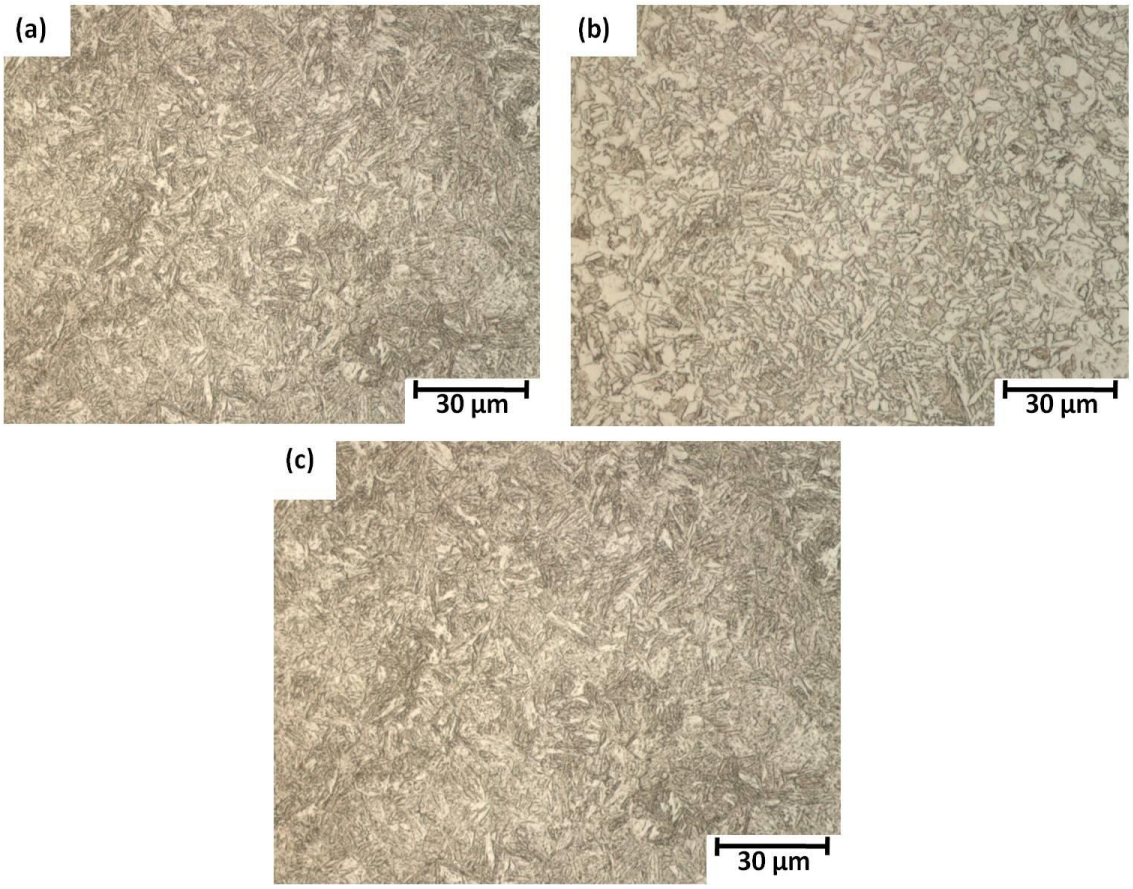

Figure 4.20. Optical micrographs of AISI 4340 steel specimens before impact test: (a) austenitized at 850 °C, oil- quenched and tempered at 315 °C – martensitic structure, (b) austenitized at 850 °C and air-cooled – pearlitic structure, (c) austenitized at 740 °C, oil-quenched and tempered at 315 °C - martensitic structure.

4.2.2.2. The effect of impact momentum

During high velocity impact, a high proportion of the kinetic energy of the impacting projectile is converted to heat inside the material. Since the deformation occurs very quickly, this heat generated inside the material cannot be conducted away along a narrow path inside the material. Therefore, the temperature of this localized area increases, which causes intense plastic deformation, high shear strains and strain-rates along this narrow path called the Adiabatic Shear Band (ASB). Figure 4.21 shows optical micrographs of martensitic AISI 1340 steel (tempered at 315˚C) impacted at different impact momentums. At the impact momentum of 34.2 kg.m/s (Fig. 4.21a), the strain rate inside the adiabatic shear band is just enough to slightly align the martensite and carbide particles along the adiabatic shear band propagation path and form a light deformed shear band observed in the specimen. As the impact momentum, and consequently the strain rate, increases, the intense strain inside the shear band becomes sufficiently high to break martensite plates and carbide laths into sub-micron size particles, forming a transformed shear band along which cracking occurs, as shown in Fig. 4.21d. Figure 4.22 shows the process of crack formation along a transformed adiabatic shear band in a martensitic AISI 1340 steel specimen impacted at 42.1 kg.m/s. As the impact momentum reaches 42.1 kg.m/s, the strain-rate and temperature rise within the adiabatic shear band are high enough to generate tensile stress inside the shear band and open up micro-voids, which cause crack to form along the adiabatic shear band propagating path [78].

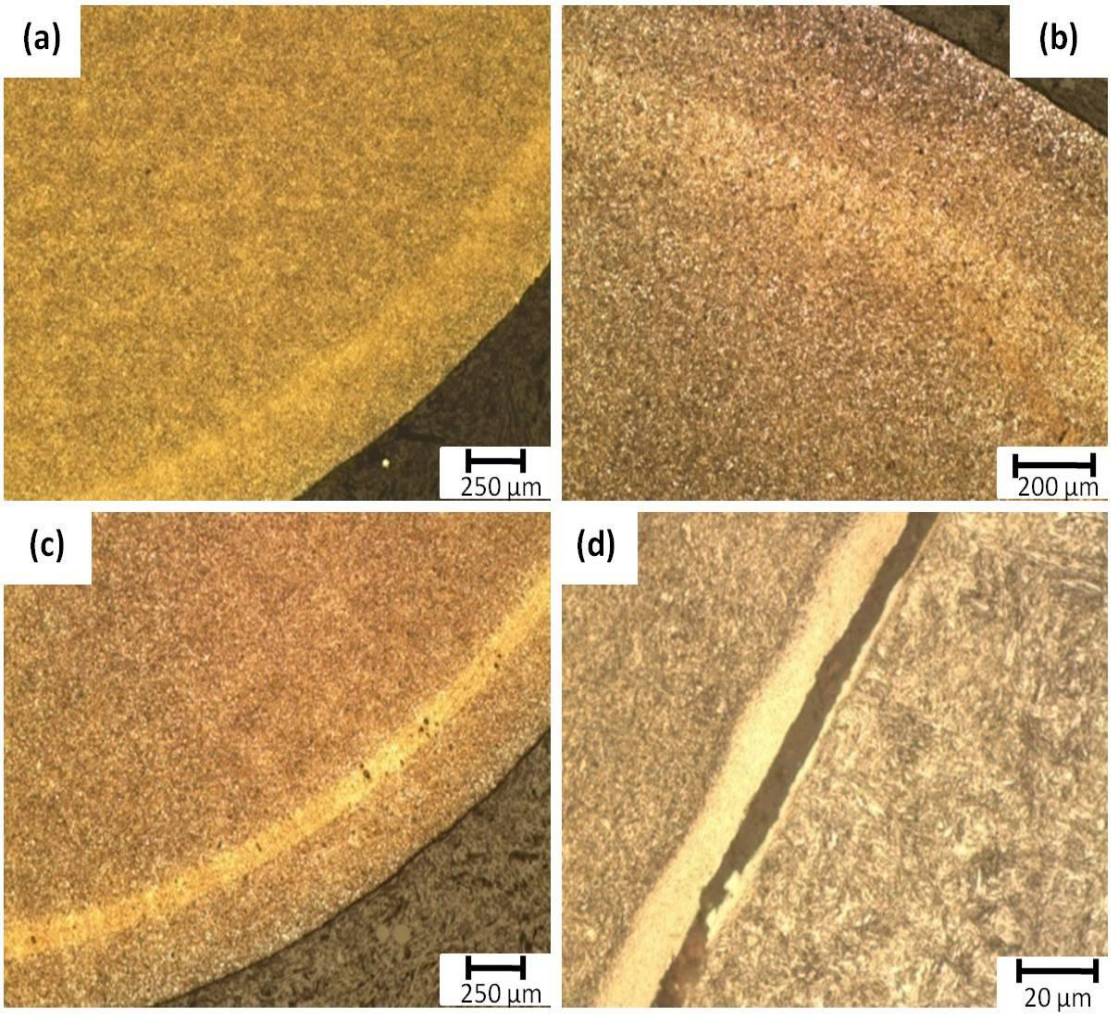

Figure 4.21. Optical micrographs of martensitic AISI 1340 steel, tempered at 315˚C, impacted at: (a) 34.2 kg.m/s, (b) 36.1 kg.m/s, (c) 39.1 kg.m/s, (d) 42.1 kg.m/s.

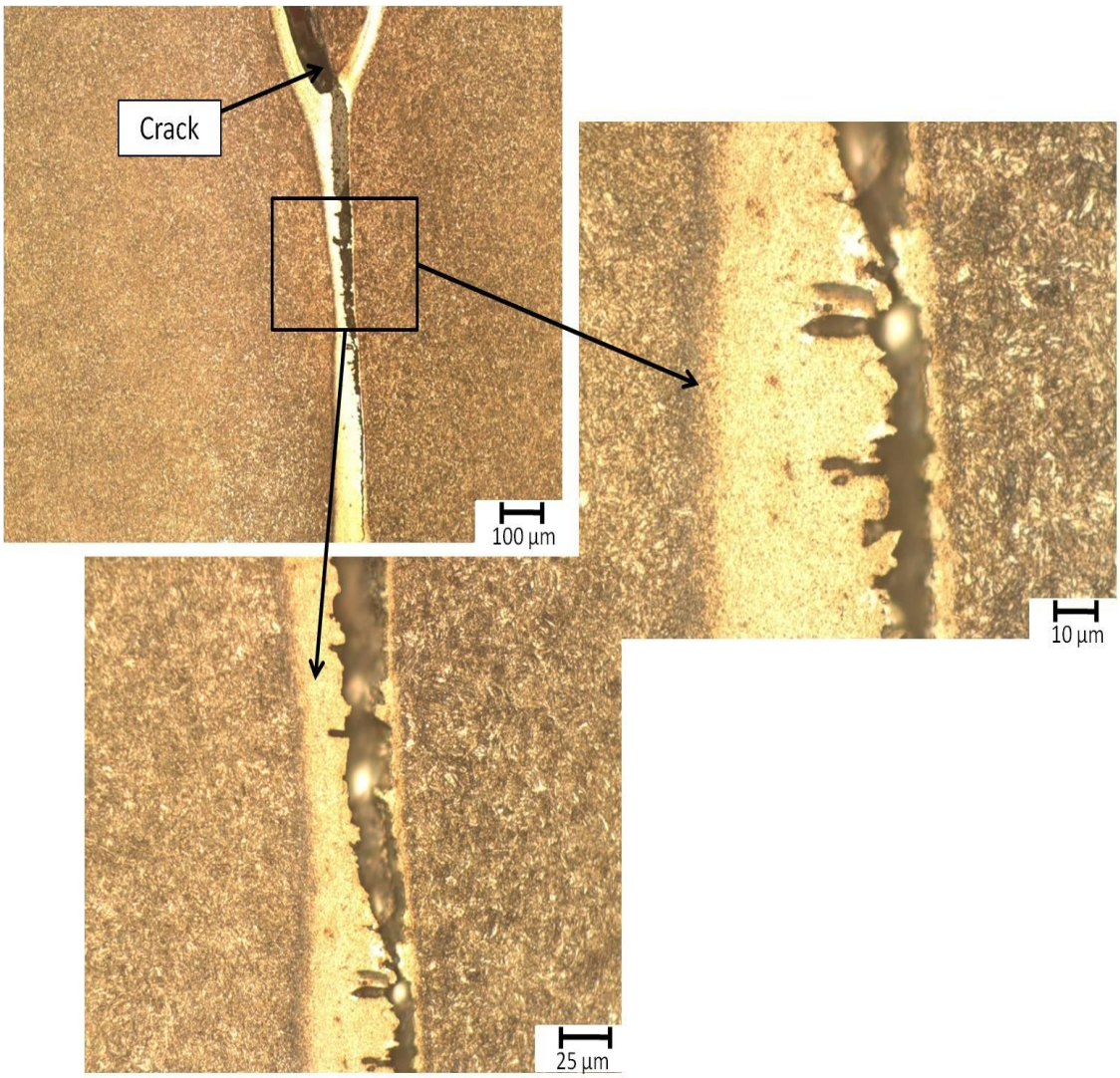

Figure 4.22. Optical micrographs of fractured cylindrical specimen martensitic AISI 1340 steel, tempered at 315˚C, impacted at 42.1 kg.m/s.

Figure 4.23 shows optical micrographs of pearlitic AISI 1340 steel specimens impacted at different impact momentums. It is observed that only deformed adiabatic shear bands form in steel specimens with pearlitic structure for all the impact momentums investigated. However, the morphology of the deformed shear bands is somewhat different from what has been observed in other steels, such as AISI 4340 steel, in which shearing on the grains was inclined to specimen's diameter [83]. It is observed in the current study on AISI 1340 steel that the pearlite and ferrite are aligned radially along the diameter of circular transverse cross-sectional area. As the impact momentum increased, the thickness of deformed shear band increased, but a transformed shear band was not formed. No fracture was observed for pearlitic specimens even at impact momentums at which fracture occurred for martensitic and dual-phase structure specimens. At high impact momentums, pearlite and ferrite particles are closely packed together and form a thick deformed shear band. However, at a low impact momentum of 34.2 kg.m/s, there was no evidence of adiabatic shear band formation in the pearlitic specimen.

SEM micrographs showing the microstructure of pearlitic AISI 1340 steel within the regions inside and outside the adiabatic shear band are presented in Fig. 4.24. It is obvious that pearlite and ferrite grains are smaller inside the deformed band than outside. This is attributed to the high strain-intensity inside the shear band, which is high enough to fragment the large pearlite and ferrite grains in this region.

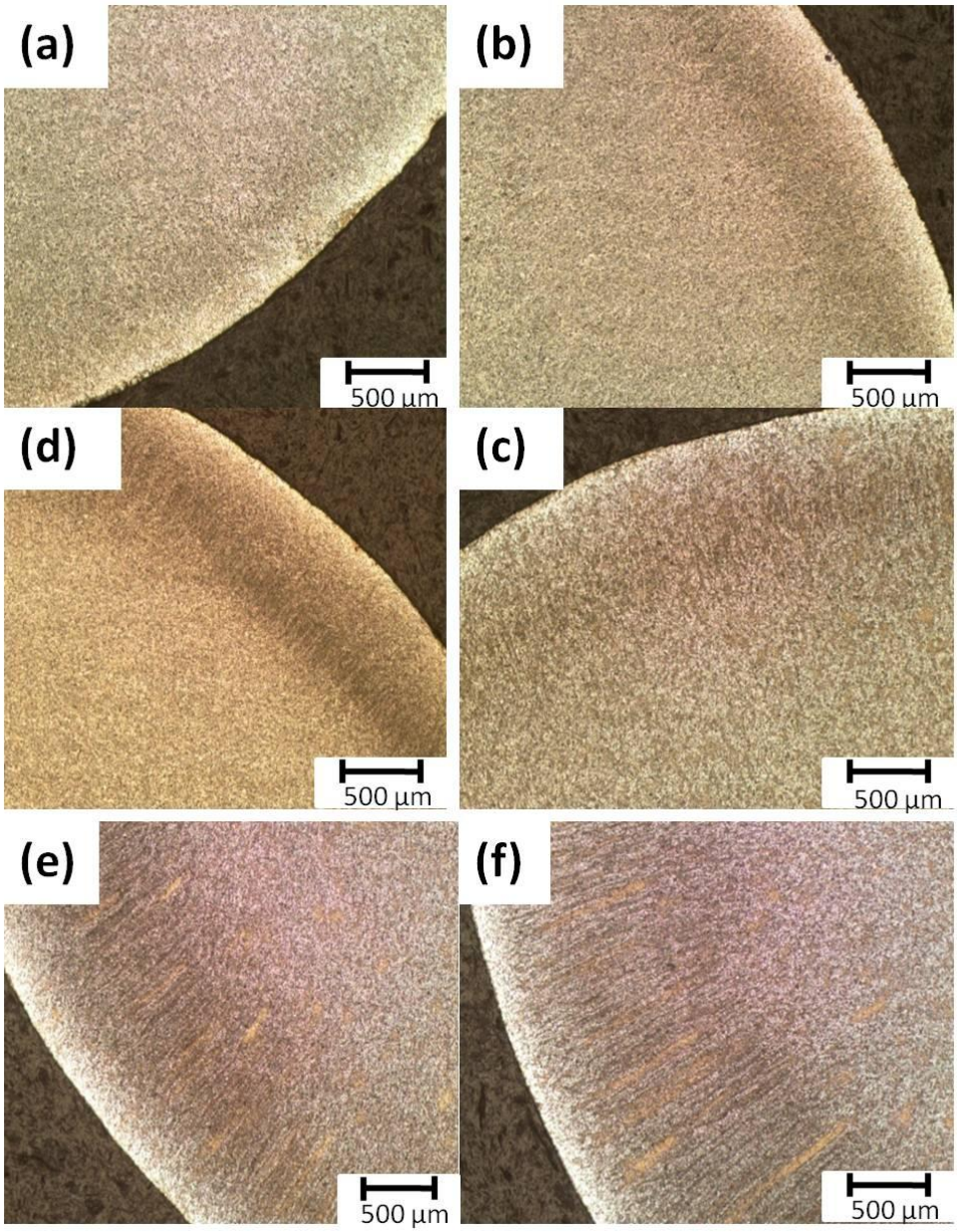

Figure 4.23. Optical micrographs showing deformed bands in the pearlitic AISI 1340 steel, Impacted at: (a) 34.2 kg.m/s, (b) 36.1 kg.m/s, (c) 39.1 kg.m/s, (d) 42.1 kg.m/s, (e) 44.1 kg.m/s, (f) 49.1 kg.m/s.

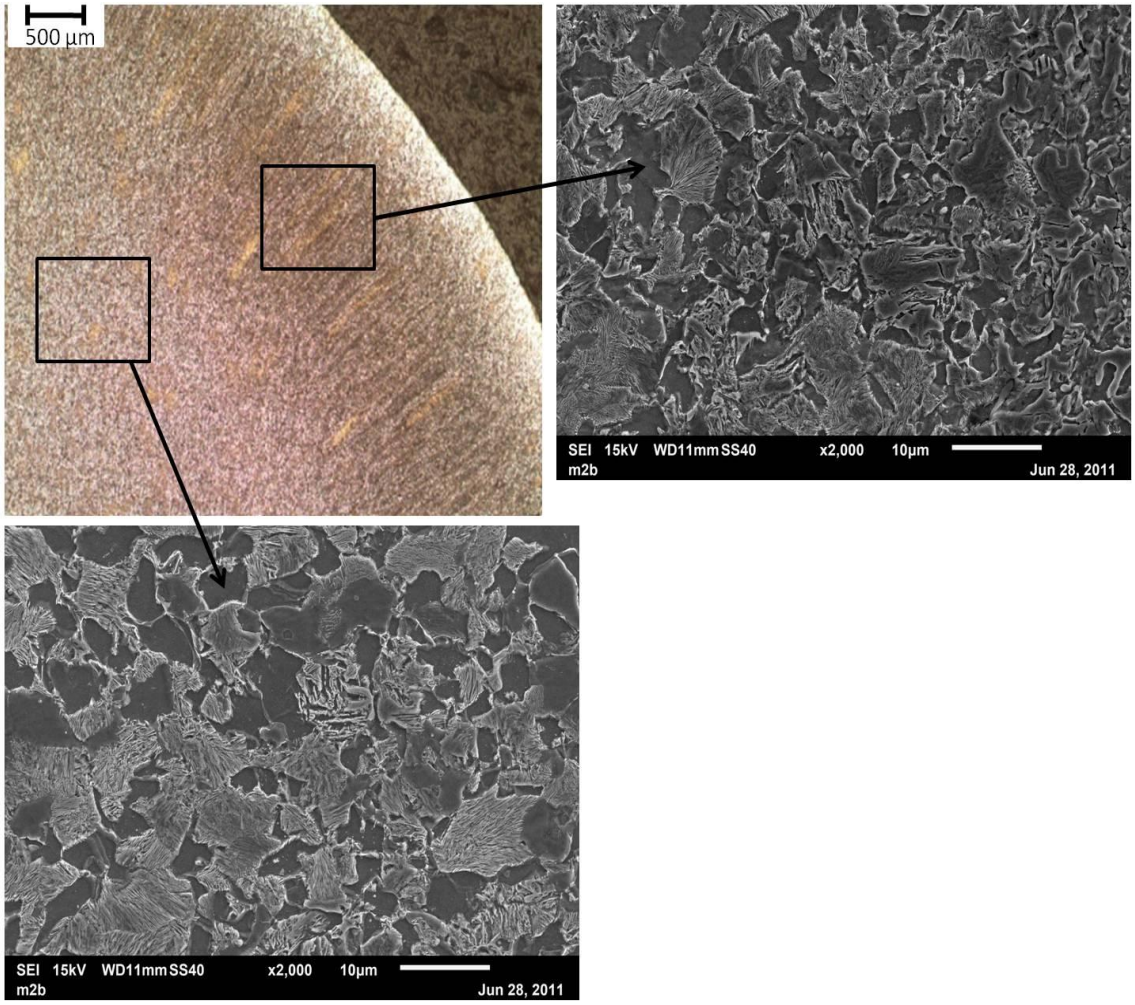

Figure 4.24. SEM micrographs of pearlitic AISI 1340 steel showing microstructure inside and outside the shear band (impacted at 44.1 kg.m/s).

Figure 4.25 shows optical micrographs for AISI 1340 steel specimens with the dual-phase structure impacted at different momentums. At 36.1 kg.m/s impact momentum, a deform shear band is formed. As the impact momentum increased, an intense white etching band, also called transformed adiabatic shear bands, formed. As the impact momentum increased, shear strain became more intensely localised in the shear bands. Finally, at an impact momentum of 42.1 kg.m/s, fracture occurred in the dual-phase structure specimen along the transformed shear band propagation path. As mentioned above, at a lower impact momentum, the strain rate is just enough to align martensite and ferrite particles along the shear stress direction. As the impact momentum and consequently the strain-rate increased, the intensity of shear strain inside the shear band became intense and caused fragmentation of martensite laths and ferrite particles along the shear band propagation path.

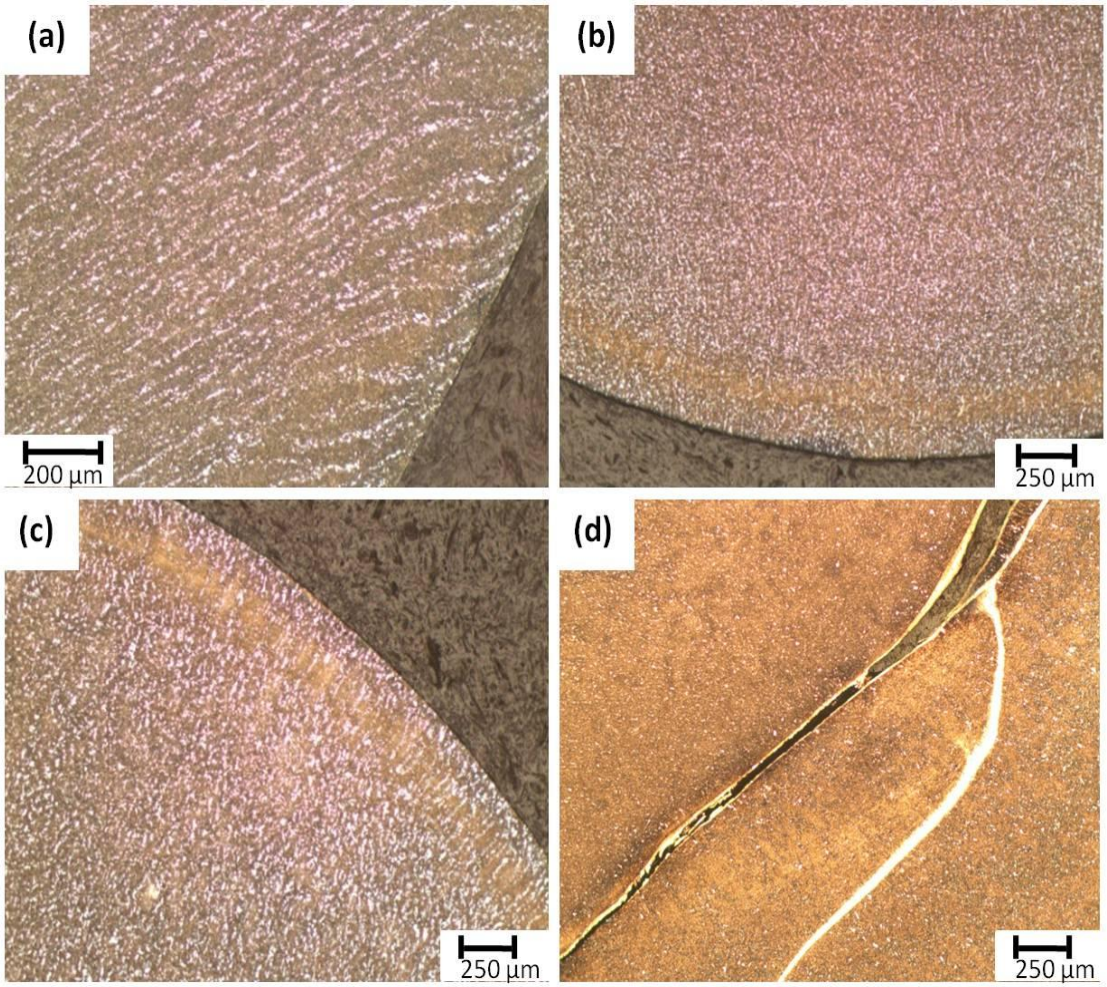

Figure 4.25. Optical micrographs for dual-phase AISI 1340 steel (tempered at 315˚C), impacted at: (a) 36.1 kg.m/s, (b) 38.1 kg.m/s, (c) 39.1 kg.m/s, (d) 42.1 kg.m/s.

SEM micrographs showing the microstructure of the dual-phase structure AISI 1340 steel within regions inside and outside the adiabatic shear band are presented in Fig. 4.26. The shear band imaged here is not a fully formed transformed band that will normally appear featureless under an optical (Fig. 4.25d) and SEM. It is observed that materials inside the shear band have less martensite and more ferrite than outside. It is not very clear at this stage why more ferrite is observed inside the shear band. However, it has been suggested that the combined action of hydrostatic pressure on the shear band and high temperature of the shear band can promote a carbon and iron diffusion path that can lead to the formation of ferrite [42]. Wittman *et al.* [20] also reported carbon diffusion aided by dislocation in AISI 4340 steel. Derep [67] observed that the microstructure of adiabatic shear band in armour steel consists of fine grain equi-axed structure of delta ferrite, mixed with narrow laths of martensite.

Figure 4.27 shows the optical micrographs for cracks in the dual-phase structure AISI 1340 steel specimens which fractured at 42.1 kg.m/s impact momentum. The crack formed along the transformed adiabatic shear band. At 42.1 kg.m/s impact momentum, the strain rate inside the adiabatic shear band of the dual-phase structure AISI 1340 steel specimen is high enough to generate micro-voids inside the shear band. These micro-voids interconnect and form cracks.

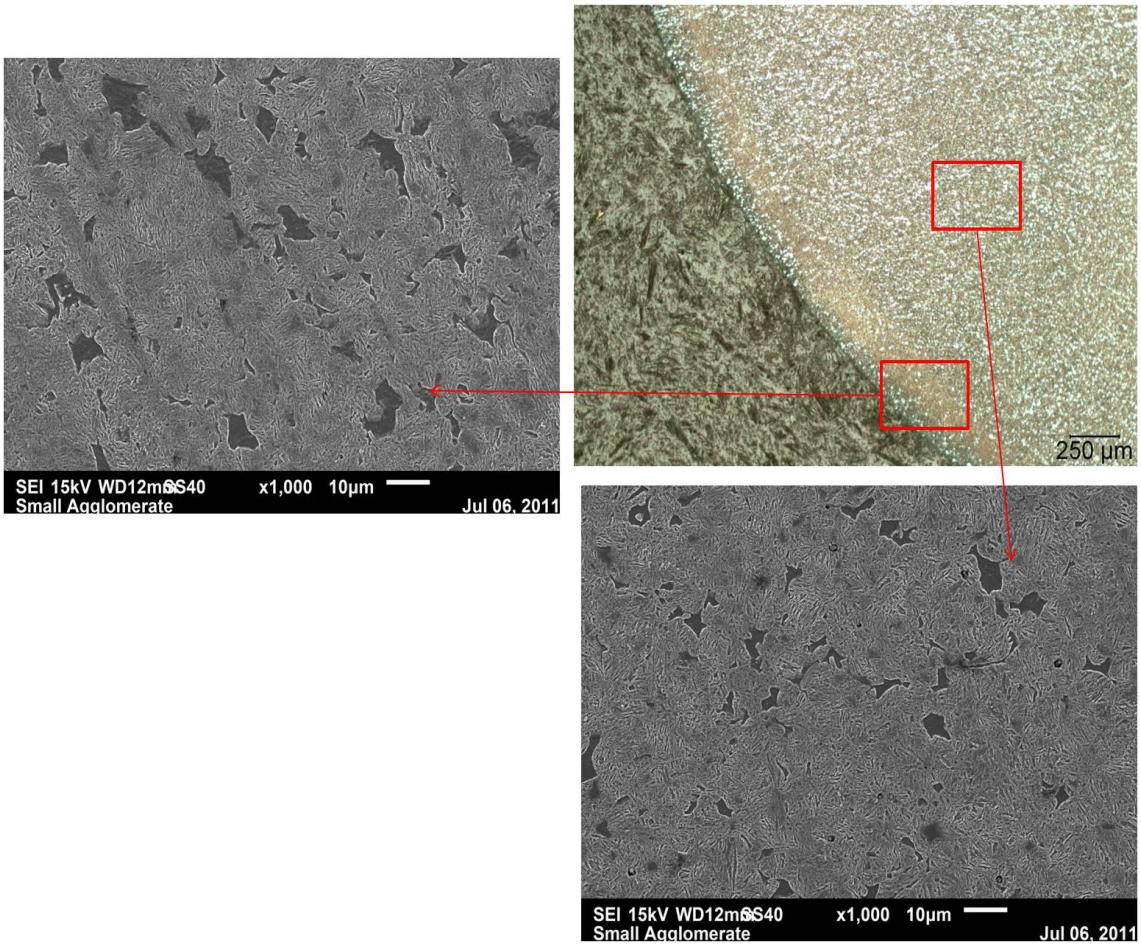

Figure 4.26. Optical and SEM micrographs of regions inside and outside the shear band for dual-phase AISI 1340 steel, tempered at 315˚C, impacted at 39.1 kg.m/s.

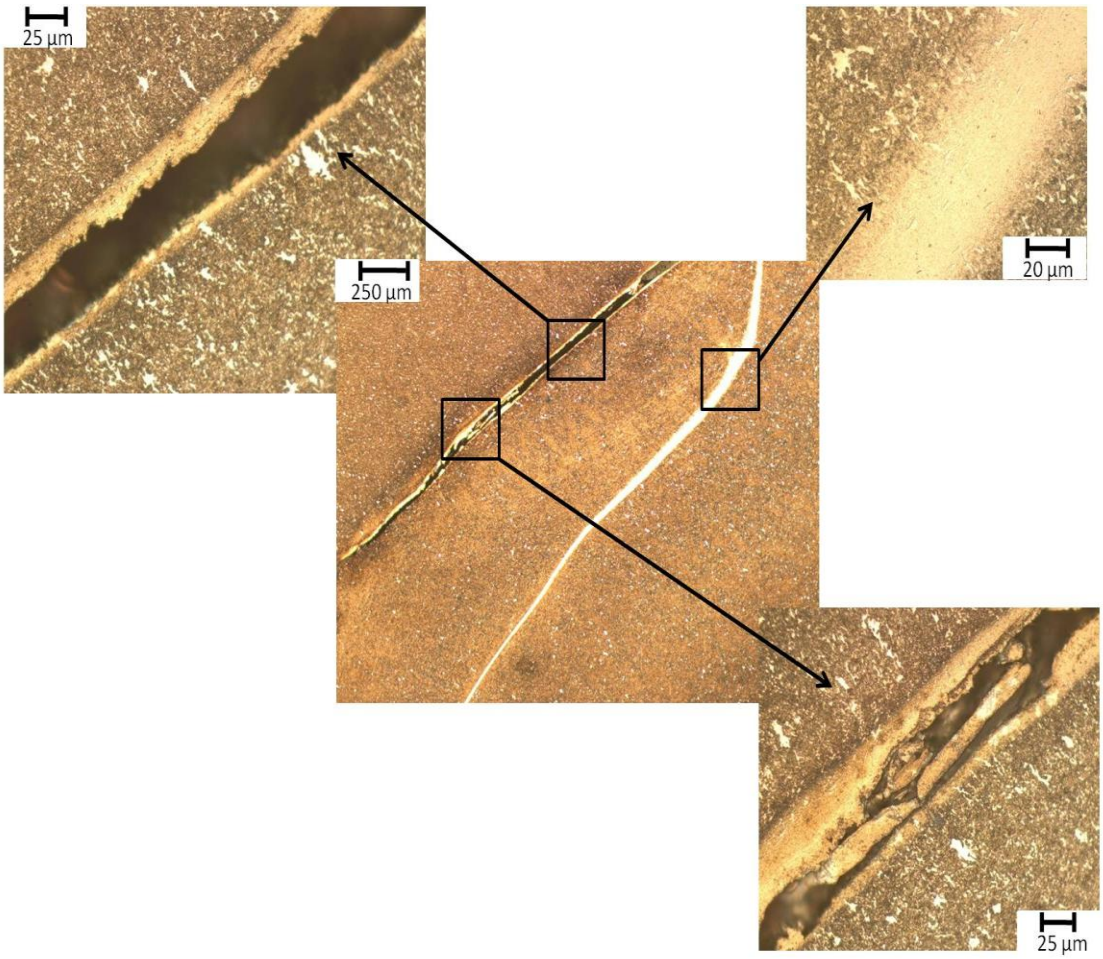

Figure 4.27. Optical micrographs showing adiabatic shear failure of dual-phase steel (AISI 1340), impacted at 42.1 kg.m/s.

4.2.2.3. The effect of microstructure

Optical micrographs showing the effects of tempering temperature on plastic deformation of martensitic AISI 1340 steel impacted at 34.1 kg.m/s are represented in Fig. 4.28. A thin intense white etching band was formed in the specimen that was tempered at 205˚C, while a thicker light deformed band was formed in the specimen which was tempered at 425˚C. The shear band for the specimen that was tempered at 315˚C had intermediate properties between the other two specimens. It is a more diffused form of white etching band.

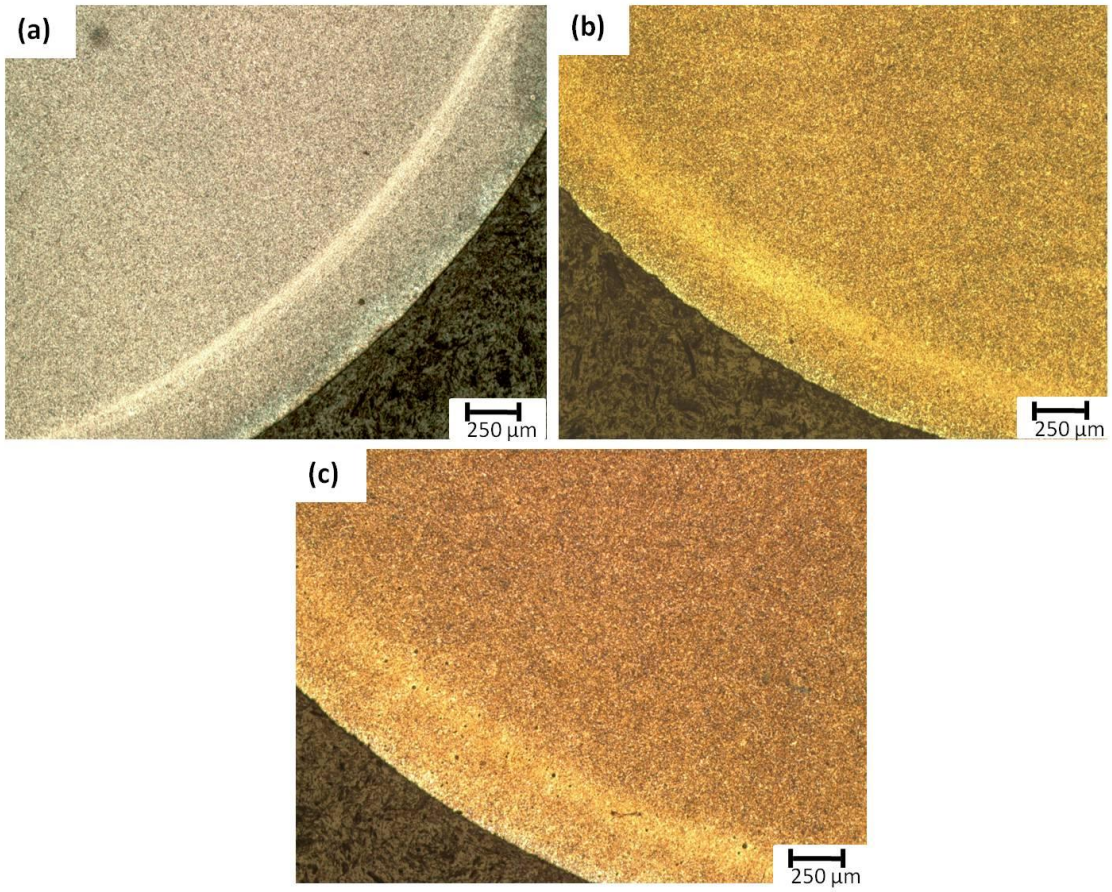

Figure 4.28. Optical micrographs of martensitic AISI 1340 steel, impacted at 34.1 kg.m/s, cylindrical specimens: (a) tempered at 205˚C, (b) tempered at 315˚C, (c) tempered at 425˚C.

It has been suggested by Rittel *et al.* [45], that the existence of defects such as abrasive particles and precipitates or any inhomogeneities inside the microstructure of metallic materials increases the susceptibility of materials to strain localization and formation of an adiabatic shear band [45]. These defects and inhomogeneities within the microstructure of materials are called initial perturbations. The internal stresses and therefore perturbations are more pronounced in the specimen that was tempered at 205 °C. This promotes the intense strain localization and formation of a transformed adiabatic shear band. As the tempering temperature increases, the stress that may be introduced during quenching is more relieved and the initial perturbations will decrease. The uniform dispersion of precipitates, as well as relieved internal strains, decrease the susceptibility of the material to strain localization. Therefore, the martensite laths are just capable of aligning themselves and forming a wide deformed band.

The optical micrographs in Fig. 4.29 show the effect of microstructure, as a result of different heat-treatment procedure, on the plastic deformation of AISI 1340 steel impacted at 38.1 kg.m/s. Thin intense white etching band is observed for the specimen with a martensitic structure, while a thick light deform band was formed for specimens having a pearlitic structure. The specimens with dual-phase structure have intermediate properties between those having martensitic and pearlitic structures [Fig. 4.29(c)]. A clear deformed shear band with brighter color than the matrix has been observed for the dual-phase structure specimen. Stresses that are introduced during quenching into martensitic microstructure act as an initial perturbation and increase the susceptibility of the material to shear strain localization. For the pearlitic microstructure specimen, which was air-cooled to room temperature, no stress is introduced inside the material, which reduces the susceptibility of the material to shear strain localization along the shear band. Therefore, shear strain inside the shear band is just high enough to align the pearlite and ferrite grains along the shear flow direction, causing formation of a deformed adiabatic shear band. The dual-phase structure has intermediate properties between transformed band observed in the martensitic specimen and deformed band in the specimens with pearlitic structure. Dual-phase structure is a mixture of strong martensite and ductile ferrite. The martensite with internal stresses, as a result of quenching, increases the susceptibility of the material to shear strain localization. On the

other hand, ductile ferrite particles facilitate plastic deformation. Therefore, maximum temperature rise inside the adiabatic shear band is less for the dual-phase steel than for the martensitic steel.

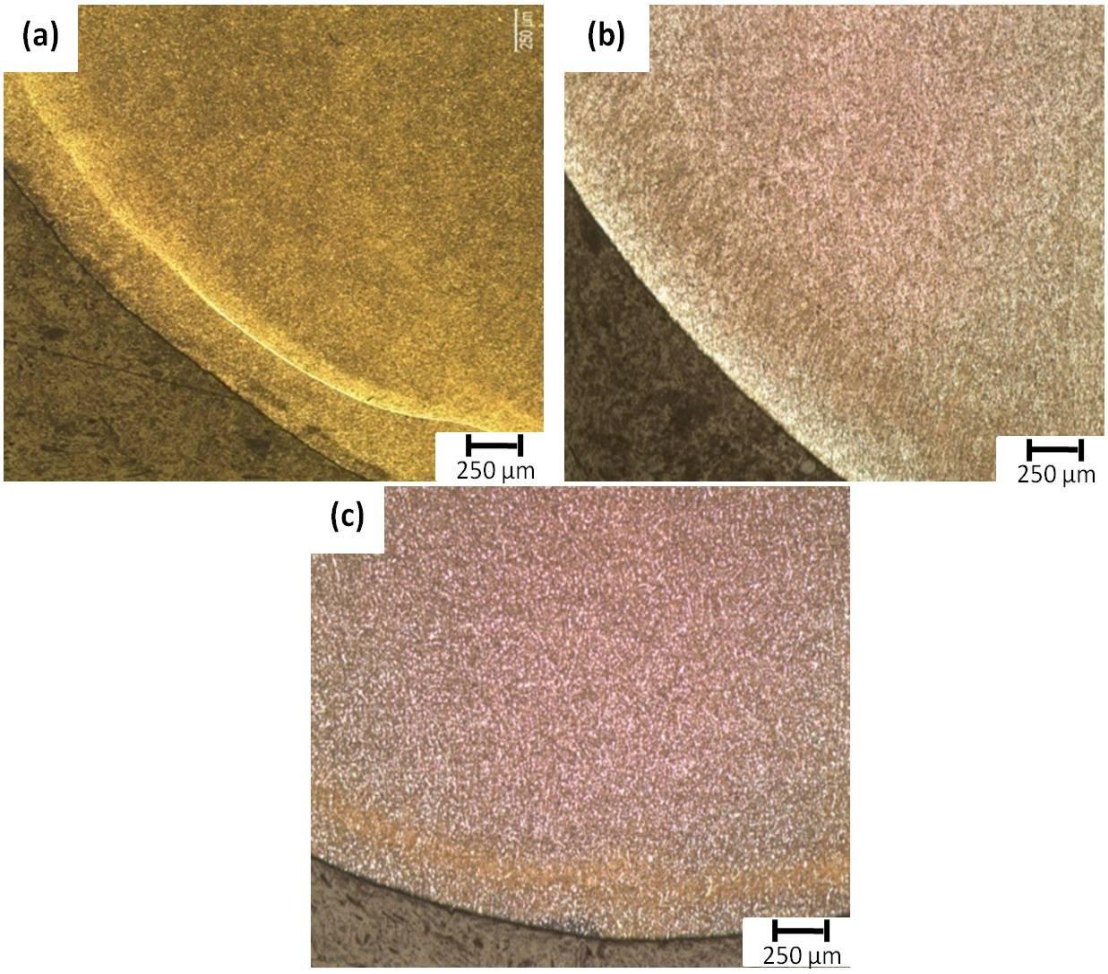

Figure 4.29. Optical micrographs of AISI 1340 steel, impacted at 38.1 kg. m/s, cylindrical specimen. (a) martensitic- tempered at 315°C, (b) Pearlitic, (c) Dual-phase structure.

Figure 4.30 shows the optical micrographs of martensitic AISI 1340 and 4340 steels that were tempered at 315˚C and impacted at 34.2 kg.m/s. Figure 4.30 (a) shows the micrograph for AISI 1340 alloy steel while Fig. 4.34 (b) is for AISI 4340 alloy steel. Figure 4.31 shows optical micrographs for cylindrical specimens that were austenitized at 740˚C, quenched-hardened and then tempered at 315˚C after impact at a momentum of 36.1 kg.m/s. Figure 4.31a and 4.31b show the micrographs for AISI 1340 steel and AISI 4340 steel, respectively. It is evident from both Figs. 4.30 and 4.31 that AISI 4340 steel is more inclined to form an adiabatic shear band than AISI 1340 steel when subjected to the same heat treat treatment condition. The presence of additional alloying elements such as Mo, Cr, Ni, and Mn increases the ability of material to form carbide particles which can act as initial perturbations and increases the susceptibility of the material to shear localization and the occurrence of adiabatic shear bands. Therefore, AISI 4340 alloy steel is more inclined to form an adiabatic shear band than AISI 1340 alloy steel. The same results have been observed from stress-strain curves of AISI 1340 and AISI 4340 steels. It should be mentioned that at 740˚C, AISI 4340 steel was not able to form dual-phase structure entirely, as previously explained.

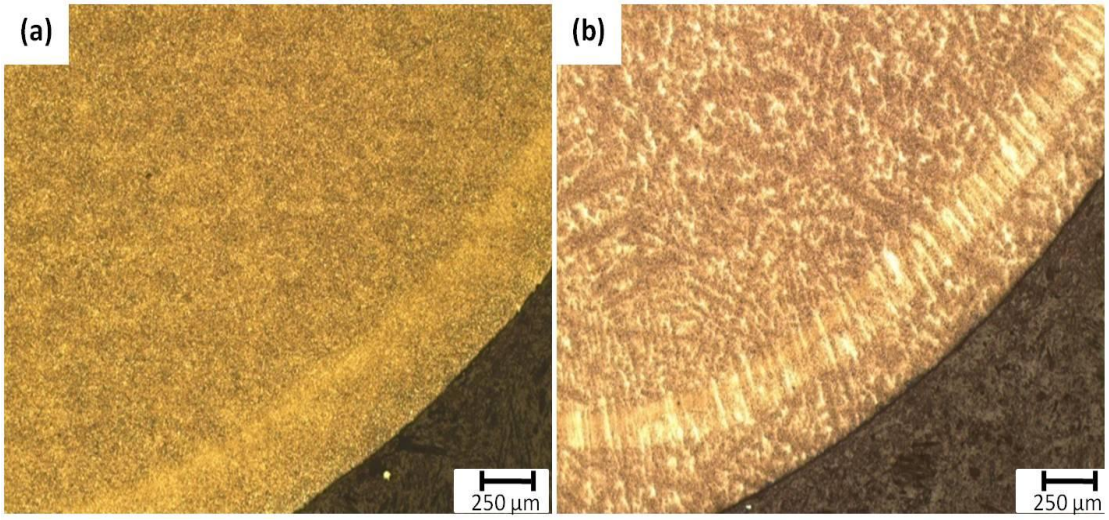

Figure 4.30. Optical micrographs of cylindrical specimen of martensitic steel, (tempered at 315˚C), impacted at 34.2 kg. m/s. (a)AISI 1340 steel, (b) AISI 4340 steel.

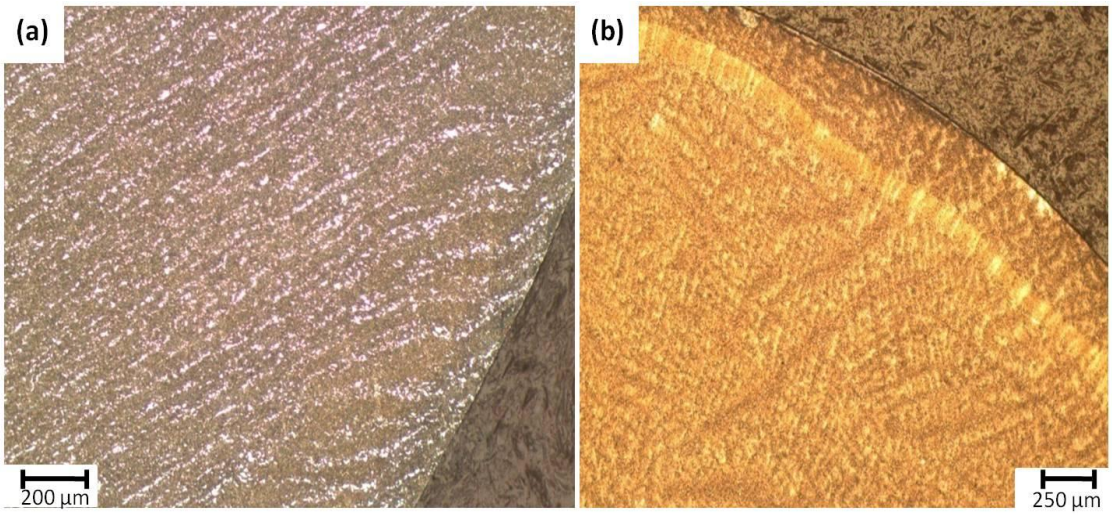

Figure 4.31. Optical micrographs of steel specimens partially austenitized at 740˚C, quenched-hardened and tempered at 315˚C - impacted at 36.1 kg. m/s: (a)AISI 1340 steel, (b) AISI 4340 steel.

4.2.2.4. The effect of geometry

Optical micrographs of the transverse cross-section of impacted martensitic AISI 1340 steel and AISI 4340 steel specimens showing the effects of specimen shape on the geometry of adiabatic shear band on the transverse section of the specimen are presented in Figs. 4.32 and 4.33, respectively. The specimens shown in these figures were impacted at a momentum of 36.1 kg.m/s. It is observed that the geometry of adiabatic shear band depends on the geometry of the specimen. The shear band in the cylindrical specimen appears as a circle on the transverse cross-sectional area [Figs. 4.32 (c), and 4.33 (a)], while in cubic specimens, it appears as a square on the transverse cross-sectional area [Figs. 4.32 (a), 4.32 (b), and 4.33 (b)]. The shear bands form a circular path on the transverse section close to the diametrical surface with smaller radius in the specimens having the shape of truncated cone [Fig. 4.33 (c)], while no shear band was observed on the transverse section close to the base of the truncated cone with the larger cross sectional area [Fig. 4.33(d)]. It should be noted that the conical specimen was impacted on the diametrical surface with the smaller radius. In comparison to the cylindrical martensitic specimen tempered at the same temperature and impacted at the same momentum, the cubic samples and the region of the conical specimen with smaller

transverse cross sectional area have more intense shear localization. This is attributed to the higher stress concentration within the sharp corners for the cubic specimen and the uneven transverse cross sectional area in the conical sample, which could act as the initial source of perturbation that promotes the occurrence of the intense white etching bands. The optical macrographs showing the effects of specimen geometry on the geometry of adiabatic shear bands along the longitudinal cross-section of impacted specimens are presented in Fig. 4.34.

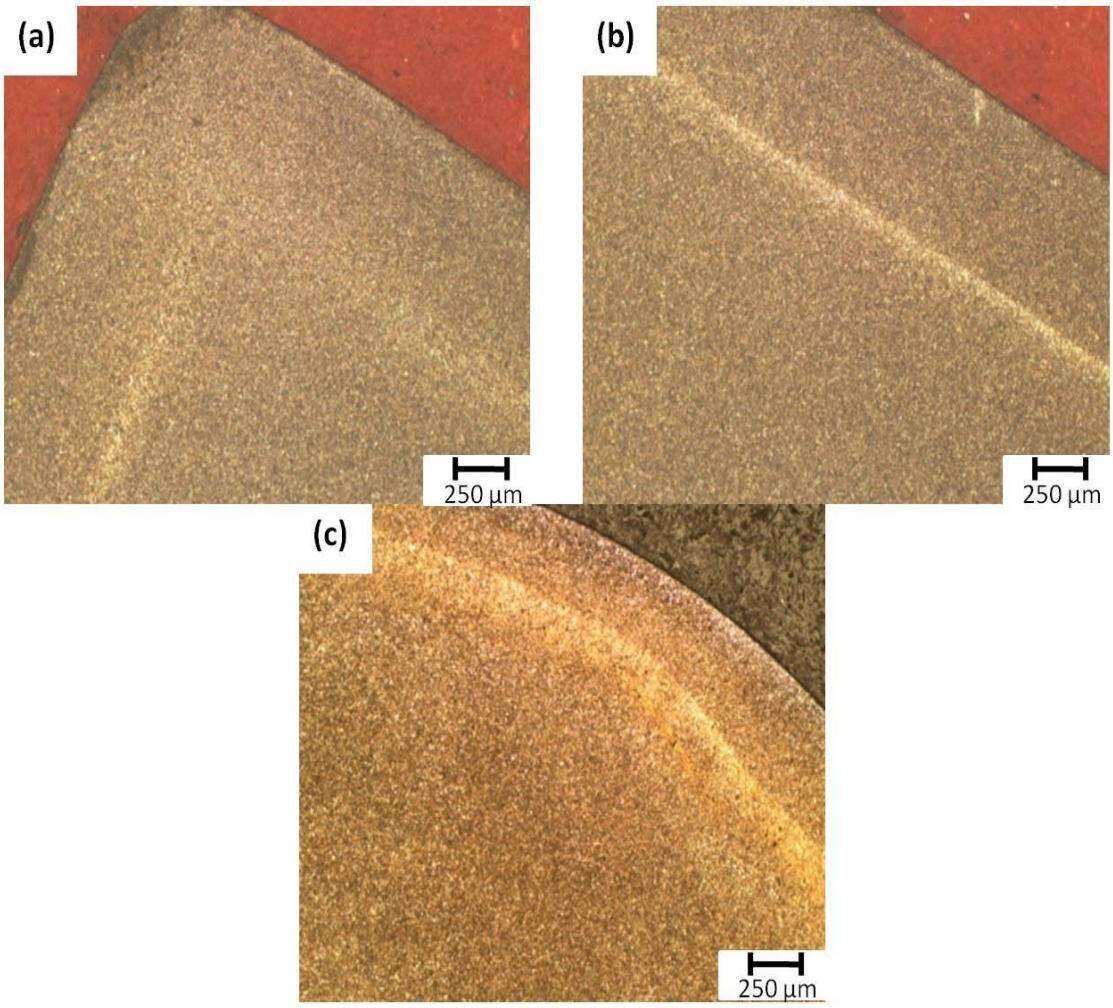

Figure 4.32. Optical micrographs of martensitic AISI 1340 steel, tempered at 315˚C, impacted at 36.1 kg.m/s: (a) cubic sample corner, (b) cubic sample close to the edge, (c) cylinder.

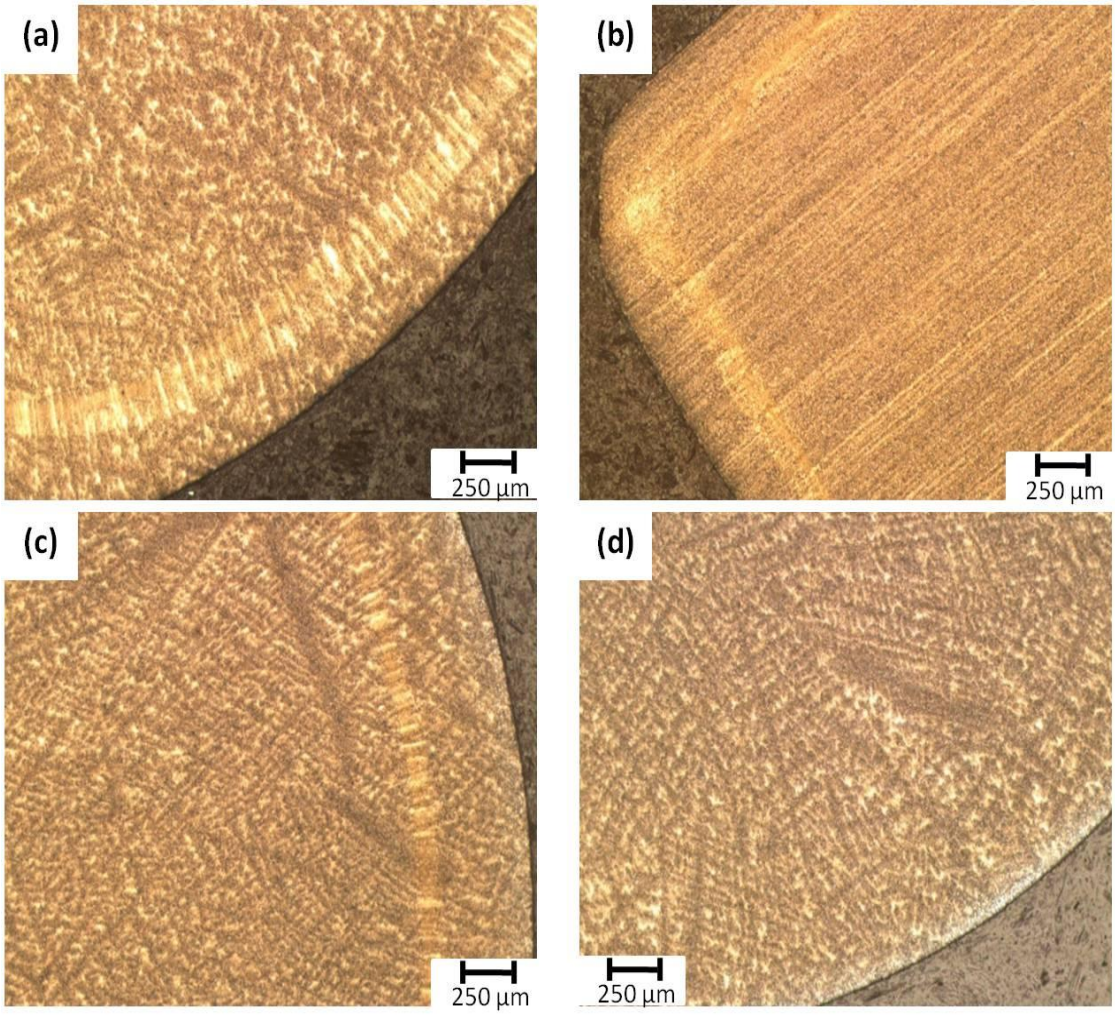

Figure 4.33. Optical micrographs of martensitic AISI 4340 steel, tempered at 315˚C, impacted at 34.2 kg.m/s: (a) cubic, (b) cylinder, (c) truncated cone(small cross-section), (d) truncated cone(large cross-section).

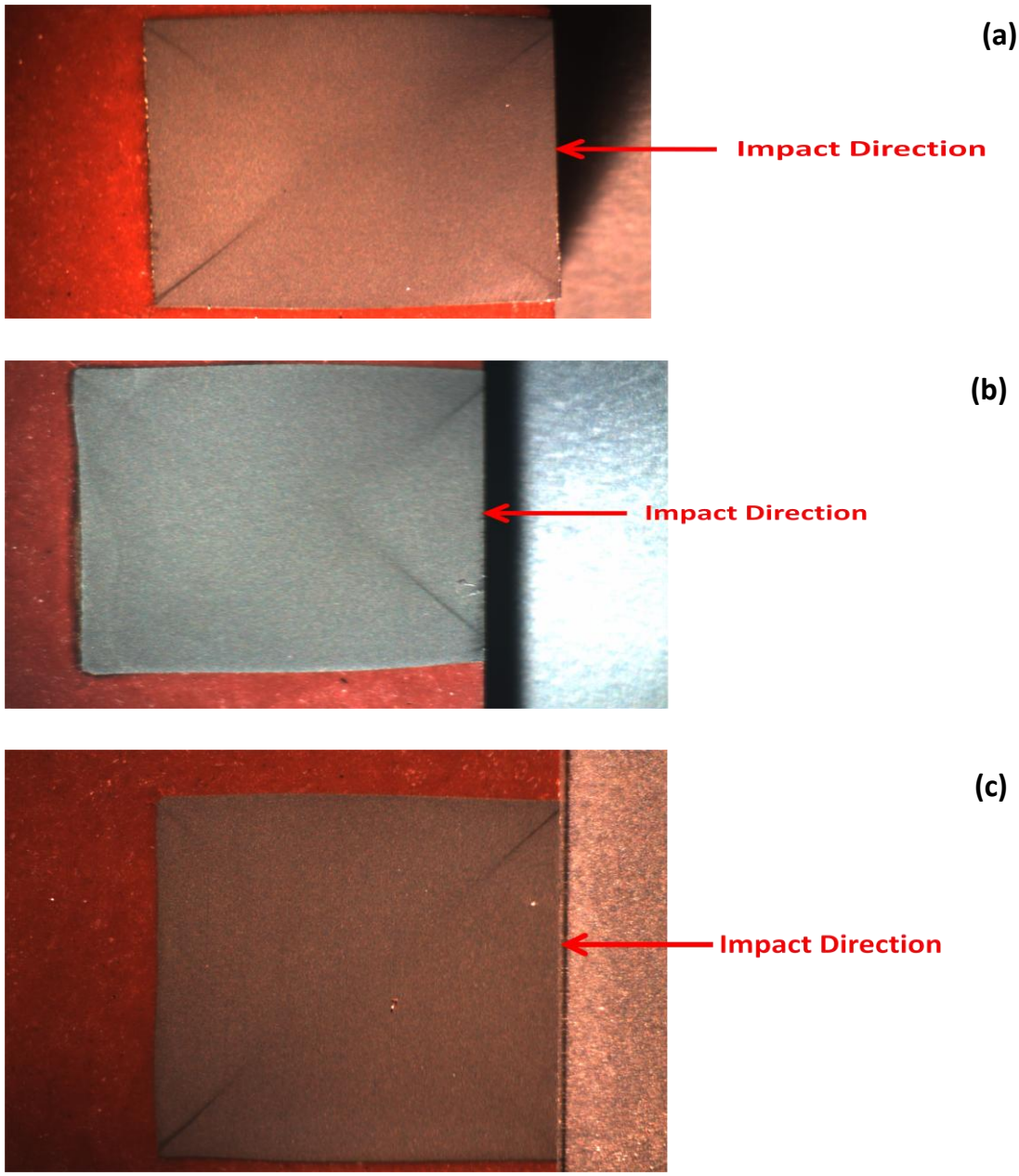

Figure 4.34. Optical macrographs for martensitic AISI 4340 steel, tempered at 315˚C, 34.2 kg.m/s: (a) cylindrical, (b) conical, (c) cubical specimen.

From the optical micrographs of adiabatic shear bands on both transverse and longitudinal sections of the steel, geometrical models of adiabatic shear bands in three dimensions are proposed as presented in Fig. 4.35. For cylindrical specimens, shear bands form two cones that are mirror images of one another. Two pyramidal shape shear bands are formed in cubical specimens, which are also mirror images of one another. For the truncated conical specimen, the adiabatic shear band appears as just one cone protruding from the smaller transverse cross-sectional area of the specimen.

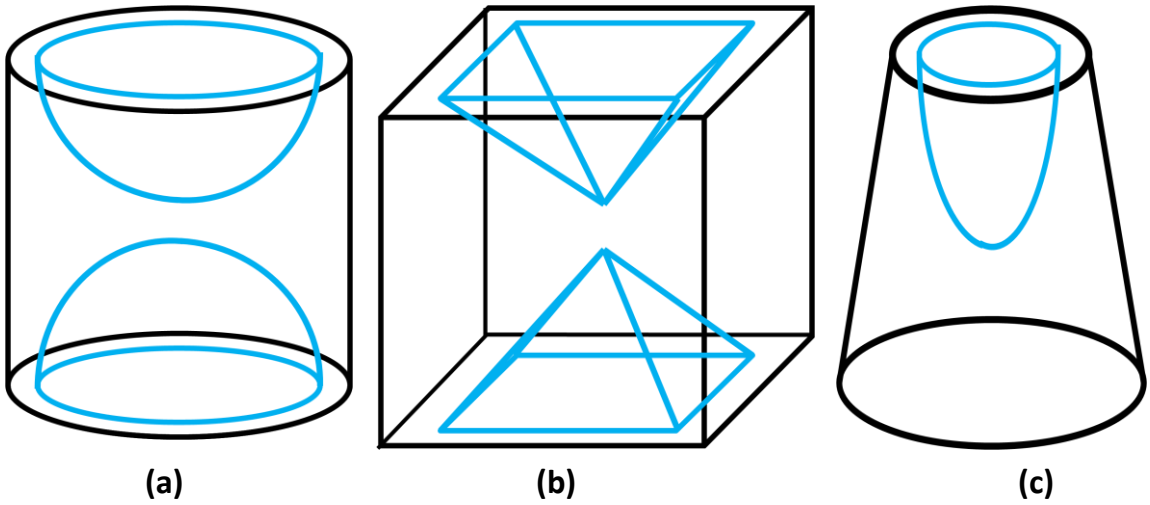

Figure 4.35. Schematic view of adiabatic shear band in (a) cylindrical, (b) cubical, (c) conical specimens.

4.3. Fracture of impacted specimens

Figure 4.36 shows the optical micrograph of a crack along transformed adiabatic shear bands for different specimens with different chemical composition, microstructure, and geometry. It is observed that failure and fracture occur along the transformed band, independent of chemical composition, microstructure, and geometry of the specimen. It should be noted that for pearlitic structure specimens, which were impacted in the strain-rate range of between 1376 s^{-1} to 7889 s^{-1}, only deformed bands are observed. Therefore, no transformed shear band and consequently no failure occur for pearlitic specimens in this strain-rate range.

Figures 4.37 and 4.38 and show the optical and SEM micrographs of transformed adiabatic shear bands in martensitic AISI 1340 steel specimen that was tempered at 315 ˚C and was impacted at 42.1 kg.m/s. The existence of elliptical shape holes along the crack are evidence of the micro-void formation along the transformed adiabatic shear band. At this impact momentum, the stress flow difference inside and outside of the white etching adiabatic shear band is high enough to produce tensile stress inside the shear band [78]. This tensile stress opens up micro-pores along the white shear band. These micro-pores connect to one another and form cracks along the transformed adiabatic shear band [76].

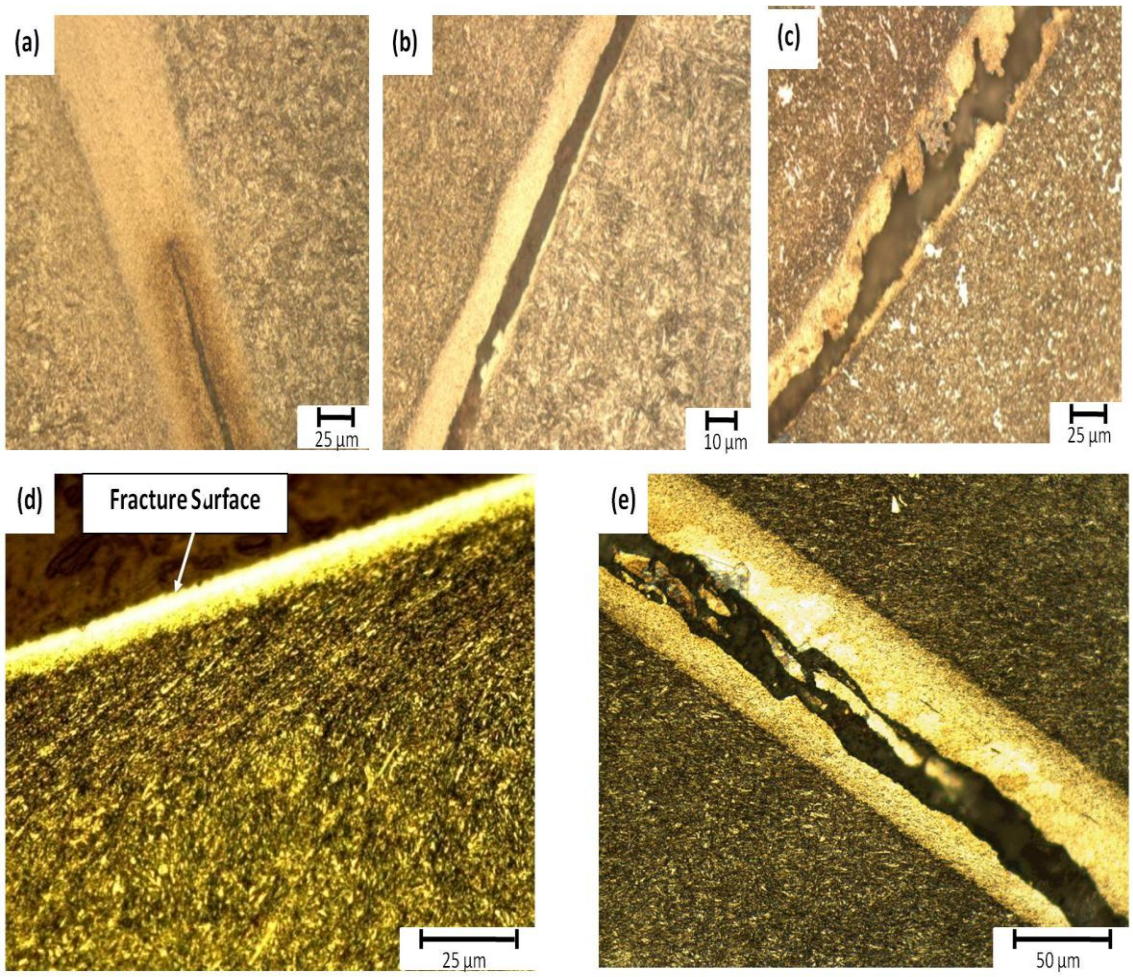

Figure 4.36. Optical micrograph showing cracks along a white etching band: (a) martensitic AISI 1340 steel, tempered at 425˚C, cylindrical specimen, impacted at 42.1 kg.m/s, (b) martensitic AISI 1340 steel, tempered at 315˚C, cylindrical specimen, impacted at 42.1 kg.m/s, (c) dual-phase structure AISI 1340 steel, tempered at 315˚C, cylindrical specimen, impacted at 44.1 kg.m/s, (d) martensitic AISI 1340 steel, tempered at 315˚C, cubic specimen, longitudinal cross-sectional area, (e) martensitic AISI 4340 steel, tempered at 315˚C, cylindrical specimen, impacted at 38.1 kg.m/s.

Although the microstructural features of a transformed adiabatic shear band can not be resolved using optical microscope, SEM micrographs of the transformed adiabatic shear band suggest fragmentation of martensite laths into submicron size particles, as shown in Fig. 4.38. The development of cracks from voids nucleated by tensile stress generated inside the shear band is also evident in the SEM micrograph shown in Fig. 4.38. At high impact momentum, the strain-rate inside the shear band is high enough to break apart martensite laths into very small carbide particles which cannot be detected by optical microscope.

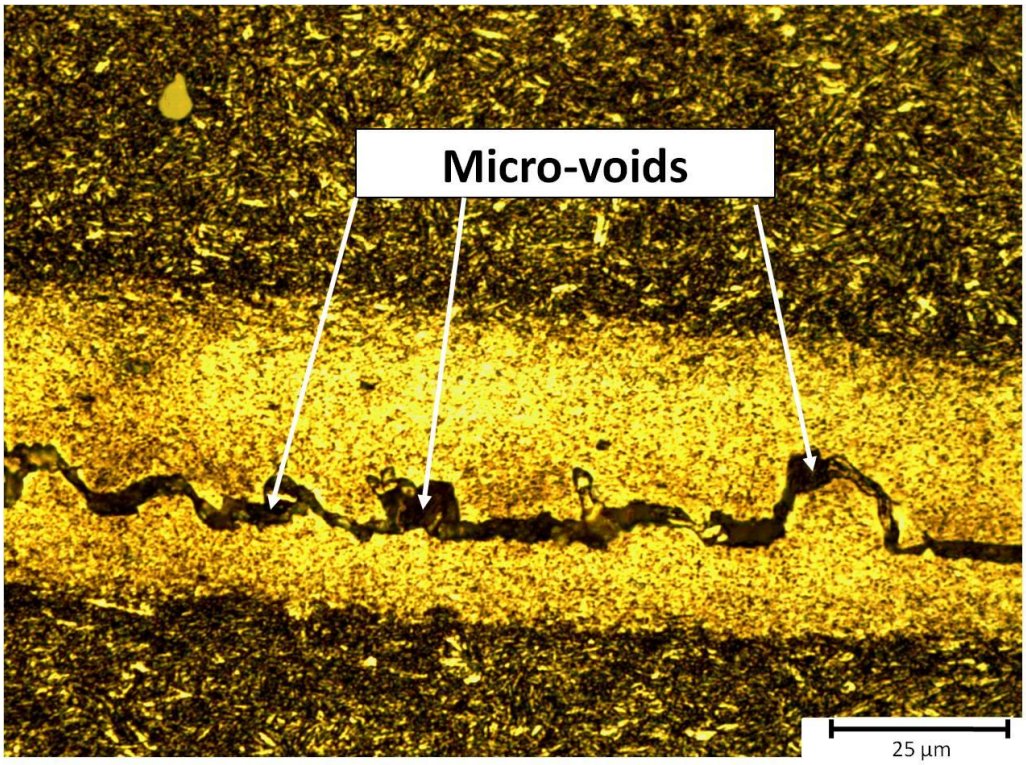

Figure 4.37. Optical micrograph of martensitic AISI 1340 steel, tempered at 315°C, cylindrical specimen, impacted at 42.1 kg.m/s.

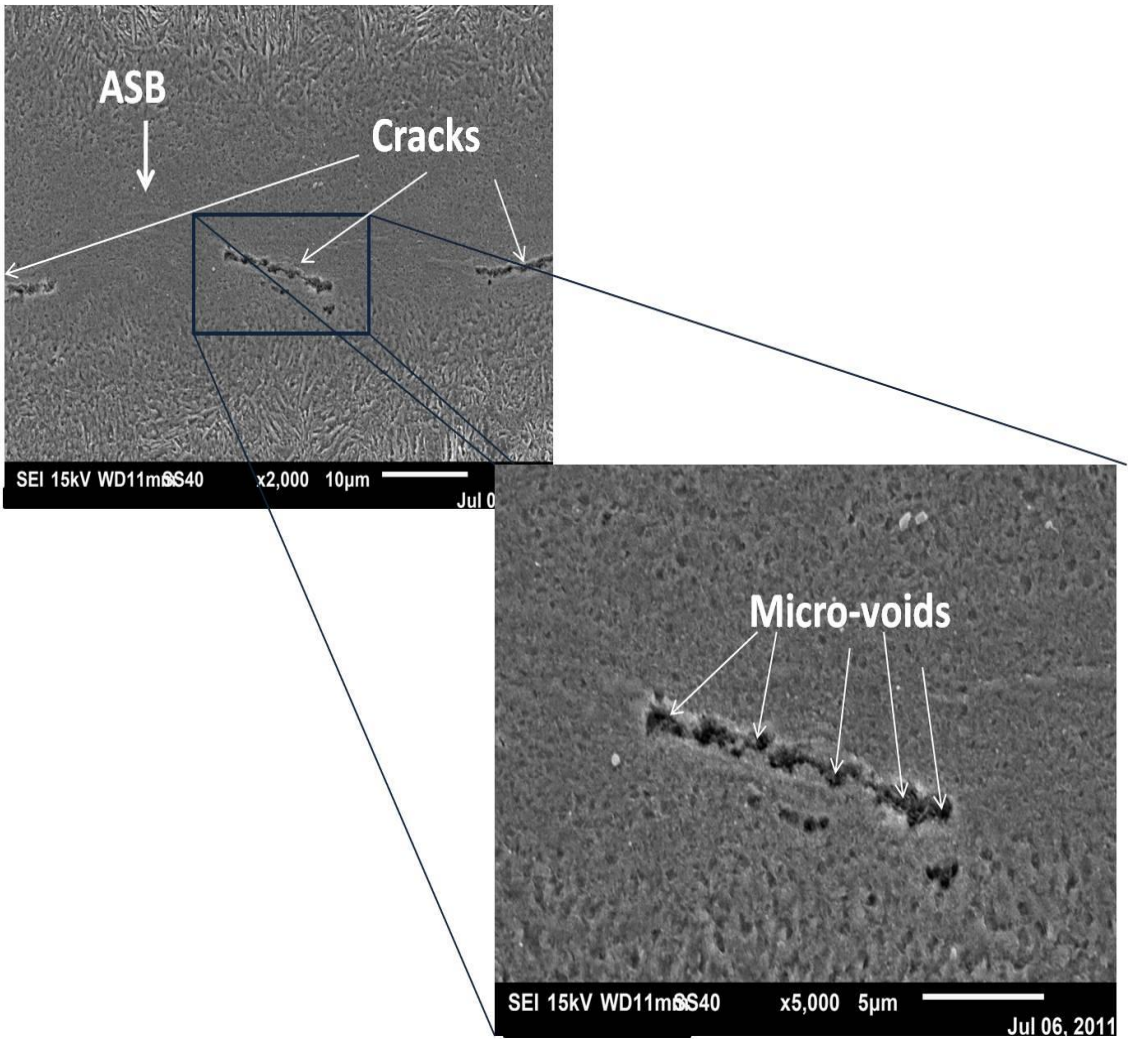

Figure 4.38. SEM micrographs of martensitic AISI 1340 steel, tempered at 315˚C, cylindrical specimen, impacted at 42.1 kg.m/s.

Figure 4.39 shows SEM micrographs of the fracture surface for AISI 1340 steel specimen with dual-phase structure that fractured under impact loading at a momentum of 44.1 kg.m/s. Highly elongated dimples and knobby features are observed on the fracture surface of the adiabatic shear band. Dimples are also observed outside the shear band, which are thicker and have lower aspect ratio than the dimples inside the shear bands. The dimples outside the shear band are shallow, unlike the very deep ones observed inside the shear bands. The highly elongated dimples inside the shear band and adjacent to the shear band region indicate a ductile shear fracture mode along the transformed band and in the adjacent deformed band region. Xue *et al*. [77] studied

adiabatic shear bands in Ti–6Al–4V alloys and proposed a schematic plot for void evolution inside the adiabatic shear bands, as presented in Fig. 2.5. In this schematic view, the voids nucleate inside the shear band as result of tensile stress generated inside the shear band. They grow until they reach the shear band boundary, where the material is harder due to the lower temperature. They proposed that, in the absence of shear stress, these voids grow in an elliptical shape and finally coalescence and generate complete separation. However, in the presence of shear stress, these voids are elongated and rotated [77]. These elongated and rotated dimples are observed as highly elongated dimples on the fracture surface of adiabatic shear band. Odeshi and Bassim [11] also observed dimples on the fracture surface of a high strength low alloy steel specimen that fractured under impact loading. They observed ductile fracture outside the shear band and reported that dimples were nucleated at the surface of the hard particles in the microstructure of bulk material. As shown in Fig. 4.39, a knobby fracture mode was observed on the fracture surface along the adiabatic shear bands, indicating melting of steel in these regions. Therefore, it could be concluded that the temperature rise inside the transformed adiabatic shear bands reach the melting temperature of the alloy in some regions during the dynamic impact loading.

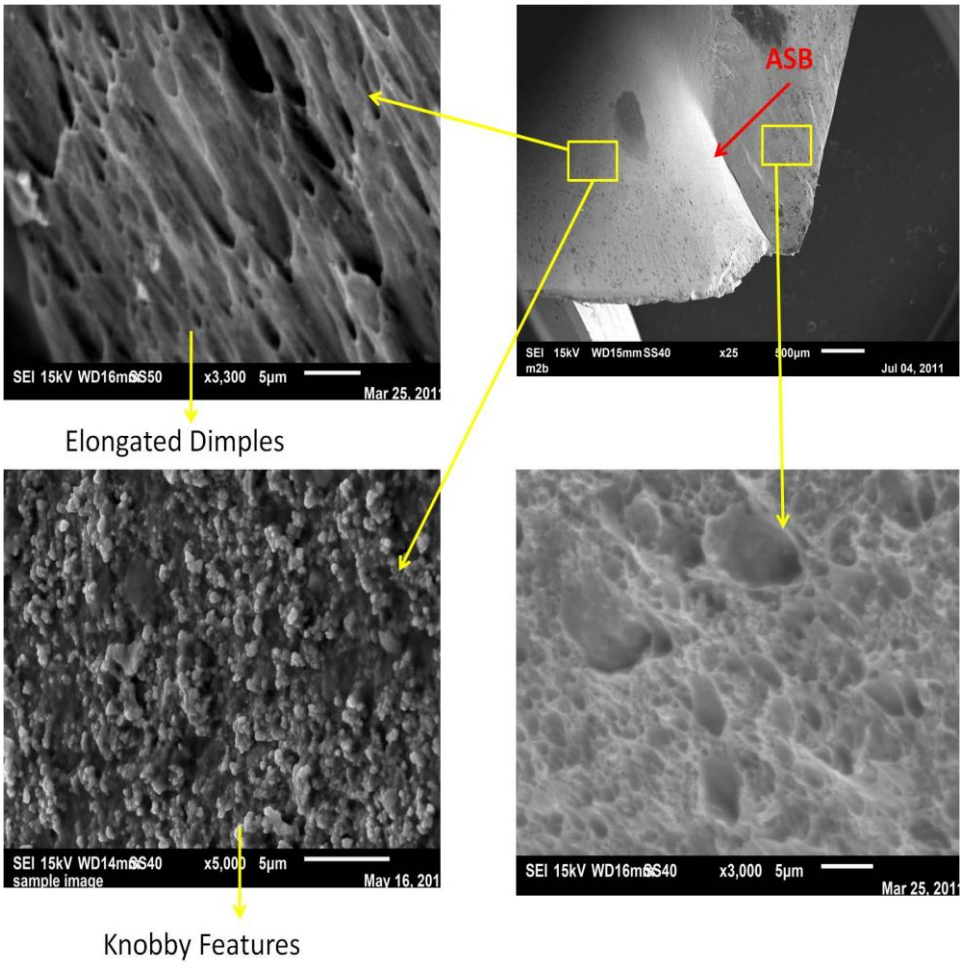

Figure 4.39. SEM micrographs showing the fracture surface of AISI 1340 steel with dual-phase structure (cylindrical specimen).

Lee *et al*. [70] observed dimples on the fracture surface of shear bands of inconel 690 superalloy. They also suggested that these intense dimples show ductile failure. Elongated dimples have been observed in adiabatic bands of other tested materials such as armour steel [31]. They also suggested that knobby features within adiabatic shear bands indicate the melting of an alloy in these regions. Rogers [42] suggested that the knobby features observed on the surface of an adiabatic shear band of a fractured sample is due to frictional heat generated as a result of fracture surfaces rubbing against one another, which causes thermal alteration. Cho *et al.* [13] observed both knobby features and elongated dimples on the fracture surface of an AISI 1018 cold-rolled steel (CRS), a structural steel (HY-100), and an AISI 4340 vacuum arc remelted (VAR) steel tempered to either of two hardnesses RHC 44 or 55. They suggested that the elongated dimples

show a ductile shear fracture mode, while knobby features exhibit melting of the alloy in these regions as a result of heat generation inside the adiabatic shear band as the two fracture surfaces are rubbing against one another.

Both elongated dimples indicating ductile shear failure and a knobby fracture mode were also observed in martensitic AISI 1340 steel that fragmented during impact, irrespective of specimen geometry. For example, Fig 4.40 shows the fracture surface in the shear band region in a fragmented cubical shaped specimen, showing the elongated dimples and knobby features. SEM micrographs of a fractured conical specimen [Fig. 4.41] also show smaller dimples on the fracture surface of the bulk material than dimples on the adiabatic shear band, indicating ductile fracture. Cleavage fracture can also be observed on the fracture surface of the bulk material. Odeshi and Bassim [11] observed both ductile and cleavage fracture on the fracture surface of the bulk material for AISI 4340 steel specimens. They suggested that precipitates open up voids outside the shear band and cause ductile fracture. Therefore, the features of fracture surface of specimens are independent of chemical composition and geometry of the impacted steel specimens. The only difference is in the aspect ratios of the dimples, which are influenced by the extent of thermal softening or degree of plasticity inside the shear band and adjoining regions.

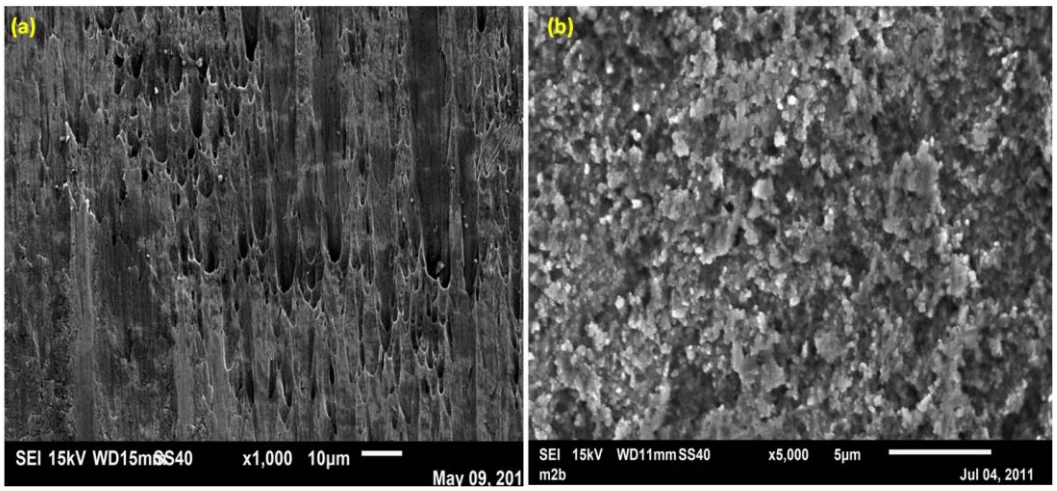

Figure 4.40. SEM micrographs showing the fracture surface of martensitic AISI 1340 steel (cubic specimen), impacted at 38.1 kg.m/s, (a) elongated dimples, (b) knobby features.

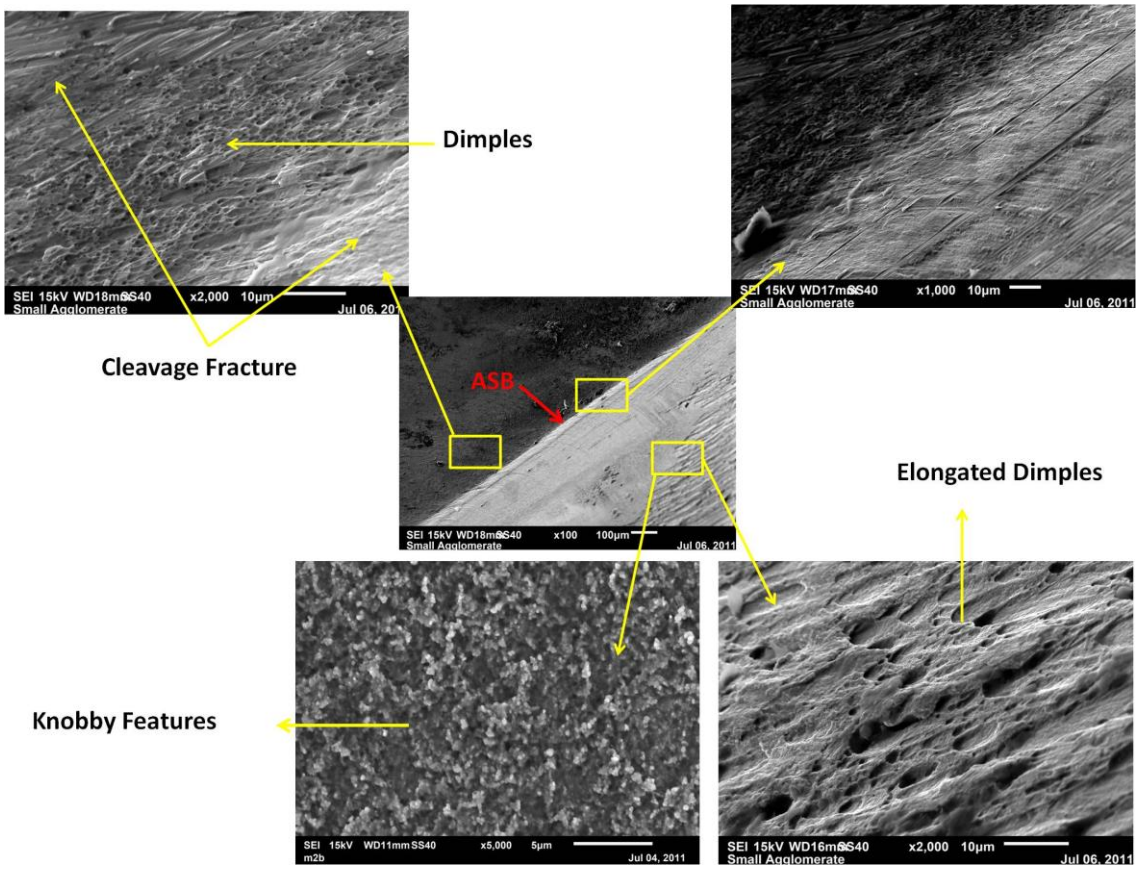

Figure 4.41. SEM micrographs showing fracture surface of martensitic AISI 1340 steel, (conical specimen) impacted at 36.1 kg.m/s.

Figure 4.42 shows the SEM micrographs of the fractured surface of torsional specimens of AISI 4340 steel. Only elongated dimples are observed on the fracture surface. This shows that the temperature rise within the torsional specimen due to adiabatic heating was not high enough to cause melting of the alloy at any point during the high strain-rate torsional loading of the alloy. Evidence of cleavage fracture was also observed on the fracture surface of the torsion specimen, suggesting a combination of ductile shear and cleavage fracture in the alloy under high strain-rate torsional loading.

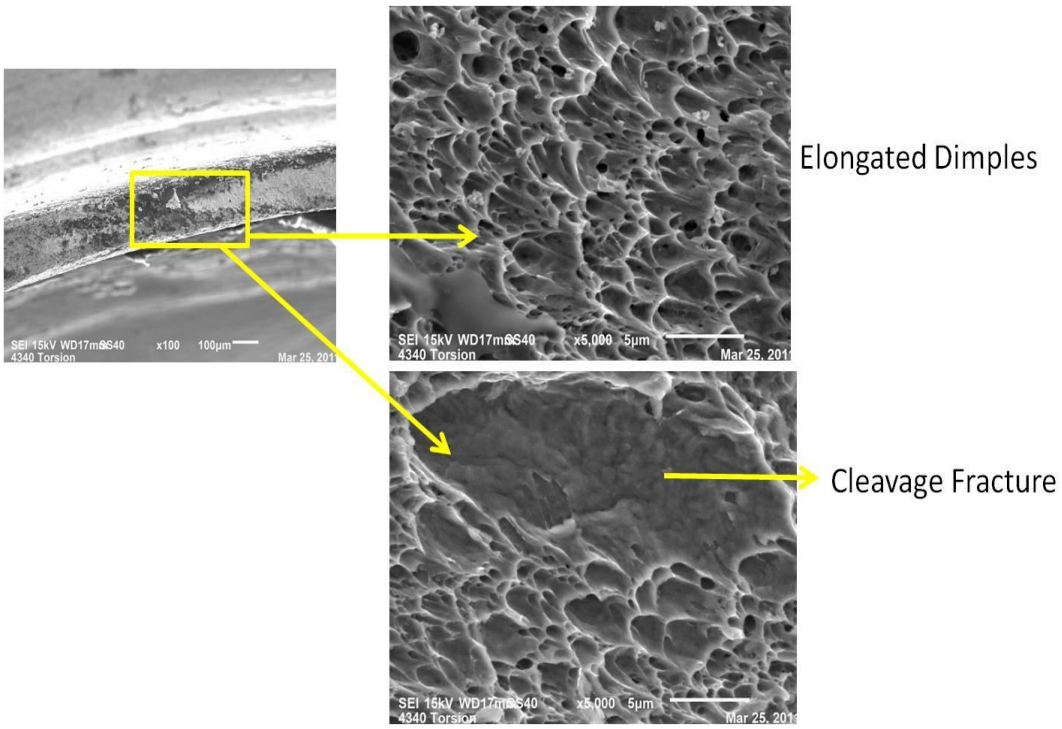

Figure 4.42. SEM micrographs showing fracture surface of martensitic AISI 4340 steel, under high strain-rate torsion loading.

Figure 4.43 shows the optical micrograph of a longitudinal section of a martensitic AISI 1340 cubic specimen that fragmented under impact loading. The specimen was sectioned perpendicularly across the fracture surface. Three separate regions can be recognised under the fracture surface: white etching adiabatic shear band (transformed adiabatic shear band) on the fracture surface, deformed band showing alignment of martensite plates and laths along shear direction below the white band layer and the bulk

materials outside the shear band region. The high intensity of shear strain inside the white etching adiabatic shear band caused the martensite to fragment into submicron size grains which could not be detected by optical microscopy (Region1).

The thermal softening and shear stress in the second region cause the alignment of martensite plates in shear flow direction indicated by the two arrows in Fig. 4.43 just below the transformed band on the fracture surface. In region 3 which comprises the region outside the shear band, i.e. the bulk material, the material just underwent normal strain hardening and there was no change in microstructure compared to that of the specimen before impact. This shows that the shear band region consists of a transformed band surrounded by a deformed band having a lamellar structure.

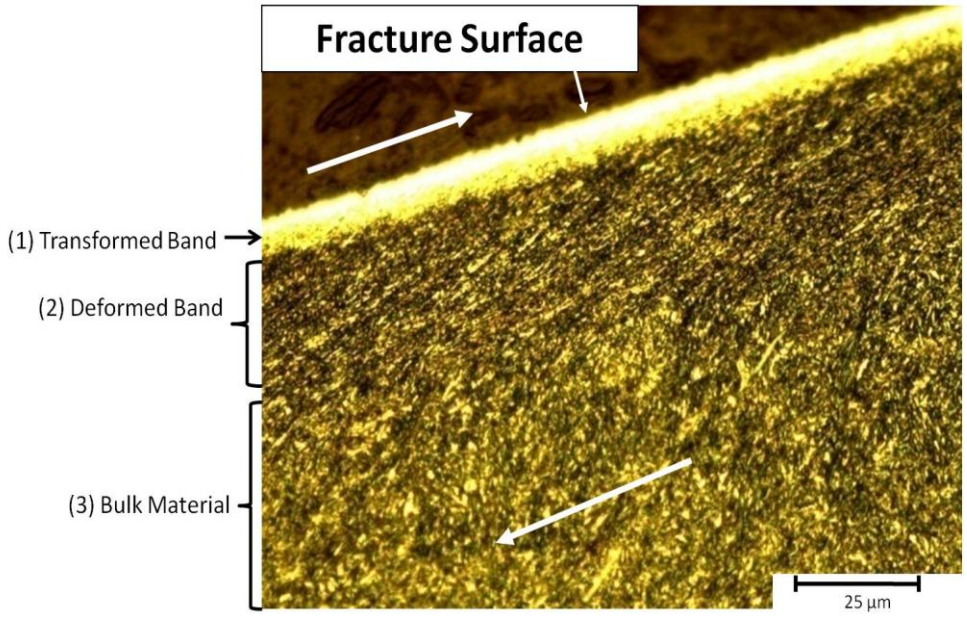

Figure 4.43. Optical micrograph showing longitudinal section of fracture cubical specimen of martensitic AISI 1340 steel.

Li *et al*. [43] also observed fine equi-axed subgrains with an average diameter of 150 nm, as well as low density of dislocations at the centre of the adiabatic shear band as a result of dynamic recrystallization They also observed the lamellae structure with elongated grains in a transition region between the centre of the shear band and the matrix. TEM investigation of dynamic deformation in 8090 Al–Li alloy by Xu *et al.* [33] showed that the material outside the adiabatic shear band consists of deformed cells

with a high density of dislocations, while the deformed region between the matrix and shear band consists of highly elongated cells with well defined boundaries. On the other hand, the structure inside the shear band consists of very fine equi-axed subgrains with a low density of dislocations with a size of about 0.2 μm. They suggested that these equi-axed subgrains are formed as a result of dynamic recrystallization.

Figures 4.44 - 4.46 show the optical macrographs of fractured cylindrical, cubical, and conical AISI 4340 steel specimens. These pictures were taken using a stereomicroscope. Based on the geometry of these fractured specimens and the three dimensional model for geometry of the adiabatic shear band in the various impacted specimen shown earlier (Fig. 4.35) , a schematic representation of crack propagation leading to fragmentation is proposed as shown in Fig. 4.47. Cracks initiate inside the shear bands and propagate into the bulk materials and connect with the second conical or pyramidal shape adiabatic shear band for cylindrical and cubical shaped specimens, respectively. The specimens eventually fragment into two symmetrical parts, as shown in Fig. 4.44 and 4.45. For the conical specimen, the crack initiates from the corner of the cone formed on the smaller side of the cone. It propagates along the adiabatic shear band to the lower point of the cone and then through bulk material in the shear band free zone into the other end of the truncated cone with bigger diameter, as shown in Fig. 4.46.

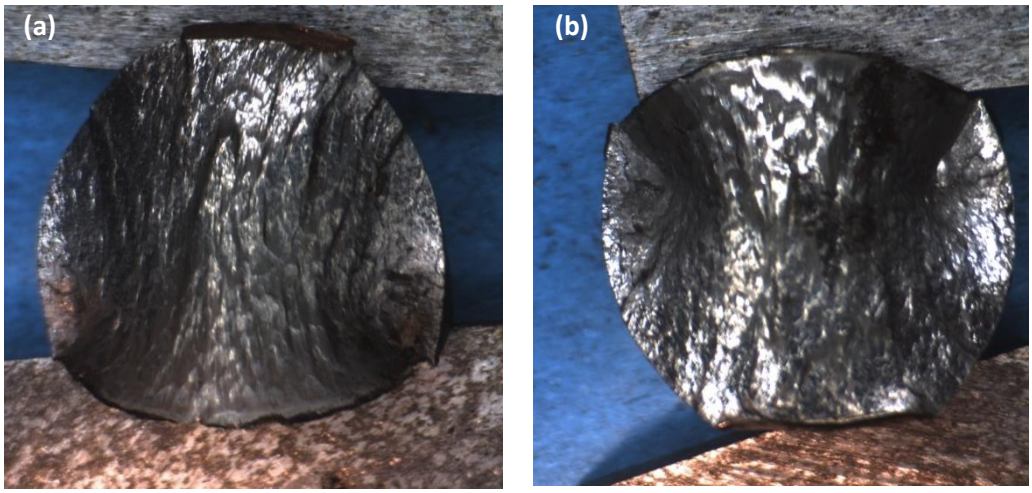

Figure 4.44. Optical macrographs of fractured cylindrical specimen of martensitic AISI 4340 steel.

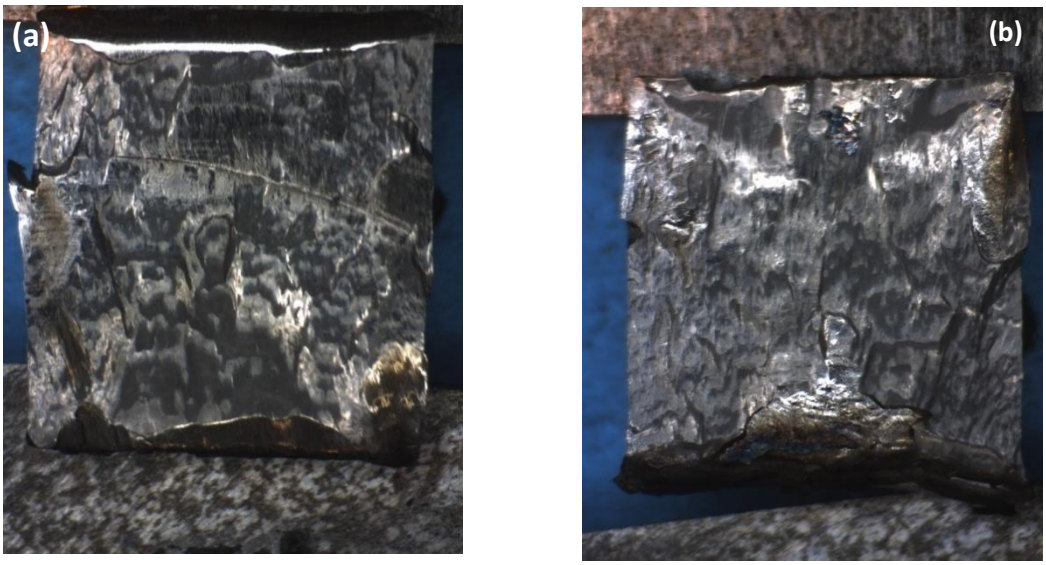

Figure 4.45. Optical macrographs of fractured cubical specimen of martensitic AISI 4340 steel.

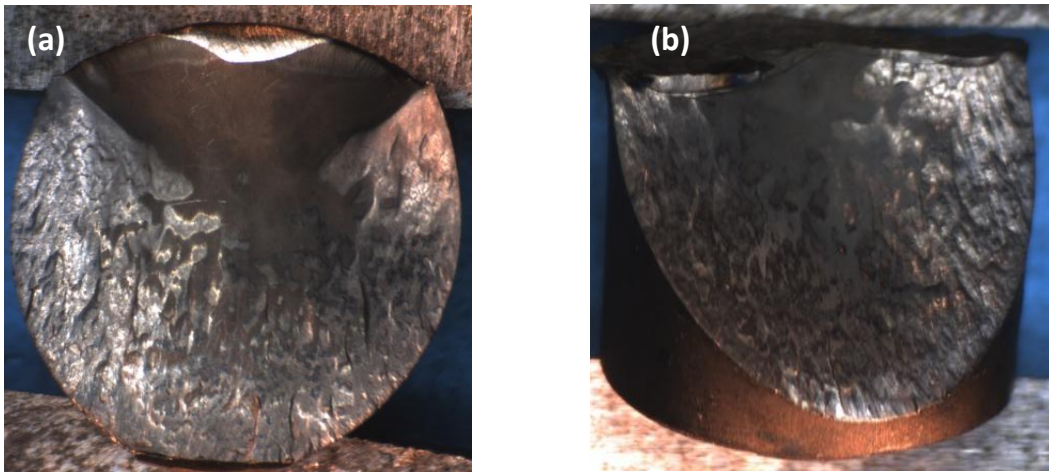

Figure 4.46. Optical macrographs of fractured conical specimen of martensitic AISI 4340 alloy steel.

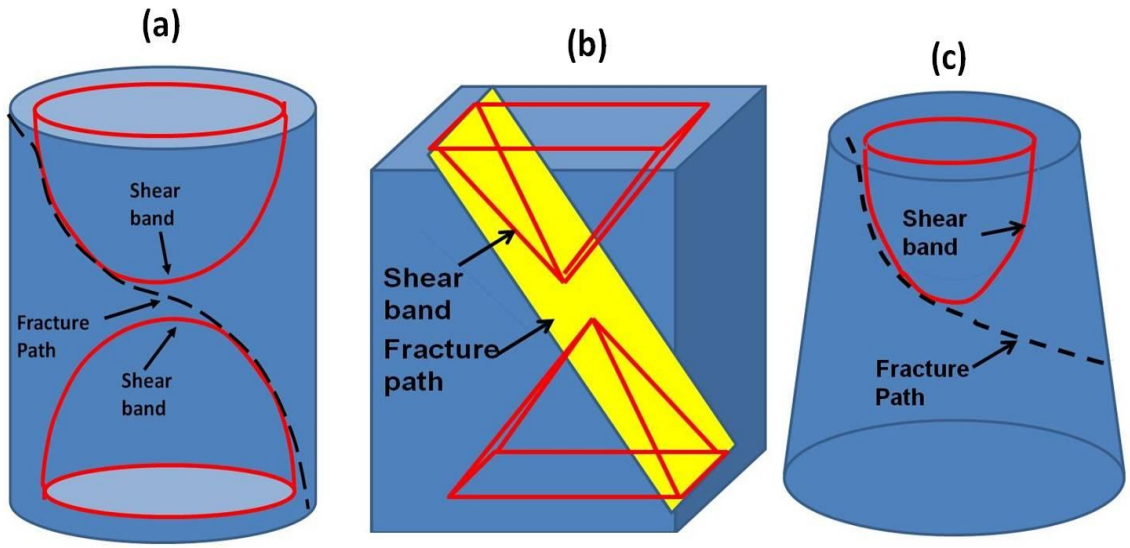

Figure 4.47. Schematic view of crack propagation path, (a) cylindrical, (b) cubical, (c) conical Specimens.

4.4. X-ray photoemission electron microscopy (XPEEM)

The results of the investigation of the transformed band in AISI 4340 steel using X-ray photoemission electron microscopy (XPEEM) and Near Edge X-Ray Absorption Fine Structure (NEXAFS) spectroscopy (Fig. 4.48-4.50) suggest redistribution of alloying elements promoted by the intense adiabatic heating and large strain in the shear band region during impact. Whereas more Nickel was observed inside the shear bands than outside, less chromium was observed inside the shear bands than in the adjacent region. Figure 4.49 shows the PEEM images of the adiabatic shear band in an AISI 4340 steel specimen while Fig. 4.50 shows the Ni map inside and outside of the adiabatic shear band in the specimen. It is evident that there is more nickel inside the shear band than outside. During high strain rate deformation, the temperature rises inside the material. This temperature rise inside the material depends on the chemical composition, microstructure, and strain rate. Chen *et al*. [62] suggested that, depending on the thickness of a target material, the temperature can rise up to 1527˚C inside the adiabatic shear band of the target material. This high temperature inside the shear band, coupled with high strain, may promote the atomic diffusion of Ni and Cr inside the shear band. The reason for the observed direction of atom migration across the shear band boundary

is not very clear at the moment. The XPEEM and NEXAFS were conducted at the Soft X-ray Spectromicroscopy (SM) beamline at the Canadian Light Source (CLS) using synchrotron light radiations.

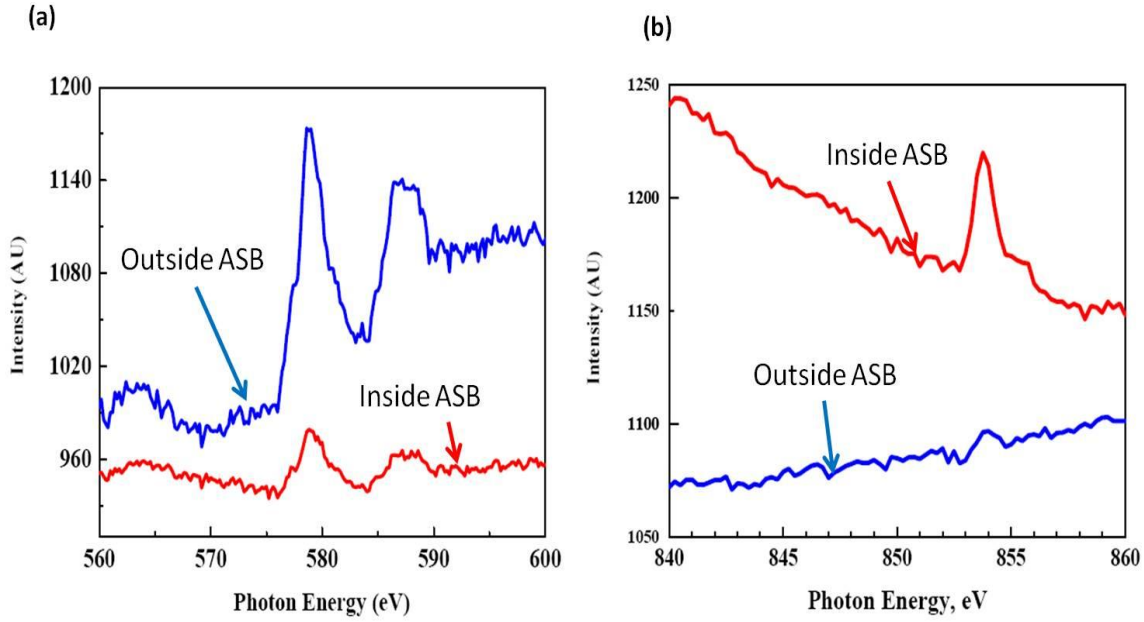

Figure 4.48. (a) Cr 2p-3d NEXAFS spectra from inside and outside the shear band, (b) Ni 2p-3d NEXAFS spectra from inside and outside the shear band.

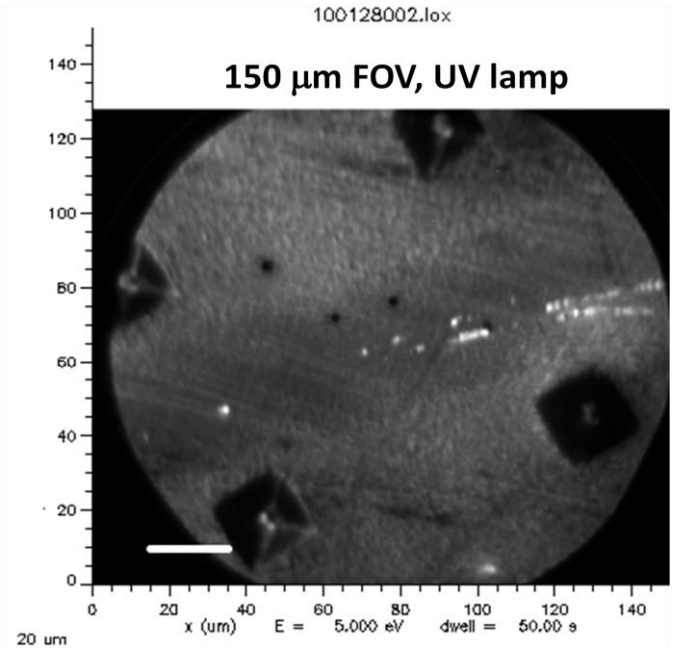

Figure 4.49. PEEM imaging using Hg lamp, 150µm FOV.

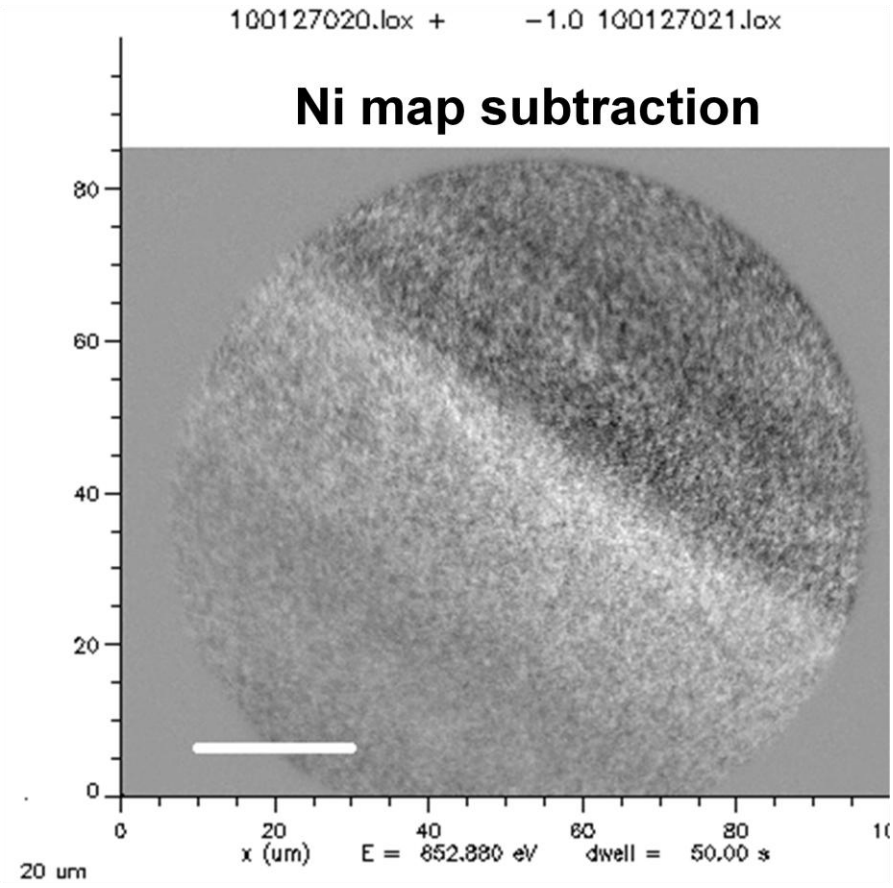

Figure 4.50. XPEEM Image showing nickel map using synchrotron light radiation.

4.3. Microhardness results

4.3.1. Hardness values across the shear band

Figure 4.51 shows the Vickers hardness values across the shear band of a martensitic AISI 1340 alloy steel specimen that was tempered at 315˚C and then impacted at the impact momentum of 39.1 kg.m/s. The error bars indicate confidence intervals with the confidence level of 90%. The hardness value increases from the edge of the specimen and reaches the maximum value at the centre of the shear band. Then it decreases and become relatively constant. The higher hardness inside shear bands can be attributed to the change in microstructure inside the shear band, especially grain refinement and increased dislocation density as outlined in some previous studies [13, 26, 42, 67, 70].

Increased dislocation density inside the shear bands can be one of the contributing factors to the higher hardness of shear bands compared with the rest of the material. Lee *et al*. [70] observed dislocation and twinning deformation inside the shear band. Their TEM investigation exhibited the nucleation of ά martensite and existence of a high proportion of dislocations inside the shear band of the deformed 304L stainless steel. Dislocations are arranged in a form of dislocation tangle which causes dislocation cell wall formation. Meyers and Wittman [26] suggested that higher hardness of ASB in low-carbon steels (AISI 1018 and 8620) is due to the fine microstructure with supersaturated carbon and not a phase transformation. Chen *et al*. [14] suggested that carbide lamellae spheroidization occurs inside the adiabatic shear band as a result of the fragmentation of carbide laths. Moreover, very fine ferrite subgrains form inside the shear band due to the iron diffusion path under hydrostatic pressure and high temperatures [14]. Rogers [42] observed that the adiabatic shear band consists of submicron size grains with the average size of tens of micrometers. TEM investigation of the white etching band in a TC4 alloy showed the existence of equi-axed grains with the diameter of 50 nm inside the shear band [44]. Li *et al*. [43] observed fine equi-axed subgrains with the average diameter of 150 nm, in the adiabatic shear band for Monel alloy. Meyers and Pak [30] observed small grains with the average size of 0.3-0.5 μm inside the shear band of titanium. There have been also fine equi-axed submicron size grains inside the shear band of tantalum [15]. For Copper samples that were deformed

under dynamic shock loadings, the submicron size grains with the average size of 0.1μm were observed inside the adiabatic shear band [35, 36]. Therefore finer grain size as well as formation of microstructure containing supersaturated carbon account for the observed higher hardness values inside the shear band of the investigated steel.

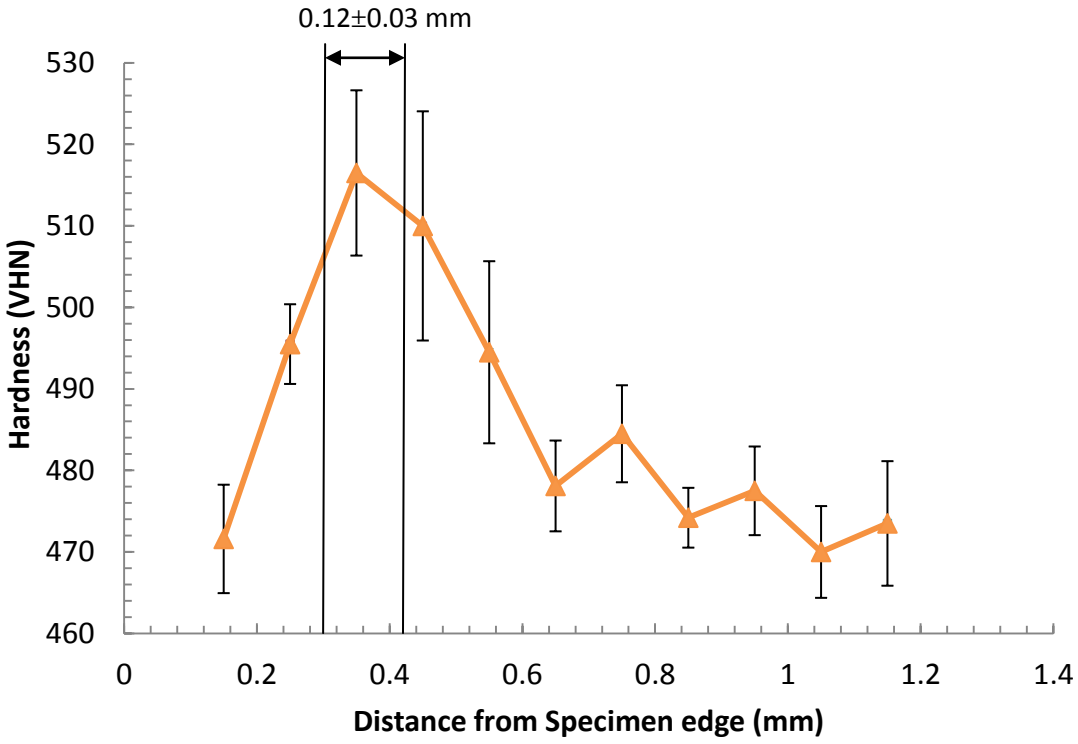

Figure 4.51. Vickers hardness value across adiabatic shear band of martensitic AISI 1340 steel, tempered at 315°C, cylindrical specimen, impacted at 39.1 kg.m/s.

4.3.2. The effect of microstructure on hardness values

The Vickers hardness values for the original heat treated specimens before the impact test are shown in Fig. 4.52. The error bars show confidence intervals with the confidence level of 90%. For martensitic specimens, as the tempering temperature increases, more of the stress which may be introduced inside the steel during rapid cooling is relieved. Therefore, hardness value of the pre-impact martensitic specimen which was tempered at 205˚C is 4.5 % higher than that for pre-impact martensitic specimen which was tempered at 315˚C. The hardness values of martensitic specimens and the dual-phase structure specimen are close to each other. Both were tempered at the same temperature and the one with the dual-phase structure contains a low fraction of ferrite (20 % vol.). Therefore, the probability that the micro indentation will be located on the martensitic structure during the hardness test is about four out of five. This explains why the hardness of the AISI 1340 steel heat-treated to have dual-phase structure has the same range of hardness with those that have martensitic structure. The steel specimens with pearlitic structure have the lowest hardness. Pre-impact hardness value of the pearlitic specimen is approximately half of that for martensitic specimen tempered at 315˚C. The martensitic structure is formed when the austenitized steel specimens are rapidly quenched to room temperature. The cooling rate is high enough to prevent carbon diffusion. These carbon atoms stay in martensitic structure as interstitial impurities, which effectively hinder dislocation motions. Moreover, martensitic structure has body-centered tetragonal (BCT) structure. BCT structure has relatively low slip systems along which dislocations can move [89].

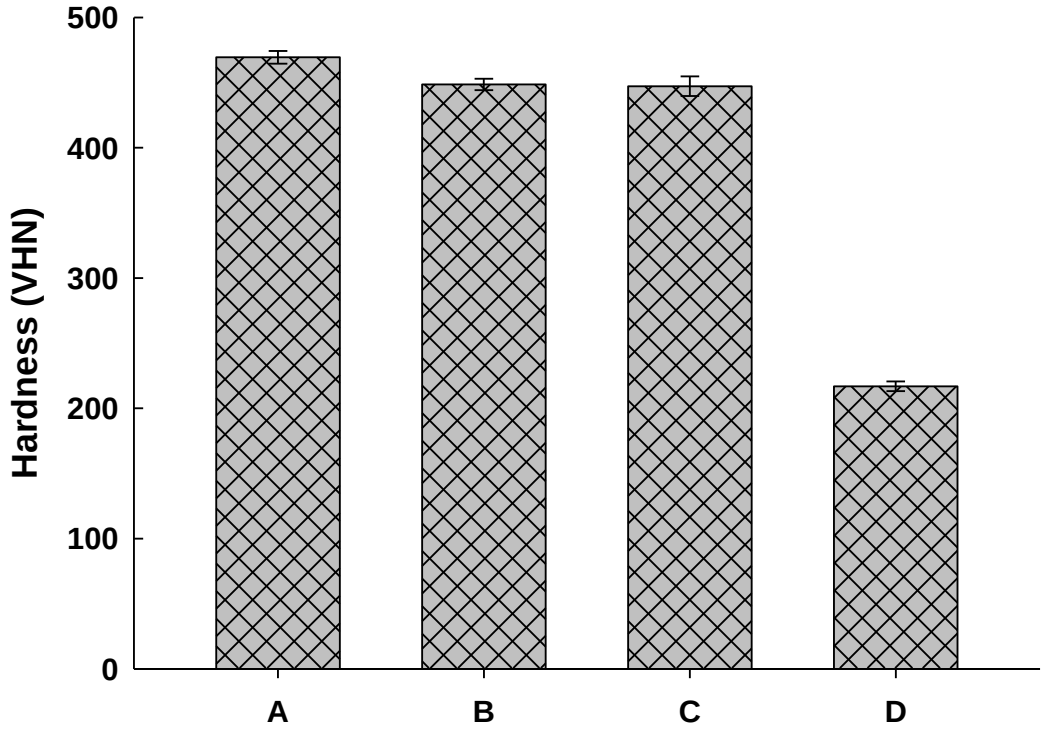

Figure 4.52. Vickers hardness values for AISI 1340 steel before impact loading, (A) martensitic, tempered at 205˚C (B) martensitic, tempered at 315˚C, (C) dual-phase structure, tempered at 315˚C, (D) pearlitic structure.

Figure 4.53 shows the results of hardness measurement inside and outside the shear bands for various AISI 1340 steel specimens (with different microstructures) impacted at a momentum of 36.1 kg.m/s. The error bars are showing confidence intervals with the confidence level of 90%. The hardness value inside the shear band of the martensitic specimen tempered at 205˚C is 28% higher than that for the pre-impact specimen, while the hardness value inside the shear band of the martensitic specimen tempered at 315˚C is 17% higher than that for pre-impact specimen. The higher amount of initial perturbation for the specimen tempered at 205˚C motivates higher a intensity of shear strain localization in this specimen, which can lead to a higher density of dislocations and finer microstructure inside the shear band. The hardness value outside of the shear band for the specimen which was tempered at 205˚C is 18% higher than the pre-impact

hardness value for the same specimen, while the hardness value outside of the specimen that was tempered at 315˚C is 16% higher than the pre-impact hardness value. Materials outside the shear band undergo strain hardening as a result of high strain-rate deformation. Therefore, hardness outside the shear band is greater than hardness values for the pre-impact specimens.

For the pearlitic steel specimens, the hardness value inside the shear band is 34% higher than that for the pre-impact specimen. The hardness value outside the shear band of the pearlitic specimen is 25% higher than that for the pre-impact specimen. This demonstrated that materials inside and outside the shear band undergo significant amounts of plastic deformation. The SEM micrographs of the impacted pearlitic specimen show that pearlite and ferrite grains are smaller inside the shear band than outside. Therefore, a higher hardness value inside the shear band than outside is due to the finer nature of pearlite and ferrite grains inside the shear band and to higher strain hardening inside the bands.

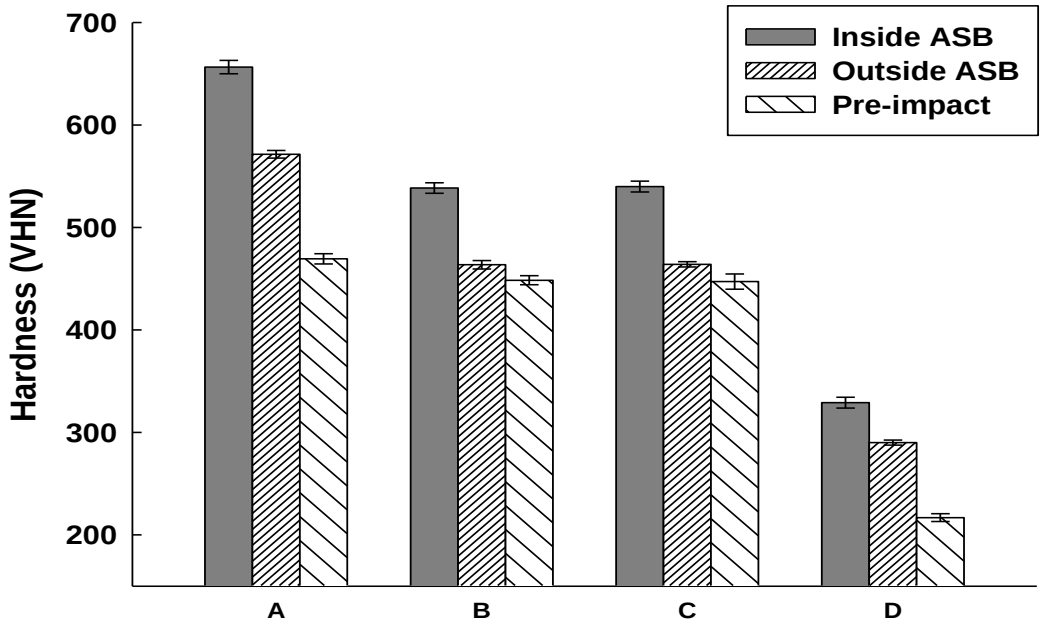

Figure 4.53. Vickers Hardness values for AISI 1340 steel, Impacted at 36.1 kg.m/s, (A) martensitic, tempered at 205˚C, (B) martensitic, tempered at 315˚C, (C) dual-phase structure-tempered at 315˚C, (D) pearlitic structure.

4.3.3. The effect of impact momentum on hardness value

Figure 4.54 shows the effect of an increase in impact momentum on the hardness measurements inside and outside shear bands in martensitic AISI 1340 steel specimens that were tempered at 315˚C. The error bars show confidence intervals with the confidence level of 90%. As the impact momentum was increased from 34.2 kg.m/s to 39.1 kg.m/s, the hardness values both inside and outside of the shear bands also increased. However, while only a marginal increase of 2% in the hardness was recorded for the region outside the shear band, the hardness increase for the shear band region was higher (5%). The hardness values inside and outside of the shear band for the martensitic specimen that was impacted at 34.2 kg.m/s are respectively 15% and 4% higher than the original hardness of the specimens before impact test. On the other hand, the hardness value inside the shear band for the martensitic specimen that was impacted at 39.1 kg.m/s was 19% higher than that for pre-impact specimens, while the hardness value outside the shear band is 6% higher than that for the pre-impact specimen. As the impact momentum increases, the material outside the shear band undergoes an increased amount of work hardening. As the impact momentum increases, the amount of heat generated inside the shear band increases. Therefore, the temperature rise within the adiabatic shear band increases as the impact momentum increases. This will translate into a more intense thermal softening and localised deformation at higher impact momentum.

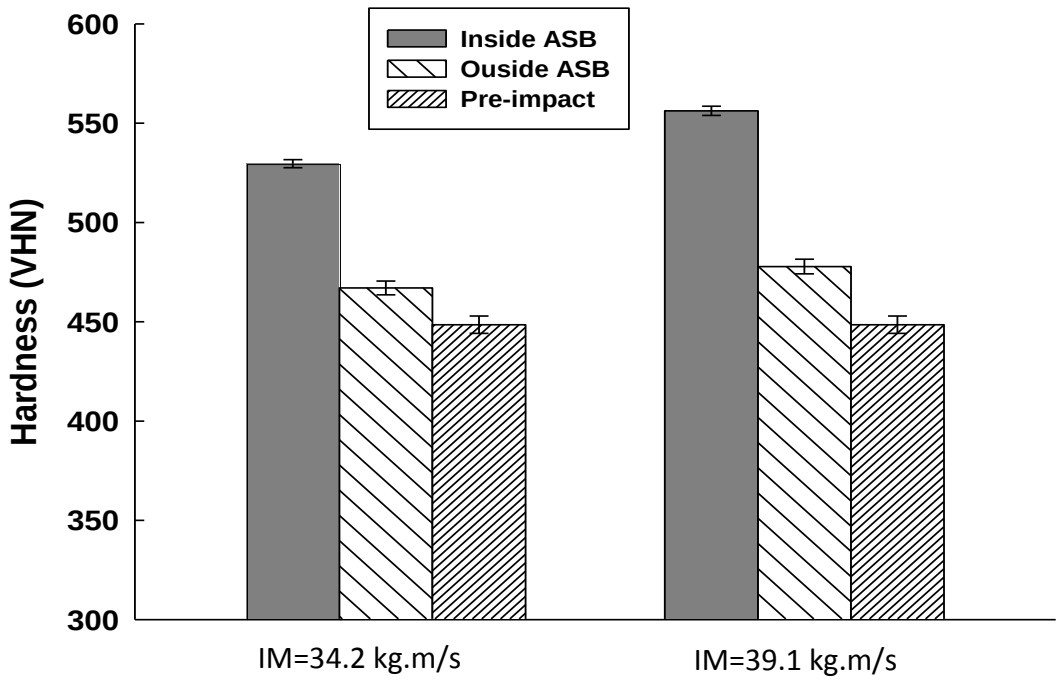

Figure 4.54. Vickers hardness values for martensitic AISI 1340 steel as a function of impact momentum (IM).

CHAPTER FIVE

CONCLUSIONS AND RECOMMENDATIONS

5.1. Conclusions

The effects of microstructure, strain rates and geometry on plastic deformation and failure of AISI 4340 and 1340 steel under high strain-rate loading both in torsion and in compression were investigated. The results of this study show that:

1. Failure of both alloys under dynamic loading in torsion and compression was initiated by intense shear strain localization along adiabatic shear bands. Both deformed and transformed bands were observed in the alloys depending on the microstructure and impact momentum or strain rate.

2. Formation of deformed and transformed adiabatic shear bands occurred in different stages of deformation. A deformed band formed at low strain rates when the localized shear strains were only high enough to align grains along the shear flow direction. As the strain rate increased, transformed adiabatic shear bands formed which contained fine equi-axed grains of submicron size.

3. The specimens with a martensitic structure were more inclined to form transformed shear bands that those having a pearlitic structure. The higher the tempering temperature of the martensitic steel, the lower its tendency to form an adiabatic shear band under dynamic shock loading.
4. AISI 4340 steel was more susceptible to adiabatic shear failure than AISI 1340 steel and there was a noticeable correlation between the dynamic stress-strain curves of both alloys and the microstructural evolution associated with adiabatic shear banding in the alloys.
5. The trajectory of the shear bands along the transverse section of impacted cylindrical-, cubical-, and conical-shaped specimens followed the shape of the

cross-section. While circular-shape shear bands were observed in cylindrical specimens, the shear bands in cubic-shape specimens formed a rectangular path. The impacted conical-shaped specimens showed circular-shape shear bands on the smaller transverse-cross sectional area, and no evidence of a shear band on the larger transverse cross-sectional area at the base of the cone.

6. The overall shape of the adiabatic shear bands in cylindrical-shape specimens was two cones which were mirror images of one another, while in cubic-shape specimens, two pyramids that were also mirror images of one another formed. The shear band in conical-shaped specimens was a cone facing the smaller diametrical surface of the specimen.

7. The alloys fragmented by ductile shear failure along the adiabatic shear bands. Fractographic investigations of the fragmented specimens showed both ductile shear and knobby fracture modes along the transformed shear band region. The presence of a knobby fracture mode indicates that the temperature rise inside the shear band during impact was close to the melting point of the steel inside the transformed band. All the fracture surfaces of fragmented cylindrical-, cubical-, and conical-shaped specimens showed both ductile shear failure and knobby fracture modes.

8. The deformed band adjacent to the transformed band also failed by ductile shear failure. The elongated dimples in the transformed band region were much deeper than those in the adjacent deformed band. This confirms a higher level of plasticity in the transformed band.

9. Hardness values of the transformed adiabatic shear bands were higher than that of the bulk materials outside the shear band region due to the extremely fine structure of these bands. The proportion of hardness increase inside the shear band over the hardness of the bulk materials outside the shear band depended on the pre-impact microstructure.
10. X-ray Photoemission electron microscopic (XPEEM) investigation of the transformed band in AISI 4340 steel suggests the occurrence of strain-enhanced

atomic diffusion inside the bands as a result in the intense localised adiabatic heating and high strain intensity. More nickel and less chromium were recorded inside the transformed shear band than in the region outside the transformed band.

5.2. Limitations and strength of thesis

To study the effects of microstructure, AISI 1340 and AISI 4340 cylindrical and thin-walled tubular steel specimens were heat treated to provide martensitic, pearlitic, and dual-phase structures. The number of specimens in each category was limited. In order to investigate the effect of strain rate on the behaviour of AISI 1340 and 4340, specimens have to be subjected to different strain rates. Therefore, each test with specific conditions was conducted once, which is a limitation on the stress strain values reported. However, at this stage of the research, the primary interest was in the general trends of the dynamic stress-strain curves as affected by impact momentums and microstructure.

The transformed band observed in AISI 1340 steel could not be investigated using X-ray Photoemission Electron Microscopy (XPEEM) and Near Edge X-ray Absorption Fine structure (NEXAFS) spectroscopy because of a prolonged equipment breakdown. At the time of writing this thesis, the PEEM beamline is still not fully operational at the CLS.

The effects of geometry of the specimen on the morphology and properties of the adiabatic shear band has been also studied in this research for AISI 1340 and 4340 steel, which is a new subject of study. There has been no such previous work on chemical analysis of the transformed band in these alloys. The chemical analysis of the material inside and outside the shear band using X-ray Photoemission Electron Microscope (XPEEM) and Near Edge X-ray Absorption Fine structure (NEXAFS) spectroscopy is a new approach to understanding the microstructure evolution associated with the occurrence of transformed bands in steel. The new results of XPEEM and NEXAFS were presented at the 7^{th} International workshop in LEEM-PEEM on August 8-13, 2010 in New York, and also at Pipeline Materials Reliability Workshop for a NSERC Strategic Network on April 8, 2011 in Calgary.

5.3. Recommendation for future works

The recommendations for future works are as follows:

1. Transmission Electron Microscopy (TEM) investigations to provide more detailed information on the evolution of microstructure in transformed bands formed in the two alloys as a function of the investigated heat treatment condition,

2. X-ray Photoemission microscopic (XPEEM) investigation of transformed band in AISI 1340 steel specimen, and

3. In-situ investigation of composition changes inside adiabatic shear band with increasing temperature using synchrotron light radiation (XPEEM, and NEXAFS) at the Canadian Light Source.

REFERENCES

[1] A. K. Zurek, "The Study of Adiabatic Shear Band Instability in a Pearlitic 4340 Steel Using a Dynamic Punch Test", *Metallurgical and Materials Transactions* 25A (1994) 2483-2489.

[2] S.E. Schoenfeld, T.W. Wright, "A failure criterion based on material instability", *International Journal of Solids and Structures* 40 (2003) 3021–3037.

[3] C. Zener, J. H. Hollomon, "Effect of Strain Rate Upon Plastic Flow of Steel", *Journal of Applied Physics* 15 (1944) 22-32.

[4] M. N. Raftenberg, C. D. Krause, "Metallographic observation of Armor Steel specimens from plates perforated by shaped charge jets", *International Journal of Impact Engineering* 23 (1999) 757-770.

[5] X.W. Chena, Q.M. Lib, S.C. Fan, "Initiation of adiabatic shear failure in a clamped circular plate struck by a blunt projectile", *International Journal of Impact Engineering* 31 (2005) 877–893.

[6] V. F. Nesterenko, M. A. Meyers, T. W. Wright, "Self-Organization in the initiation of adiabatic shear bands", *Acta Materialia* 46 (1998) 327-340.

[7] S. N. Medyanik, W. K. Liu, S. Li, "On criteria for dynamic adiabatic shear band propagation", *Journal of the Mechanics and Physics of Solids* 55 (2007) 1439–1461.

[8] B. Zhang, W. Shen, Y. Liu, R. Zhang, "Some factors influencing adiabatic shear banding in impact wear", *Wear* 214 (1981) 259—263.

[9] L. Daridon, O. Oussouaddi, S. Ahzi, "Influence of the material constitutive models on the adiabatic shear band spacing. MTS, power law and Johnson–Cook models", *International Journal of Solids and Structures* 41 (2004) 3109–3124.

[10] M.R. Staker, "Relation between adiabatic shear instability strain and material properties", *Acta Metallurgica* 29 (1981) 683–689.

[11] A.G. Odeshi, M.N. Bassim, "High strain-rate fracture and failure of a high strength low alloy steel in compression", *Materials Science and Engineering* A525 (2009) 96–101.

[12] J. Duffy, Y.C.Chi, "On the measurement of local strain and temperature during the formation of adiabatic shear bands", *Materials Science and Engineering A* 157 (1992) 195–210.

[13] K.M. Cho, S. Lee, S.R. Nutt, J. Duffy, "Adiabatic shear band formation during dynamic torsional deformation of an HY-100 steel", *Acta Metallurgica et Materialia* 41 (1993) 923–932.

[14] Z.H. Chen, L.C. Chan, T.C. Lee, C.Y. Tang, "An investigation on the formation and propagation of shear band in fine-blanking process", *Journal of Materials Processing Technology* 138 (2003) 610–614.

[15] M.A. Meyers, Y.J. Chen, F.D.S. Marquis, D.S. Kim, "High-Strain-Rate Behavior of Tantalum", *Metallurgical Transactions* 26A (1995) 2493- 2509.

[16] A. Hartley, J. Duffy, R.H. Hawley, "Measurement of the temperature profile during shear band formation in steels deforming at high strain rates", *Journal of Mechanics and Physics of Solids* 35 (1987) 283-301.

[17] C.O. Mgbokwere, S.R. Nutt, J. Duffy, "Shear band formation in 4340 steel: a TEM study", *Mechanics of Materials* 17 (1994) 97–110.

[18] M. Zhou, A. J. Rosakis, G. Ravichandran, "Dynamically Propagating Shear Bands in Impact-Loaded Pre-notched Plates I. Experimental Investigations of Temperature Signatures and Propagation Speed*", Journal of the Mechanics and Physics of Solids* 44 (1996) 981-1006.

[19] B.K. Kad, J.M. Gebert, M.T. Perez-Prado, M.E. Kassner, M.A. Meyers, "Ultrafine-grain-sized zirconium by dynamic deformation", *Acta Materialia* 54 (2006) 4111–4127.

[20] C.L. Wittman, M.A. Meyeres, H.R. Pak, “Observation of an Adiabatic Shear Band in AISI 4340 Steel by High-Voltage Transmission Electron Microscopy”, *Metallurgical Transactions* 21A (1990) 707-716.

[21] A.G. Odeshi, M.N. Bassim, S. Al-Ameeri, “Effect of heat treatment on adiabatic shear bands in a high-strength low alloy steel”, *Materials Science and Engineering A* 419 (2006) 69–75.

[22] T.C. Lee, L.C. Chan, B.J. Wu, “Straining behaviour in blanking process—fine blanking vs. conventional blanking”, *Journal of Materials Processing and Technology* 48 (1995) 105–111.

[23] Q. Xue, G.T. Gray, “Development of adiabatic shear bands in annealed 316L stainless steel. Part II. TEM studies of the evolution of microstructure during deformation localization”, *Metallurgy and Materials Transaction* 37A (2006) 2447–2458.

[24] H. Feng, M.N. Bassim , “Finite element modeling of the formation of adiabatic shear bands in AISI 4340 steel”, *Materials Science and Engineering* A266 (1999) 255–260.

[25] K.C. Dao, D.A. Schockey, “A method for measuring shear-band temperatures”, *Journal of Applied Physics* 50 (1979) 8244-8246.

[26] M.A. Meyers, C.L. Wittman, “Effect of metallurgical parameters on shear band formation in low-carbon (approx. 0.20 wt pct) steels”, *Metallurgical Transactions* 21A (1990), 3153–3164.

[27] S.P. Timothy, “The structure of adiabatic shear bands in metals: A critical review”, *Acta Metallurgica* 35 (1987) 301-306.

[28] J.E. Balzer, W.G. Proud, S.M. Walley, J.E. Field, “High-speed photographic study of the drop-weight impact response of RDX/DOS mixtures”, *Combustion and Flame* 135 (2003) 547–555.

[29] R.C. Glenn, W.C. Leslie, “The Nature of "White Streaks" in Impacted Steel Armor Plate”, *Metallurgical Transactions* 2 (1971) 2945–2947.

[30] M.A. Meyers, H.R. Pak, “Observation of an adiabatic shear band in titanium by high-voltage transmission electron microscopy”, *Acta Metallurgica* 34 (1986) 2493-2499.

[31] M.N. Raftenberg, C.D. Krause, “Metallographic observations of armor steel specimens from plates perforated by shaped charge jets”, *International Journal of Impact Engineering* 23, (1999) 757–770.

[32] J. Barry, G. Byrne, “TEM study on the surface white layer in two turned hardened steels”, *Materials Science and Engineering* A 325 (2002), pp. 356–364

[33] Y.B. Xu , W.L. Zhong , Y.J. Chen , L.T. Shen Q. Liu , Y.L. Bai , M.A. Meyers, “Shear localization and recrystallization in dynamic deformation of 8090 Al–Li alloy”, *Materials Science and Engineering* A299 (2001) 287–295.

[34] M. N. Bassim, “Study of the formation of adiabatic shear bands in steels”, *Journal of Materials Processing Technology* 119 (2001) 234-234.

[35] J.A. Hines, K.S. Vecchio, “Recrystallization kinetics within adiabatic shear bands”, *Acta Materialia* 45 (1997) 635–649.

[36] U. Andradea, M.A. Meyersa, K.S. Vecchioa, A.H. Chokshia, “Dynamic recrystallization in high-strain, high-strain-rate plastic deformation of copper”, *Acta Metallurgica et Materialia* 42 (1994) 3183-3195.

[37] A. Marchand, J. Duffy, “An experimental study of the formation process of adiabatic shear bands in a structural steel”, *Journal of the Mechanics and Physics of Solids* 36 (1988) 251–283.

[38] V.F. Nesterenko, M.A. Meyers, J.C. LaSalvia, M.P. Bondar, Y.J. Chen, Y.L. Lukyanov, “Shear localization and recrystallization in high-strain, high-strain-rate deformation of tantalum”, *Materials Science and Engineering* A229 (1997) 23-41.

[39] S. Nemat-Nasser, W. Guo, “Flow stress of commercially pure niobium over a broad range of temperatures and strain rates”, *Materials Science and Engineering* A284 (2000) 202–210.

[40] Q. Xue, V.F. Nesterenko, M.A. Meyers, “Evaluation of the collapsing thick-walled cylinder technique for shear-band spacing”, *International Journal of Impact Engineering* 28 (2003) 257–280.

[41] C. J. Shih, M. A. Meyers, V. F. Nesterenko, “High strain rate deformation of granular silicon carbide”, *Acta Materialia* 46 (1998) 4037-4065.

[42] H.C. Rogers, “Adiabatic plastic deformation”, *Annual Review of Material Science*, 1979, vol. 9, pp. 283–311.

[43] Q. Li, Y.B. Xu, Z.H. Lai, L.T. Shen, Y.L. Bai, “Dynamic recrystallization induced by plastic deformation at high strain rate in a Monel alloy”, *Materials Science and Engineering* A276 (2000) 250–256.

[44] G.A. Li, L. Zhen, C. Lin, R.S. Gao, X. Tan, C.Y. Xu, “Deformation localization and recrystallization in TC4 alloy under impact condition”, *Materials Science and Engineering* A 395 (2005) 98–101.

[45] D. Rittel, Z.G. Wang, A. Dorogoy, “Geometrical imperfection and adiabatic shear banding”, *International Journal of Impact Engineering* 35 (2008) 1280–1292.

[46] Y. Me-Bar, D. Shechtman, “On the adiabatic shear of Ti-6Al-4V ballistic targets”, *Material Science and Engineering* 58 (1983) 181–188.

[47] Q. Xue, M.A. Meyers, V.F. Nesterenko, “Self-organization of shear bands in titanium and Ti–6Al–4V alloy”, *Acta Materialia* 50 (2002) 575–596.

[48] M. A.Meyers, V. F. Nesterenko, J. C. LaSalvia, Qing Xue, “Shear localization in dynamic deformation of materials: microstructureal evolutiona and self-organization”, *Materials Science and Engineering* A317 (2011) 204-225.

[49] K.M. Roessig, J.J. Mason, "Adiabatic shear localization in the dynamic punch test, part I. experimental investigation", *International Journal of Plasticity* 15 (1999) 241-262.

[50] C.G. Lee, Y.J. Lee, S. Lee, "Observation of adiabatic shear bands formed by ballistic impact in Aluminum-Lithium alloys", *Scripta Metallurgica et Materialia* 32 (1995) 821.

[51] T.W. Wright, "Approximate analysis for the formation of adiabatic shear bands", *Journal of the Mechanics and Physics of Solids* 38 (1990) 515–530.

[52] A. Molinari, R.J. Clifton, "Analytical characterization of shear localization in thermoviscoplastic materials", *Journal of Applied Mechanics* 54 (1987) 806–812.

[53] M. C. Mataya, M. J. Carr, G. Kraus, "Flow Localization and Shear Band Formation in a Precipitation Strengthened Austenitic Stainless Steel", *Metallurgical Transactions* 13A (1982) 1263.

[54] M. A. Meyers, U. R. Andrade, A. H. Chokshi, "The Effect of Grain Size on the High-Strain, High-Strain-Rate Behavior of Copper", *Metallurgical Transactions* 26A (1995), 2881.

[55] J.R. Li, J.L. Yu, Z.G. Wei, "Influence of specimen geometry on adiabatic shear instability of tungsten heavy alloys", *International Journal of Impact Engineering* 28 (2003) 303–314.

[56] D.E. Graddy, M.E. Kipp, "The growth of unstable thermoplastic shear with application to steady-wave shock compression in solids", *Journal of the Mechanics and Physics of Solids* 35 (1987) 95-119.

[57] T.W. Wright, H. Ockendon, "A scaling law for the effect of inertia on the formation of adiabatic shear bands", *International Journal of Plasticity* 12 (1996) 927-934.

[58] B. Hwang, S. Lee, Y. C. Kim, N. J. Kim, D. H. Shin, "Microstructural development of adiabatic shear bands in ultra-fine-grained low-carbon steels fabricated by equal

channel angular pressing", *Materials Science and Engineering* A 441 (2006) 308–320.

[59] G. F. Vander Voort, *"ASM handbood"*, Volume 8 (2000) 469-495.

[60] J.F.C. Lins H.R.Z. Sandim, H.J. Kestenbach, D. Raabe, K.S. Vecchio, "A microstructural investigation of adiabatic shear bands in an interstitial free steel", *Materials Science and Engineering A* 457 (2007) 205–218.

[61] K. Cho, Y.C. Chi, J. Duffy, "Microscopic observations of adiabatic shear bands in three different steels", *Metallurgical Transactions A* 21 (1990) 1161–1175.

[62] X.W. Chen, Q.M. Li, S.C. Fan, "Initiation of adiabatic shear failure in a clamped circular plate struck by a blunt projectile", *International Journal of Impact Engineering* 31 (2005), pp. 877–893.

[63] M.A. Meyers, Y.B. Xu, Q. Xue, M.T. Perez-Prado, T.R. McNelley, *"Microstructural evolution in adiabatic shear localization in stainless steel"*, Acta Materialia 51 (2003) 1307–1325.

[64] J.A. Hines, K.S. Vecchio, S. Ahzi, "A model for microstructure evolution in adiabatic shear bands", *Metallurgical and Materials Transactions* 29A (1998) 191–203.

[65] M. T. Perez-prado, J. A. Hines, K. S. Vecchio, "Microstructural evolution in adiabatic shear bands in Ta AND Ta–W alloys", *Acta Materialia* 49 (2001) 2905–2917.

[66] Y.J. Chen, M.A. Meyers, V.F. Nesterenk, "Spontaneous and forced shear localization in high-strain-rate deformation of tantalum", *Materials Science and Engineering* A268 (1999) 70–82.

[67] J.L. Derep, "Microstructure transformation induced by adiabatic shearing in armour steel", *Acta Metallurgica* 35 (1987) 1245–49.

[68] D.R. Lesuer, C.K. Syn, O.D. Sherby, "Severe plastic deformation through adiabatic shear banding in Fe–C steels", *Materials Science and Engineering A* 410–411 (2005) 222–225.

[69] J. Talone, "Effect of strain-induced α'-martensite transformation on mechanical properties of metastable austenitic Stainless Steel", *Doctoral dissertation, Helsinki University of Technology, Department of Mechanical Engineering, Laboratory of Engineering Material*, 2007.

[70] W.S. Lee, C.Y. Liu, T. N Sun, "Dynamic impact response and microstructural evolution of inconel 690 superalloy at elevated temperatures", *International Journal of Impact Engineering* 32 (2005) 210–223.

[71] W. S. Lee, C. F. Lin, "Impact properties and microstructure evolution of 304L Stainless steel", *Materials Science and Engineering A* 308 (2001) 124–135.

[72] S.P. Timothy, I.M. Hutchings, "The structure of adiabatic shear bands in titanium alloy", *Acta Metallurgica* 33 (1985) 667.

[73] V. F. Nesterenkot, M. A. Meyers, H. C. Chen, "Shear Localization in High-Strain rate Deformation of granular Alumina", *Acta Materialia* 44 (1996) 2017-2026.

[74] W. Xue-bin, "Phenomenon of transformed adiabatic shear band surrounded by deformed adiabatic shear band of ductile metal", *The Transactions of Nonferrous Metals Society of China*, 18 (2008) 1177-1183.

[75] J. F. Kalthoff, A. Burgel, "Influence of loading rate on shear fracture toughness for failure mode transition", *International Journal of Impact Engineering* 30 (2004) 957–971.

[76] M.N. Bassim, A.G. Odeshi, "Shear strain localisation and fracture in high strength structural materials", *Archives of Materials Science and Engineering* 31 (2008) 69-74.

[77] Q. Xue, M.A. Meyers, V.F. Nesterenk, "Self-organization of shear bands in titanium and Ti–6Al–4V alloy", *Acta Materialia* 50 (2002) 575–596.

[78] A.G. Odeshi, S. Al-ameeri, S. Mirfakhraei, F. Yazdani, M.N. Bassim, "Deformation and failure mechanism in AISI 4340 steel under ballistic impact", *Theoretical and Applied Fracture Mechanics* 45 (2006) 18–24.

[79] K. Ryttberg, M. Knutson Wedel, P. Dahlman, L. Nyborg, "Microstructural evolution during fracture induced by high strain rate deformation of 100Cr6 steel", *Journal of Materials Processing Technology* 209 (2009) 3325–3334.

[80] D.M. Turley, E.D. Doyle, S. Ramaligam, "Calculation of shear strains in chip formation in titanium", *Materials Science and Engineering. A* 55 (1982) 45.

[81] J.C. Lemaire, W.A. Backofen, "Adiabatic instability in the orthogonal cutting of steel", *Metallurgical Transaction* 3 (1972) 477.

[82] G.R. Speich, *"ASM handbook"*, Vol. 1 (2005) 697-707.

[83] A.G. Odeshi, M.N. Bassim, S. Al-Ameeri, Q. Li, "Dynamic shear band propagation and failure in AISI 4340 steel", *Journal of Materials Processing Technology* 169 (2005) 150–155.

[84] Amos Gilat, *"ASM handbook"*, Volume 8 (2000) 1134-1162.

[85] C.C. Menzemera, T.S. Srivatsanb, R. Ortiza, Meslet Al-Hajrib, M. Petraroli, "Influence of temperature on impact fracture behavior of an alloy steel", *Materials and Design* 22 (2001) 659-667.

[86] A.S. Bonnet-Lebouvier, A. Molinari, P. Lipinski, "Analysis of the dynamic propagation of adiabatic shear bands", *International Journal of Solids and Structures* 39 (2002) 4249–4269.

[87] A. Gilat, C.S. Cheng, "Torsional split Hopkinson bar tests at strain rates above 10^4 s^{-1}", *Experimental Mechanics* 40 (2000) 54–59.

[88] K. Ryttberg, M. Knutson Wedel, L. Nyborg, "Electron microscopy of white-etching band generated by high-velocity parting off of 100CrMn6 steel", *Materials Science and Engineering A* 480 (2008) 489–495.

[89] W. D. Callister, Jr., *"Materials science and engineering an introduction"*, 7th edition, John Wiley and Sons, Inc., 2007.